EUROPEAN ORGANIZATION FOR NUCLEAR RESEARCH

CERN-PH-EP-2012-153
22 June 2012

arXiv:1207.6520v1 [hep-ex] 27 Jul 2012

Inclusive production of protons, anti-protons, neutrons, deuterons and tritons in p+C collisions at 158 GeV/c beam momentum

This paper is dedicated to the memory of Prof. Matey Mateev

B. Baatar[4], G. Barr[8], J. Bartke[3], L. Betev[6], O. Chvala[9,12], J. Dolejsi[9], V. Eckardt[7],
H. G. Fischer[6,a)], Z. Fodor[2], A. Karev[6], V. Kolesnikov[4], M. Kowalski[3], M. Makariev[11],
A. Malakhov[4], M. Mateev[10,13], G. Melkumov[4], A. Rybicki[3], N. Schmitz[7], P. Seyboth[7],
R. Stock[5], G. Tinti[8], D. Varga[1], G. Vesztergombi[2], S. Wenig[6]

(The NA49 Collaboration)

[1]Eötvös Loránd University, Budapest, Hungary
[2]KFKI Research Institute for Particle and Nuclear Physics, Budapest, Hungary
[3]H. Niewodniczański Institute of Nuclear Physics, Polish Academy of Sciences, Cracow, Poland
[4]Joint Institute for Nuclear Research, Dubna, Russia.
[5]Fachbereich Physik der Universität, Frankfurt, Germany.
[6]CERN, Geneva, Switzerland
[7]Max-Planck-Institut für Physik, Munich, Germany.
[8]Oxford University, Oxford, UK
[9]Charles University, Faculty of Mathematics and Physics, Institute of Particle and Nuclear Physics, Prague, Czech Republic
[10]Atomic Physics Department, Sofia University St. Kliment Ohridski, Sofia, Bulgaria
[11]Institute for Nuclear Research and Nuclear Energy, BAS, Sofia, Bulgaria
[12]now at University of Tennessee, Knoxville, TN, USA
[13]deceased

to be published in EPJC

---

a) e-mail: Hans.Gerhard.Fischer@cern.ch

Abstract

The production of protons, anti-protons, neutrons, deuterons and tritons in minimum bias p+C interactions is studied using a sample of 385 734 inelastic events obtained with the NA49 detector at the CERN SPS at 158 GeV/c beam momentum. The data cover a phase space area ranging from 0 to 1.9 GeV/c in transverse momentum and in Feynman x from -0.80 to 0.95 for protons, from -0.2 to 0.4 for anti-protons and from 0.2 to 0.95 for neutrons. Existing data in the far backward hemisphere are used to extend the coverage for protons and light nuclear fragments into the region of intranuclear cascading. The use of corresponding data sets obtained in hadron-proton collisions with the same detector allows for the detailed analysis and model-independent separation of the three principle components of hadronization in p+C interactions, namely projectile fragmentation, target fragmentation of participant nucleons and intranuclear cascading.

1 Introduction

Baryon and light ion production in proton-nucleus collisions has in the past drawn considerable interest, resulting in an impressive amount of data from a variety of experiments. This interest concentrated in forward direction on the evident transfer of baryon number towards the central region, known under the misleading label of ”stopping”, and in the far backward region on the fact that the laboratory momentum distributions of baryons and light fragments reach far beyond the limits expected from the nuclear binding energy alone. A general experimental study covering the complete phase space from the limit of projectile diffraction to the detailed study of nuclear effects in the target frame is, however, still missing. More recently, renewed interest has been created by the necessity of providing precision reference data for the control of systematic effects in neutrino physics.

In addition to and beyond the motivations mentioned above, the present study is part of a very general survey of elementary and nuclear interactions at the CERN SPS using the NA49 detector, aiming at a straight-forward connection between the different reactions in a purely experiment-based way. After a detailed inspection of pion [1], kaon [2] and baryon [3] production in p+p interactions, a similar in-depth approach is being carried out for p+C collisions. This has led to the recent publication of two papers concerning pion production [4, 5] and this aim is here being extended to baryons and light ions.

The use of the light, iso-scalar Carbon nucleus is to be regarded as a first step towards the study of proton collisions with heavy nuclei using data with controlled centrality available from NA49. It allows the control of the transition from elementary to nuclear interactions for a small number of intra-nuclear collisions, thus providing an important link between elementary and multiple hadronic reactions. It also allows for the clean-cut separation of the three basic components of hadronization in p+A collisions, namely projectile fragmentation, fragmentation of the target nucleons hit by the projectile, and intra-nuclear cascading. The detailed study of the superposition of these components in a model-independent way is the main aim of this paper. For this end the possibility of defining net proton densities by measuring anti-protons and thereby getting access to the yield of pair produced baryons, will be essential. As the acceptance of the NA49 detector does not cover the far backward region, the combination of the NA49 results with measurements from other experiments dedicated to this phase space area is mandatory. A survey of the s-dependence of backward hadron production in p+C collisions has therefore been carried out and is published in an accompanying paper [6]. This allows the extension of the NA49 data set to full phase space.

As the extraction of hadronic cross sections has been described in detail in the preceding publications [1–5], the present paper will concentrate on those aspects which are specific to baryon and light ion production, particularly in the exploitation of the NA49 acceptance into the backward hemisphere. After a short comment on existing double differential data in the SPS energy range in Sect. 2, a few experimental details will be given in Sect. 3 together with the binning scheme adopted for protons, anti-protons and neutrons. Section 4 will present a comprehensive description of particle identification in the backward hemisphere which is an important new ingredient of the optimized use of the NA49 detector in particular for the asymmetric p+A collisions. Section 5 deals with the extraction of the inclusive cross sections and with the applied corrections. Section 6 contains the data tables and plots of the invariant cross sections as well as some particle ratios and a comparison to the few available double differential yields at SPS energy for comparison. Section 7 describes the use of the extensive complementary data set from the Fermilab experiment [7] for the data extension into the far backward direction together with an interpolation scheme allowing for the first time the complete inspection of the production phase space for protons in the range -2 $< x_F <$ +0.95. This combined study is extended to deuterons and tritons in Sect. 8. Baryon ratios are shown in Sect. 9. p_T integrated quantities are given in Sect. 10 both for minimum bias trigger conditions and for the dependence on the number of measured grey protons. In addition, the measured p_T integrated neutron yields are presented in Sect. 10 together with a comparison to other integrated data in the SPS energy range. Section 11 contains a detailed discussion of the two-component mechanism of baryon and baryon pair production, thus covering the first two components of the hadronization process defined above. This Section contains experimental results from both p+p and p+C interactions including a comment on resonance decay and a comparison to a recent microscopic simulation code. Section 12 gives a detailed discussion of anti-proton production including the application of the two-component mechanism introduced in Sect. 11 and a study of the p_T dependence. The discussion of p_T integrated proton and net proton yields is presented in Sect. 13 followed by the exploitation of double differential proton and net proton cross sections in Sect. 14. The paper is closed by a summary of conclusions in Sect. 15.

2 The Experimental Situation

As already pointed out for pions in [4] there are only two sets of double differential inclusive data, for identified baryons and light fragments in p+C collisions in the SPS energy range. The differential inclusive cross sections are presented in this paper as:

$$\frac{d^2\sigma}{dx_F dp_T^2}, \tag{1}$$

with $x_F = 2p_L/\sqrt{s}$ defined in the nucleon-nucleon cms. A first data set [7, 8] covers the far backward direction for protons and light ions at five fixed laboratory angles between 70 and 160 degrees for total lab momenta between 0.4 and 1.4 GeV/c at a projectile momentum of 400 GeV/c. A second set [9] has been obtained in forward direction for 0.3 $< x_F <$ 0.88 and 0.15 $< p_T <$ 0.5 with 100 GeV/c beam momentum. The respective phase space coverage in x_F and p_T is shown in Fig. 1a,b for protons and anti-protons, respectively, with a superposition of the NA49 coverage for protons. This coverage is presented in more detail in Fig. 1c and for the anti-protons in Fig. 1d.

With the NA49 data covering lab angles of up to 40 degrees the combination with [7, 8] into a consistent data set becomes possible. This allows for the first time the complete scrutiny of the proton phase space in the range -2 $< x_F <$ +0.95, with only minor inter- and extrapolation.

3 Experimental information and binning scheme

As a detailed description of the NA49 detector and the extraction of inclusive cross sections has been given in [1–4, 10], only some basic informations are repeated here for convenience.

3.1 Target, grey proton detection, trigger cross section and event sample

The NA49 experiment is using a secondary proton beam of 158 GeV/c momentum at the CERN SPS. A graphite target of 1.5% interaction length is placed inside a grey proton detector which covers a range from 45 to 315 degrees in polar angle with a granularity of 256 readout pads placed on the inner surface of a cylindrical proportional counter. An interaction trigger is defined by a small scintillator 380 cm downstream of the target in anti-coincidence with the beam. This yields a trigger cross section of 210.1 mb corresponding to 91% of the measured

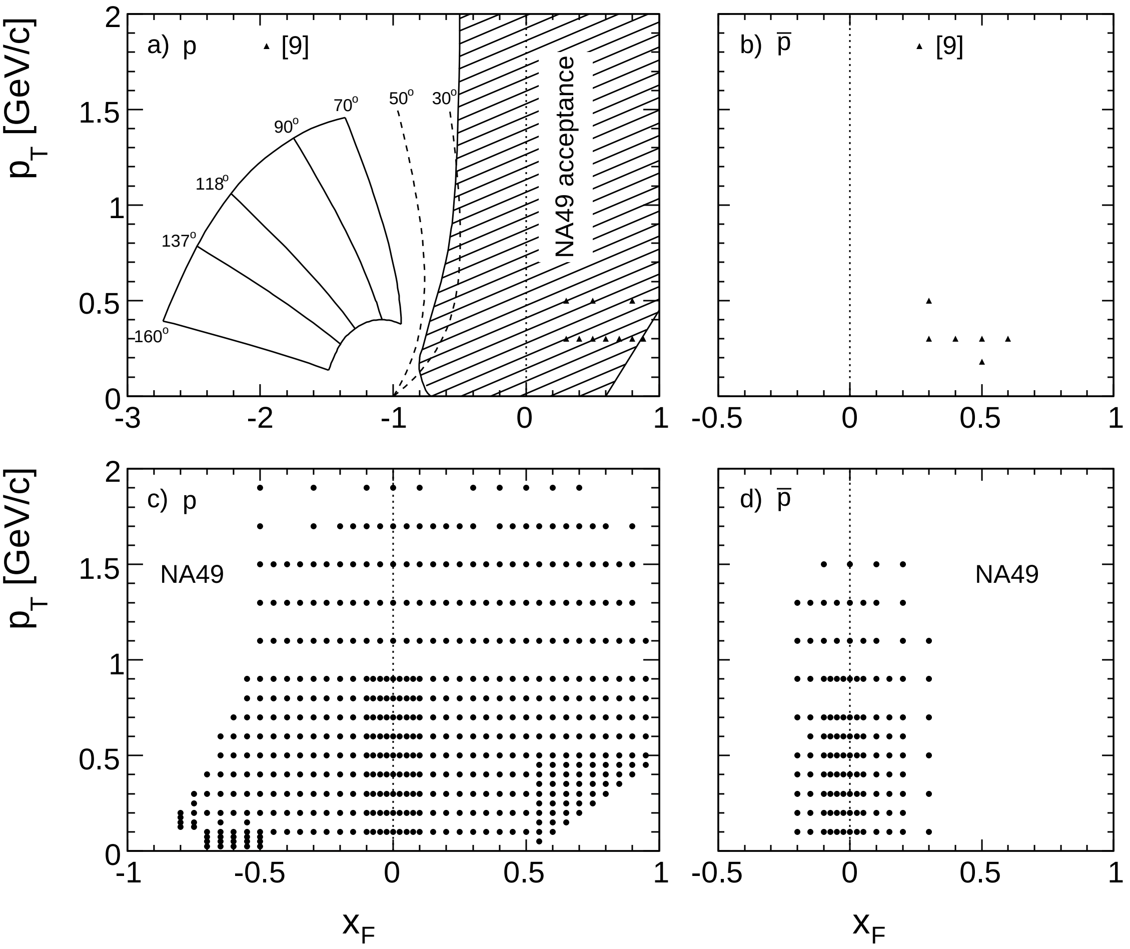

Figure 1: Phase space coverage of existing data: a) p data from [7] (full lines) and [9]. Here with the shaded area is shown the NA49 acceptance range; b) p̄ data from [9]; c) p data from NA49; and d) p̄ data from NA49

inelastic cross section of 226.3 mb. This is in good agreement with the average of 225.8 mb obtained from a number of previous measurements [4]. A total sample of 385.7k events has been obtained after fiducial cuts on the beam emittance and on the longitudinal vertex position.

3.2 Acceptance coverage, binning and statistical errors

The NA49 detector [10] covers a range of polar laboratory angles between ±45 degrees with a set of four Time Projection Chambers combining tracking and particle identification, two of the TPC's being placed inside superconducting magnets. While for anti-protons the accessible range in x_F and p_T is essentially defined by the limited event statistics, it has been possible to completely exploit the available range of polar angle for protons. The corresponding binning schemes are shown in Fig. 2 in the cms variables x_F and p_T.

A rough indication of the effective statistical errors is given by the shading of the bins. Neutrons have been detected in a forward hadronic calorimeter [3] in combination with proportional chambers vetoing charged hadrons. Due to the limited resolution in transverse momentum only p_T integrated information in 8 bins in x_F (Fig. 2c) could be obtained, after unfolding of the energy resolution. This coverage is identical to the one in p+p interactions [3] and allows for direct yield comparison.

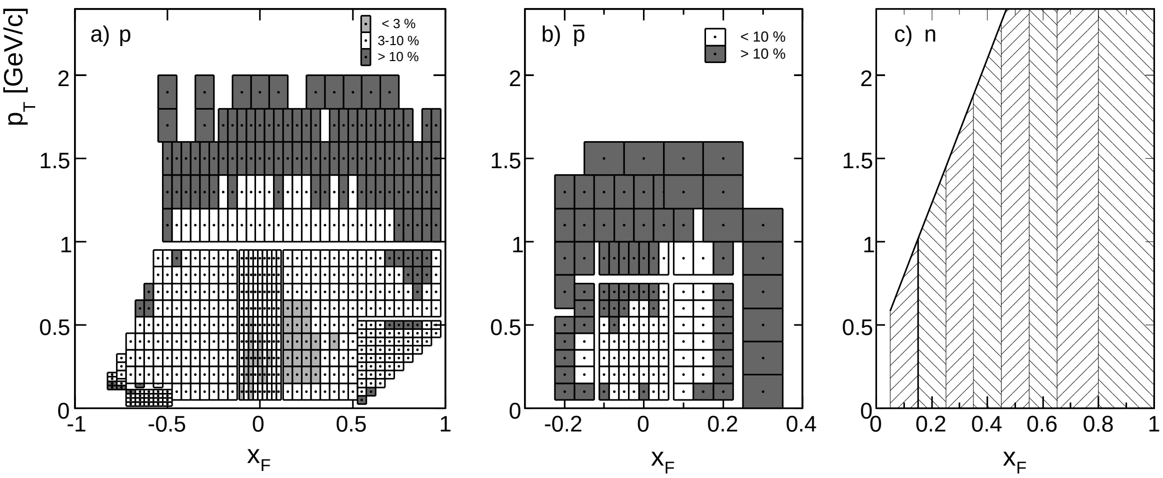

Figure 2: Binning scheme in x_F and p_T together with information on the statistical errors for a) protons, b) anti-protons and c) neutrons

4 Particle Identification

Due to the forward-backward asymmetry of p+A interactions, the study of the backward hemisphere is of major interest for the understanding of target fragmentation and intranuclear cascading. Particle identification at negative x_F is therefore mandatory; it has to rely for the NA49 detector on the measurement of ionization energy loss in the TPC system. This method has been developed and described in detail for mesons and baryons in p+p collisions in [1–3] for $x_F > 0$. A substantial effort has been invested for the present study in its extension to the far backward direction down to the acceptance limit in x_F imposed by the NA49 detector configuration. With decreasing x_F the baryonic lab momentum decreases below the region of minimum ionization where the ionization energy loss increases like $1/\beta^2$ and thereby successively crosses the deposits from kaons, pions and electrons. This is shown in Fig. 3 for the the momentum dependence of the parametrization of the mean truncated energy loss used in this analysis.

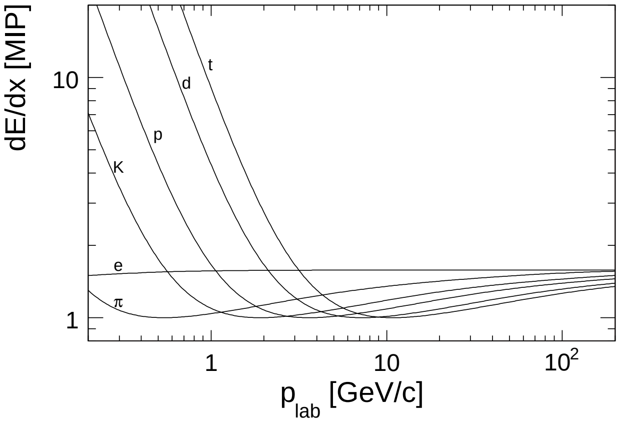

Figure 3: Parametrization of the mean truncated energy loss as a function of total lab momentum p_{lab} for electrons, pions, kaons and protons. The situation for deuterons and tritons is also indicated

In terms of x_F and p_T, this cross-over pattern reflects into lines of equal energy loss in the x_F–p_T plane as shown in Fig. 4.

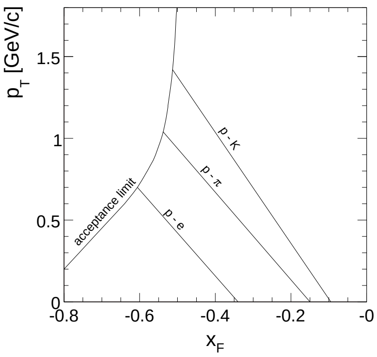

Figure 4: Lines of equal energy loss for protons and kaons (p-K), protons and pions (p-π) and protons and electrons (p-e) as functions of x_F and p_T, together with the acceptance limit of the NA49 detector

The region above the line p-K allows for the standard multi-parameter fits of the truncated energy loss distributions as described in the preceding publications [1–4]. The approximately triangular region below the line p-e permits the direct extraction of baryon yields partially even without fitting. This is exemplified in Fig. 5 for two bins at x_F = -0.5 and -0.6 and small p_T.

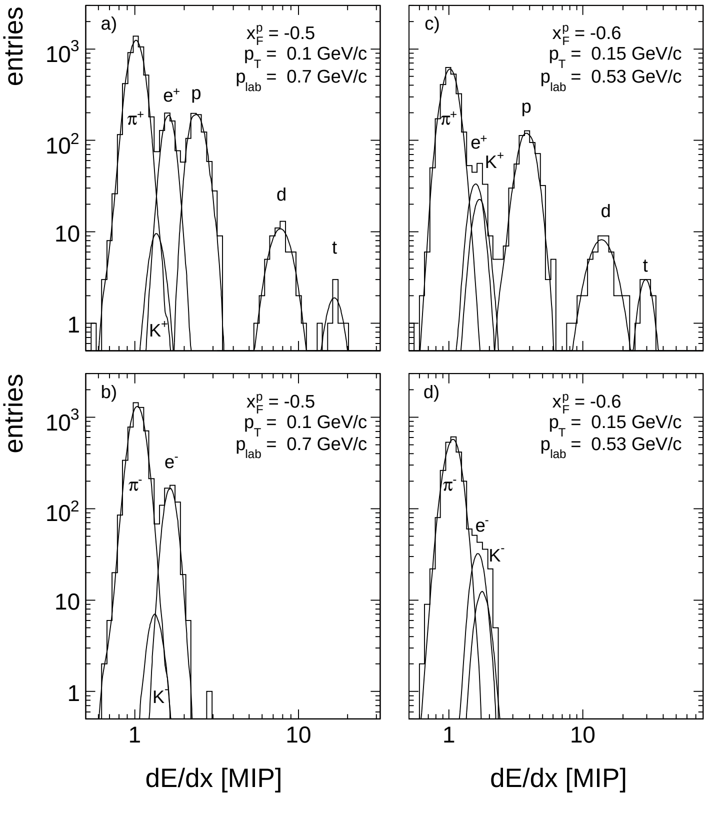

Figure 5: Truncated energy loss distributions for a) positives and b) negatives at x_F = -0.5, p_T = 0.1 GeV/c; and for c) positives and d) negatives at x_F = -0.6, p_T = 0.15 GeV/c

It is interesting to note that also the light ions deuteron and triton are here well separable practically without background. For anti-protons, a direct measurement of the p̅/p ratio becomes feasible down to values below 10^{-3} in this region.

In order to extract proton yields from the energy loss distributions in the intermediate region between the lines p-e and p-K, Fig 4, the particle ratios in each studied x_F/p_T bin are of prime importance. If the ratios p/π, k/π and e/π are known, proton yields may be obtained from the total number of tracks even in those bins where the proton energy loss equals the one from electrons, pions or kaons. A two-dimensional interpolation of the measured particle ratios over the full accessible phase space has therefore been established. These ratios are obtained without problem in the regions below the line p-e and above the line p-K (Fig. 4) as well as in most intermediate bins where a sufficient separation in dE/dx of the different particle species is present. Near the cross-over bins the measured ratios show a sharp increase of the effective statistical fluctuations, an increase which has been described in the discussion of the error matrix involved with the multi-dimensional fitting procedure in [2]. As this effect is of statistical and not of systematic origin, an interpolation through the critical regions in x_F and p_T is applicable.

It should be stressed here that the obtained particle ratios are non-physical in the sense that they use different phase space regions for each particle mass. For each x_F/p_T bin the necessary transformation to total lab momentum is performed using the proton mass for each track. This means that electrons, pions and kaons from different effective x_F values enter into the proton bin, with an asymmetry that increases with decreasing x_F and p_T. This is quantified in Fig. 6 where the effective mean x_F for electrons, pions and kaons is shown as a function of proton x_F^p for two values of p_T.

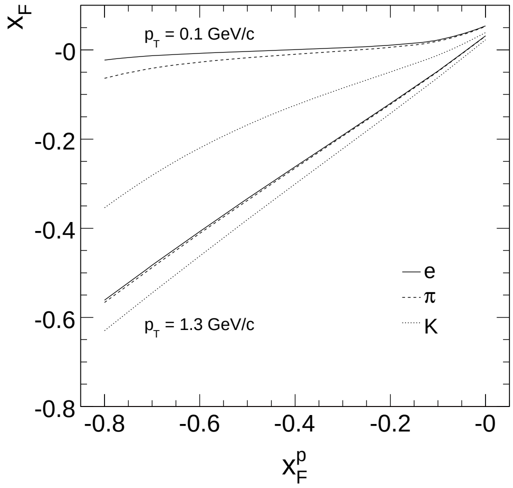

Figure 6: x_F for electrons, pions and kaons as a function of proton x_F^p for p_T = 0.1 GeV/c (upper lines) and p_T = 1.3 GeV/c (lower lines)

The lighter particles at small p_T are thus effectively collected from the neighbourhood of x_F = 0 with decreasing baryonic x_F. For anti-protons this purely kinematic effect is unfavourable for fitting as the effective p̅/π^- ratios quickly decrease below the percent level at low p_T, whereas the p/π^+ ratios stay always above about 10%, increasing rapidly with p_T due to the rather flat number distribution dn/dx_F. Proton and anti-proton extraction are therefore regarded separately in the following Sects. 4.1 and 4.2, respectively.

4.1 Proton extraction

4.1.1 e^+/π^+ ratio

The crossing of the proton dE/dx through the practically constant electron energy loss at $p_{\text{lab}} \sim 1$ GeV/c is the least critical effect as the momentum dependence of the proton dE/dx is a steep function of lab momentum in this p_{lab} range and as the e/π ratio quickly decreases with increasing p_T, reaching the 1% level already at $p_T > 0.3$ GeV/c. The e^+/π^+ ratio is shown in Fig. 7 as a function of x_F for four values of p_T together with the two-dimensional interpolation used.

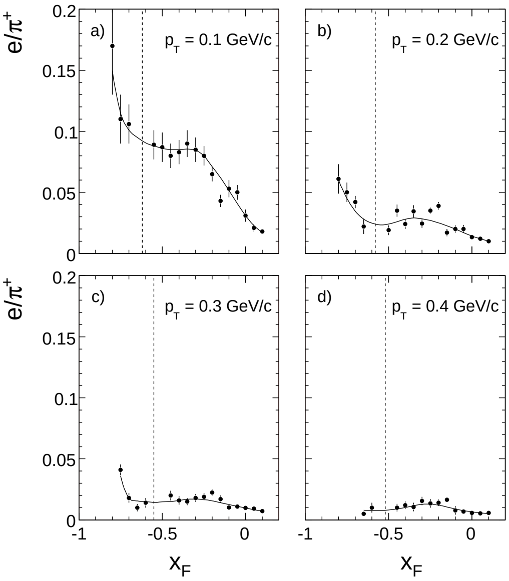

Figure 7: e^+/π^+ ratio as a function of x_F for a) p_T = 0.1 GeV/c, b) p_T = 0.2 GeV/c, c) p_T = 0.3 GeV/c and d) p_T = 0.4 GeV/c. The cross-over with the proton energy loss is indicated by vertical dotted lines. The full lines give the two-dimensional interpolation established from the data

Vertical lines indicate the position of the dE/dx cross-over for each p_T value and evidently the ratios may be well interpolated through the small affected x_F regions.

4.1.2 p/π^+ ratio

Fitted p/π^+ ratios are presented in Fig. 8 for four x_F values together with their two-dimensional interpolation as a function of p_T. If the fit results yield stable p_T dependences within their statistical errors in the uncritical regions at x_F = 0 and -0.6, the intermediate x_F values at -0.2 and -0.4 show some additional fluctuation in the cross-over regions indicated by the hatched areas which combine the p-π and p-K ambiguities.

Evidently the data interpolation describes the ratio properly through the ambiguous p_T areas.

A complete picture over the full available backward phase space is given in Fig. 9 where the fitted p/π^+ ratios are shown as functions of x_F for different p_T values together with the interpolations (full lines). The ratios at successive p_T values are shifted by a factor of 2 for clarity of presentation.

The complete situation for the data interpolation is finally presented in Fig. 10 with fixed vertical scale as a function of x_F at different p_T values. Here the acceptance limit of the NA49

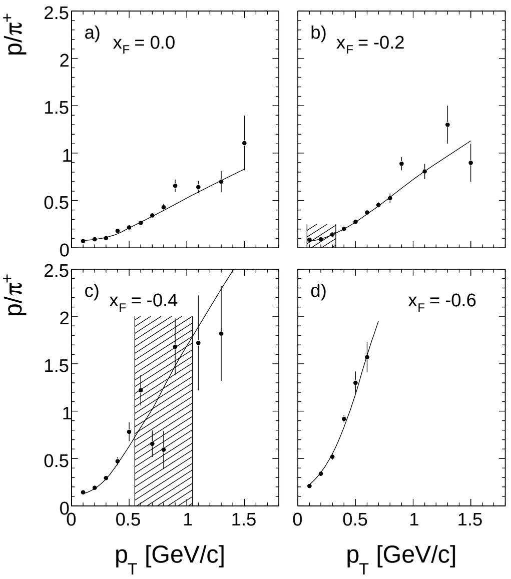

Figure 8: p/π^+ ratios as a function of p_T for a) x_F = 0, b) x_F = -0.2, c) x_F = -0.4 and d) x_F = -0.6. The full lines present the two-dimensional data interpolation, the hatched areas between the vertical lines the regions affected by the p-π and p-K ambiguities

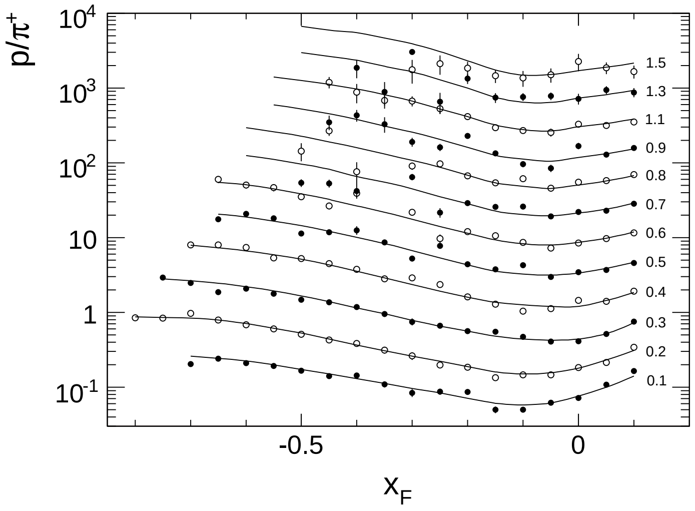

Figure 9: p/π^+ ratios as functions of x_F for fixed values of p_T [GeV/c]. Full lines: data interpolation. The ratios at successive p_T values are shifted by a factor of 2 for clarity of presentation

detector is given as the broken line together with the region of p-π and p-K ambiguity as hatched area.

This plot again clarifies the way in which the critical cross-over areas may be bridged by two-dimensional interpolation.

4.1.3 K$^+$/π^+ ratio

A situation quite similar to the p/π^+ ratio exists for the K$^+$/π^+ ratio. Again, there are regions of ambiguity against protons and pions, but the influence of eventual systematic deviations on the extraction of protons is small as the K$^+$/π^+ ratios are smaller than the p/π^+ ratio

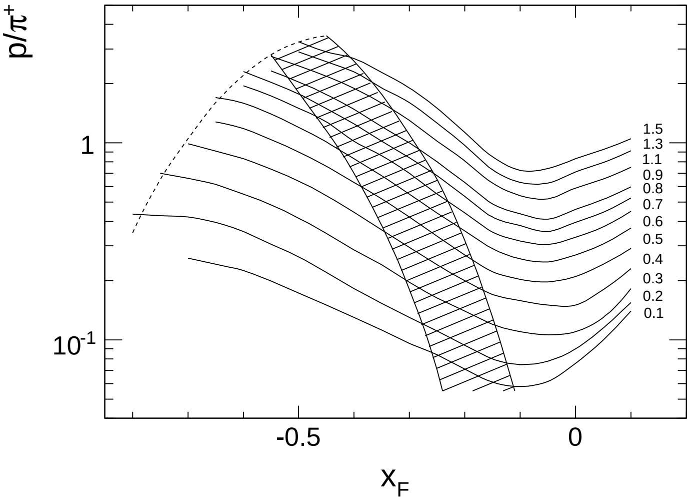

Figure 10: Interpolated p/π^+ ratios as functions of x_F for fixed values of p_T [GeV/c]. Broken line: NA49 acceptance limit. Hatched area: region of p-π and p-K ambiguity

by factors between 3 and 10. Fig. 11 shows K$^+$/π^+ ratios as functions of p_T for four x_F values, where the lowest and highest x_F at -0.6 and 0 allow for unambiguous fits over the full x_F range, whereas the x_F values at -0.2 and -0.4 suffer from p-K and K-π ambiguities in the hatched areas of p_T, with resulting increased statistical fluctuations. The two-dimensional interpolation is superimposed as full lines.

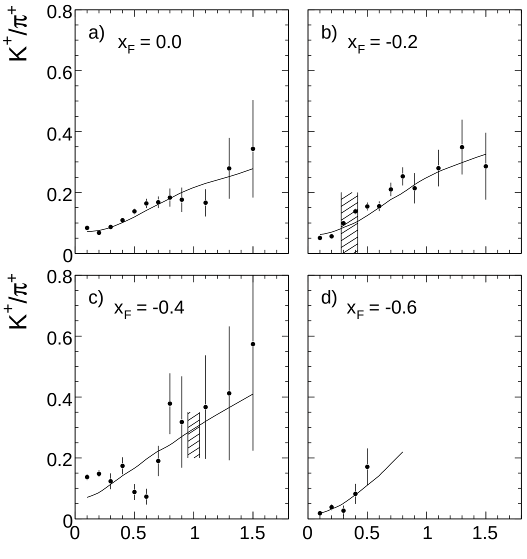

Figure 11: K$^+$/π^+ ratios as a function of p_T for four values of x_F, a) x_F = 0, b) x_F = -0.2, c) x_F = -0.4 and d) x_F = -0.6. The regions of p-K and K-π ambiguities are indicated as hatched areas in panels b) and c). The full lines represent the two-dimensional interpolation

All fitted values of K$^+$/π^+ are plotted in Fig. 12 as a function of x_F for fixed p_T. As in Fig. 9 the ratios at successive p_T values are shifted by 3 in order to sufficiently separate the measurements.

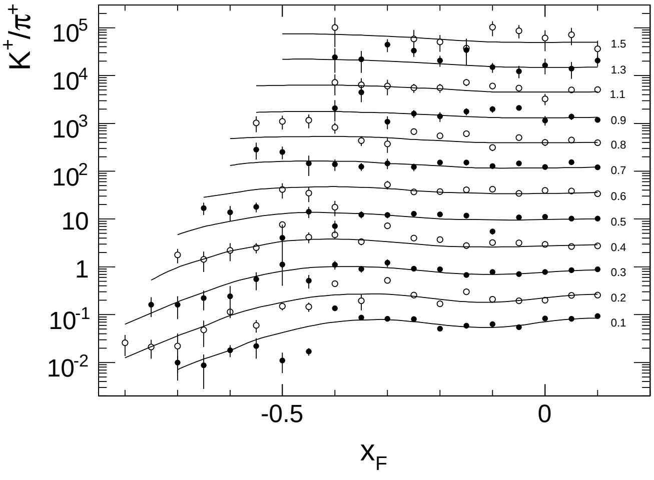

Figure 12: K$^+$/π^+ ratios as functions of x_F for fixed values of p_T [GeV/c]. Full lines: data interpolation. The ratios at successive p_T values are shifted by a factor of 3 for clarity of presentation

Fig. 13 presents the overview of the interpolated K$^+$/π^+ ratios at fixed vertical scale as a function of x_F for fixed values of p_T [GeV/c]. The broken line represents the acceptance limits and the hatched area the region of p-K and K-π ambiguity.

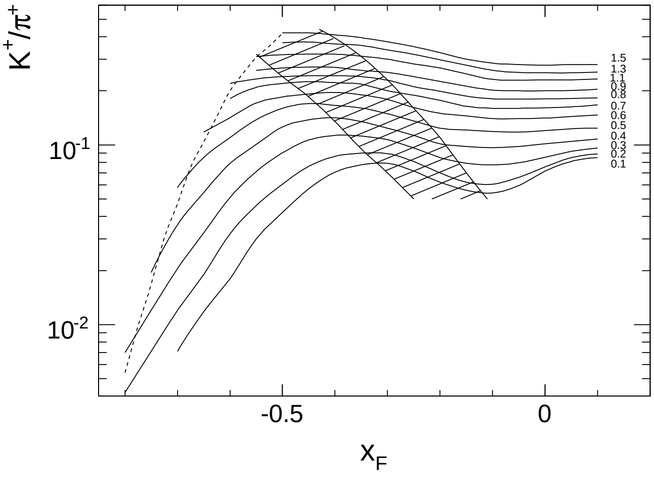

Figure 13: Interpolated K$^+$/π^+ ratios as functions of x_F for fixed values of p_T. Broken line: NA49 acceptance limit. Hatched area: region of K-π and p-K ambiguity

4.1.4 *Proton extraction in the far forward region*

Due to the gap between the TPC detectors imposed by the operation with heavy ion beams [10], charged particles progressively leave the TPC acceptance region at low p_T for $x_F > 0.55$. Here, tracking is achieved by the combination of a small ”gap” TPC (GTPC) in conjunction with two forward proportional chambers (VPC). The performance of this detector combination is described in detail in [3]. In the absence of particle identification in this area one has to rely on external information concerning the combined fraction of K$^+$ and π^+ in the total charged particle yield. Several considerations help to establish reference values for the (K$^+$ + π^+)/p ratios:

- The (K$^+$ + π^+)/p ratios decrease very rapidly with increasing x_F at all p_T, from about 10% at x_F = 0.6 to less than 1% at x_F = 0.9. Possible deviations from the used external reference data therefore introduce only small systematic effects in the extracted proton yield.
- Existing data may be used to come to a consistent estimation of the particle ratio. Direct measurements from Barton et al. [9] in p+C interactions cover the region from x_F = 0.2 to 0.8 for p_T = 0.3 and 0.5 GeV/c. Although the published invariant cross sections show sizeable deviations from the NA49 results, see Sect. 6.5, the particle ratios of the two experiments compare well.
- The ratios also comply with measurements in p+p collisions, both from NA49 [1–3] and from Brenner et al. [11] at 100 and 175 GeV/c beam momentum.

An overview of the experimental situation is given in Fig. 14 which shows the available measurements of the (K$^+$ + π^+)/p ratio as a function of x_F for eight values of p_T between 0.1 and 1.3 GeV/c. Here the full lines and full circles represent the NA49 measurements in p+p and p+C collisions, respectively, and the open circles and squares show the corresponding ratios from [9] and [11].

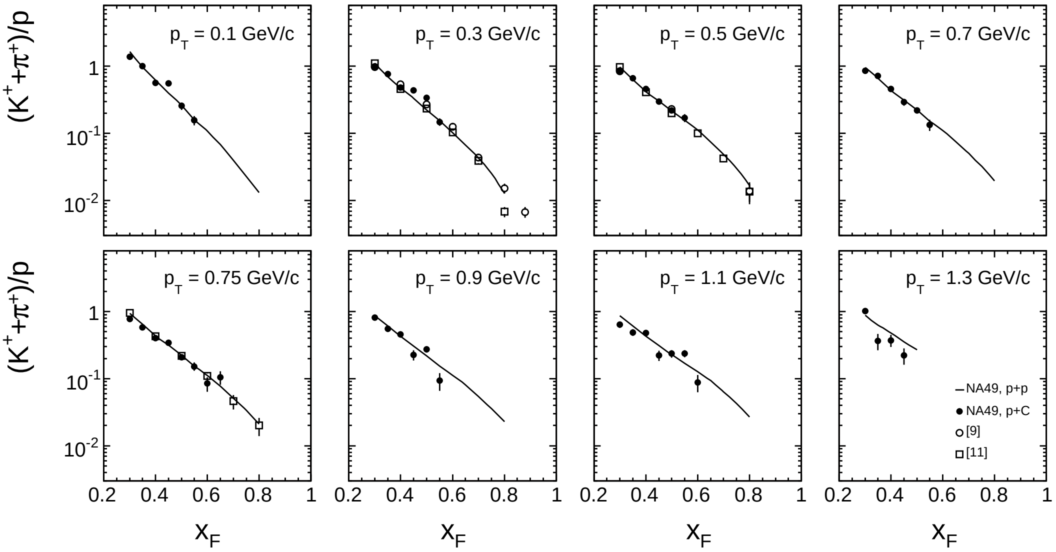

Figure 14: Measured (K$^+$ + π^+)/p ratios as a function of x_F for eight values of p_T between 0.1 and 1.3 GeV/c. The full lines give the results from NA49 in p+p collisions, the full and open circles the ones from NA49 and [9], respectively. Open squares: results from [11] in p+p interactions

An impressive consistency between the different experimental results within their statistical uncertainties is apparent. This allows for the safe extrapolation of the ratios into the non-measured region in p+C interactions. The slight deviations towards x_F = 0.3 are due to the fact that the reference ratios are obtained from invariant cross sections, whereas the values of interest for proton extraction are rather density ratios using the proton mass for the transformation to lab momentum, see Fig. 6 above. At $x_F > 0.3$ the two definitions converge rapidly. Also at $p_T > 1.1$ GeV/c systematic differences on the level of one standard deviation might be present. In this region however, the full TPC information is available at all x_F values, see Fig. 15 which shows the interpolated (K$^+$ + π^+)/p ratios as a function of p_T for different values of x_F.

The general data consistency on a $\sim$10% level apparent in Fig. 14 implies that possible systematic effects on the extracted proton cross sections in the region between the dotted and

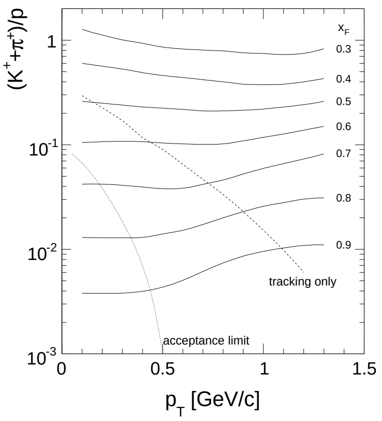

Figure 15: Interpolated (K$^+$ + π^+)/p ratios as a function of p_T for different values of x_F between 0.3 and 0.9, full lines. Broken line: border between available TPC information and the GTPC/VPC combination (Tracking only). Dotted line: acceptance limit of the NA49 detector

broken lines in Fig. 15 are on the percent level or below.

4.2 Anti-proton extraction

As stated above the extension of the determination of anti-proton yields into the backward hemisphere suffers from the fact that the $\overline{\text{p}}/\pi^-$ and $\overline{\text{p}}$/K$^-$ ratios come down rapidly with decreasing x_F. This is shown by the energy loss distributions of two typical bins in x_F and p_T in Fig. 16.

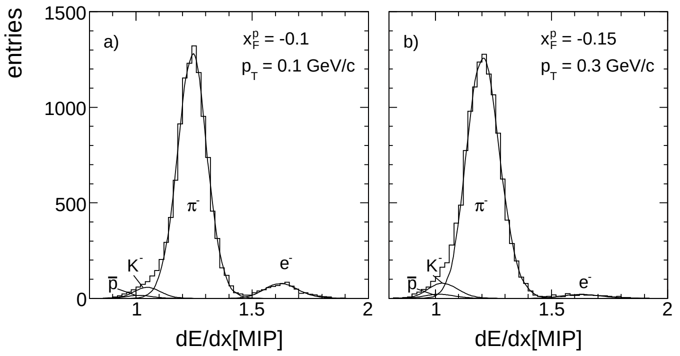

Figure 16: dE/dx distributions for negative particles a) x_F = -0.1, p_T = 0.1 and b) x_F = -0.15, p_T = 0.3

This effect is largely due to the asymmetry between the effective x_F for light particles and anti-protons due to the transformation to the lab momentum using proton mass, see Fig. 6. Thus at $x_F^{\overline{\text{p}}}$ = -0.2 pions are sampled close to maximum yield whereas the anti-proton cross section is steeply decreasing.

If the extraction of pion yields therefore presents no problem in this phase space region, the fits of kaon and anti-proton densities become strongly correlated with sizeable uncertainties in their relative position on the energy loss scale. The combined (K$^-$ + $\overline{\text{p}}$) yields however stay well defined with respect to the pions. This is shown by the fitted (K$^-$ + $\overline{\text{p}}$)/π^- ratios of Fig. 17.

In order to resolve the K$^-$-$\overline{\text{p}}$ ambiguity, the high statistics data on $\overline{\text{p}}$ production in p+p interactions [3] have been invoked. In this symmetric configuration, the measured $\overline{\text{p}}$ cross sec-

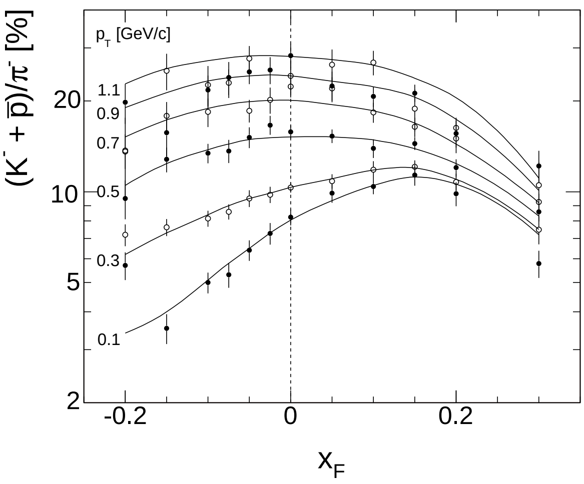

Figure 17: (K$^-$ + p̄)/π^- ratios as a function of x_F for fixed values of p_T. Full lines: two-dimensional interpolation of the fitted ratios

tions may be reflected into the backward hemisphere and thereby the correlation between the relative shifts $\delta_{\overline{\text{p}}}$ and δ_{K^-} in the dE/dx variable may be obtained imposing for each combination the given reflected cross section. As shown in Fig. 18 for x_F = -0.1 this correlation is precisely defined experimentally over the full p_T range, also yielding stable values of the p̄/π^- ratio.

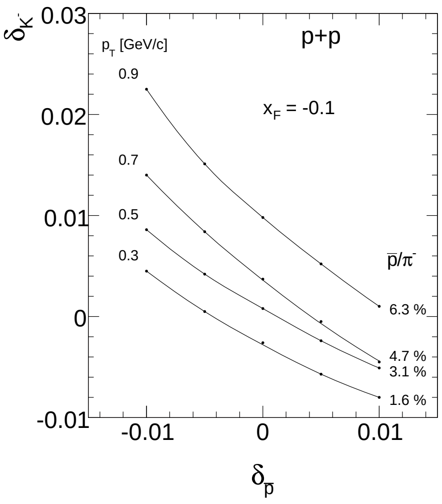

Figure 18: Correlation between the relative displacements $\delta_{\overline{\text{p}}}$ and δ_{K^-} in p+p collisions at x_F = -0.1 for fixed values of p_T, imposing the forward-backward symmetry of cross section in this interaction. The lines are given to guide the eye

Using the same correlation for the p+C data, effective p̄/π^- ratios are obtained. The observed stability of these ratios over the full range of the correlations is a strong test of the validity of the method.

Fig. 19 presents the obtained p̄/π^- ratios as a function of p_T for x_F = -0.05, -0.1 and -0.15, together with the directly fitted values at x_F = 0. Full lines: two-dimensional interpolation of the ratios.

A complete picture of the p̄/π^- ratios used in this analysis is given in Fig. 20 as a

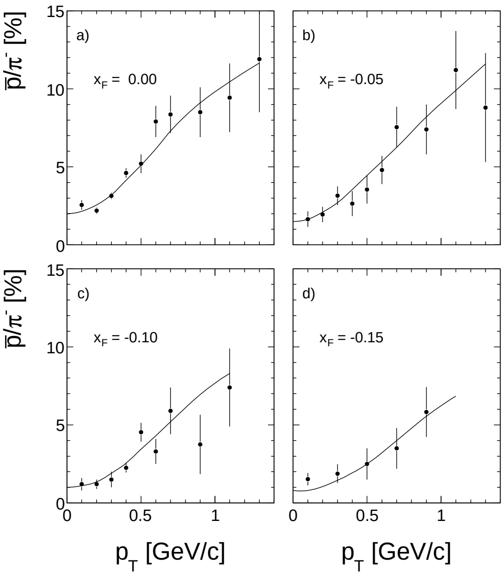

Figure 19: $\bar{p}/\pi^-$ ratios as a function of p_T for a) x_F = 0, b) x_F = -0.05, c) x_F = -0.1 and d) x_F = -0.2

function of x_F which combines the directly fitted ratios in the forward hemisphere with the ones obtained using the reflection method described above in the backward hemisphere.

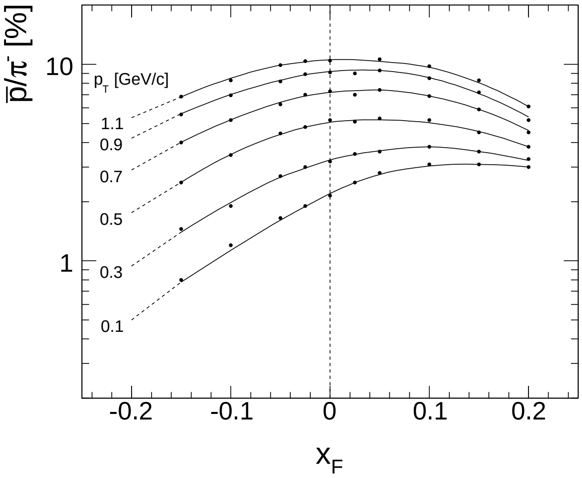

Figure 20: $\bar{p}/\pi^-$ ratios as a function of x_F for fixed values of p_T. The values at x_F = -0.2 are extrapolations using the broken lines

Note that the values at x_F = -0.2 are obtained by extrapolation following the broken lines. Note also that the applied method allows the extraction of the ratios in the percent and sub-percent region.

5 Evaluation of invariant cross sections and corrections

The invariant cross section,

$$f(x_F, p_T) = E(x_F, p_T) \cdot \frac{d^3\sigma}{dp^3}(x_F, p_T) \tag{2}$$

is experimentally determined by the measured quantity [1]

$$f_{\text{meas}}(x_F, p_T, \Delta p^3) = E(x_F, p_T, \Delta p^3) \cdot \frac{\sigma_{\text{trig}}}{N_{\text{ev}}} \cdot \frac{\Delta n(x_F, p_T, \Delta p^3)}{\Delta p^3} \quad , \tag{3}$$

where Δp^3 is the finite phase space element defined by the bin width.

As described in [1] several steps of normalization and correction are necessary in order to make $f_{\text{meas}}(x_F, p_T, \Delta p^3)$ approach $f(x_F, p_T)$. The determination of the trigger cross section and its deviation from the total inelastic p+C cross section have been discussed in [4]. The following corrections for baryons have been applied and will be discussed below:

- treatment of the empty target contribution
- effect of the interaction trigger
- feed-down from weak decays of strange particles
- re-interaction in the target volume
- absorption in the detector material
- effects of final bin width

5.1 Empty target contribution

This correction has been determined experimentally using the available empty target data sample, as described in [4]. The resulting correction is essentially determined by the different amounts of empty events in full and empty target condition. It is within errors p_T independent and equal for protons and anti-protons. It increases from about 2% in in the far forward direction to about 7% in the most backward region as shown in Fig. 21.

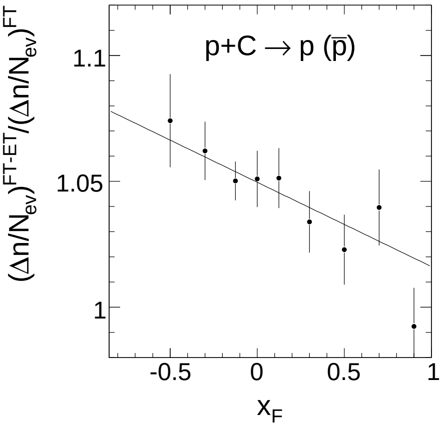

Figure 21: Empty target correction as a function of x_F. The full line shows the chosen interpolation

5.2 Effect of the interaction trigger

Due to the high trigger efficiency of 93% [4] this correction is small compared to p+p interactions [1]. It has been determined experimentally by increasing the diameter of the trigger counter using the accumulated data. Within its statistical uncertainty it is independent of p_T and similar for protons and anti-protons. Its x_F dependence as shown in Fig. 22 is following the expected trend [3] where the fast decrease in forward direction as compared to p+p collisions is due to the lower particle yields at high x_F.

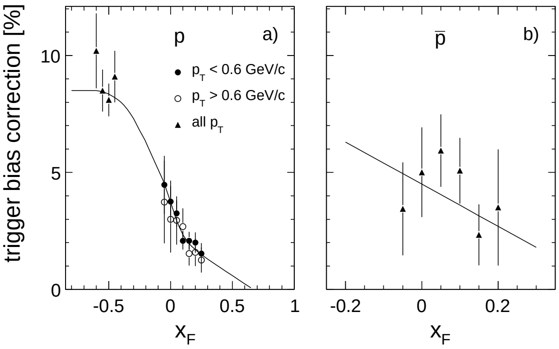

Figure 22: Trigger bias correction as a function of x_F for a) protons and b) anti-protons. The chosen interpolation is given by the full lines

5.3 Feed-down correction

The hyperon cross sections relative to p+p collisions established in [4] for $x_F > 0$ have been used. These cross section ratios approach at $x_F < 0$ the expected factor of 1.6 corresponding to the number of intranuclear projectile collisions, in account of the fact that for Λ and $\overline{\Lambda}$ there is no isospin effect [12]. For the contribution from target fragmentation this ratio should be constant into the backward hemisphere. For the determination of the feed-down correction the corresponding yields have to be folded with the on-vertex baryon reconstruction efficiency which reaches large values in the far backward hemisphere. The resulting correction in percent of the total proton yield drops however quickly below $x_F <$ -0.2 due to the decrease of the Λ cross section relative to protons and due to the fact that the important baryon contribution from intranuclear cascading has no hyperon content. The numerical values in percent of the baryon yields are shown in Fig. 23 as a function of x_F.

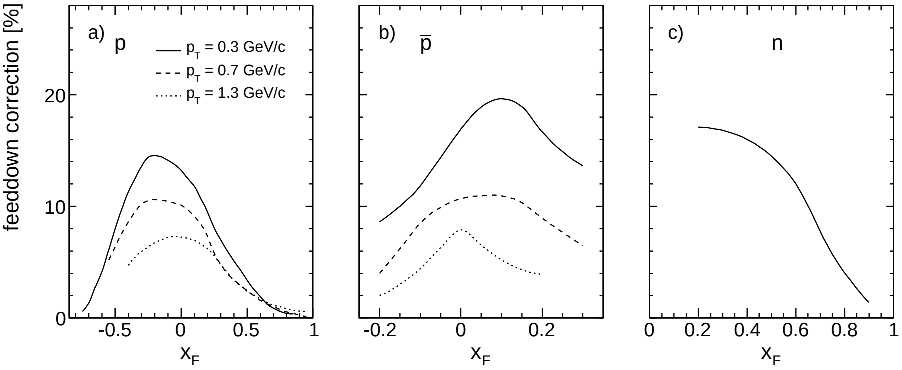

Figure 23: Feed-down correction as a function of x_F at different p_T values for a) protons, b) anti-protons and c) neutrons, in the latter case integrated over p_T

In comparison to the pion data [4] this correction reaches considerable values of up to 20% for the anti-protons and therefore constitutes, together with the absolute normalization, the most important source of systematic uncertainty.

5.4 Re-interaction in the target

The carbon target has an interaction length of 1.5%, which corresponds to about half of the length of the hydrogen target used in p+p collisions. The expected re-interaction correction is therefore smaller than +0.5% in the forward and -2% in the backward hemisphere. The values obtained in [3] have therefore been downscaled accordingly.

5.5 Absorption in the detector material

The absorption losses in the detector material are equal to the ones obtained in [3]. Baryons in the newly exploited region in the far backward direction feature short track lengths in the first NA49 TPC detector only and are not affected by any support structures; hence the corresponding corrections are below the 1% level as shown in Fig. 24.

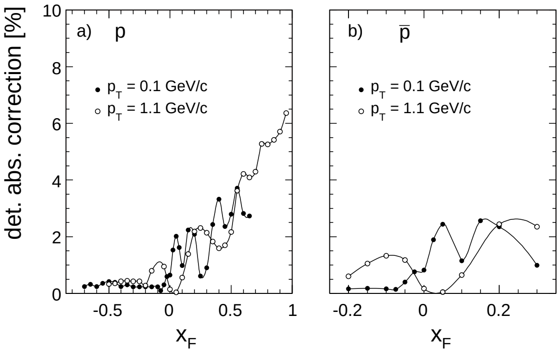

Figure 24: Detector absorption correction as a function of x_F at different p_T values for a) protons and b) anti-protons

5.6 Binning correction

The correction for finite bin width follows the scheme developed in [1] using the local second derivative of the particle density distribution. This correction stays, despite of the rather sizeable bins used in some areas of the p+C data, generally below the ±2% level, being negligible in the x_F co-ordinate for protons due to their rather flat dn/dx_F distribution. Two typical distributions of the p_T correction for protons and for the x_F correction for anti-protons are shown in Fig. 25 both for the nominal bin width of 0.1 GeV/c in p_T and 0.05 in x_F and for the actually used bin widths.

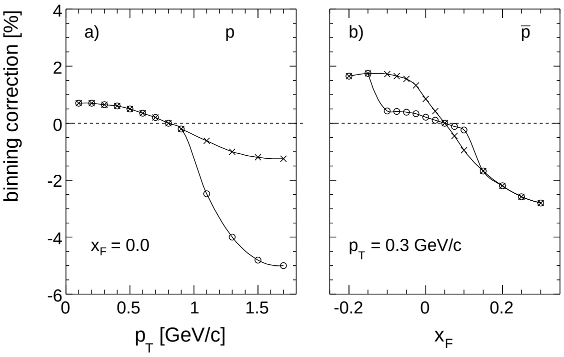

Figure 25: Binning correction a) in p_T for protons at x_F = 0 and b) in x_F for anti-protons at p_T = 0.3 GeV/c. The values for the nominal bin widths of 0.1 GeV/c in p_T and 0.05 in x_F are indicated by crosses, for the actually used bin widths by open circles

5.7 Systematic errors

An estimation of the systematic errors induced by the absolute normalization and the applied corrections is given in Table 1. For the proton and anti-proton extraction in the newly exploited backward regions an additional systematic error due to particle identification is indicated. An upper limit of 7.0% (8.5%) for protons (anti-protons) results from the linear addition of the error sources, increasing to 10% (14.5%) in the backward region. Quadratic summation results in the corresponding values of 3.7% (4.2%) and 4.7% (7.3%). The distribution of the numerical values of the corrections in all measured bins is shown in Fig. 26 for protons.

	p	$\bar{p}$		n
Normalization	2.5%	2.5%	Normalization	1.5%
Tracking efficiency	0.5%	0.5%		
Trigger bias	0.5%	2.0%	Trigger bias	1%
Feed-down	2.5%	2.5%	Feed-down	3%
Detector absorption	0.5%	0.5%	Detector absorption	0.5 – 1.5%
Target re-interaction			Target re-interaction	
Binning	0.5%	0.5%	Binning correction	
Particle ID backward	0 – 6%	2 – 10%	Acceptance	0 – 2%
			Energy scale error	4 – 8%
			Energy resolution unfolding	3 – 8%
backward			Charged veto efficiency	2 – 3%
Total(upper limit)	10.0%	14.5%	Cluster overlap	2%
Total(quadratic sum)	4.7%	7.3%	Hadron identification	2 – 5%
forward			K^0_L contribution	0 – 3%
Total(upper limit)	7.0%	8.5%	Total (upper limit)	28%
Total(quadratic sum)	3.7%	4.2%	Total (quadratic sum)	10%

Table 1: Systematic errors

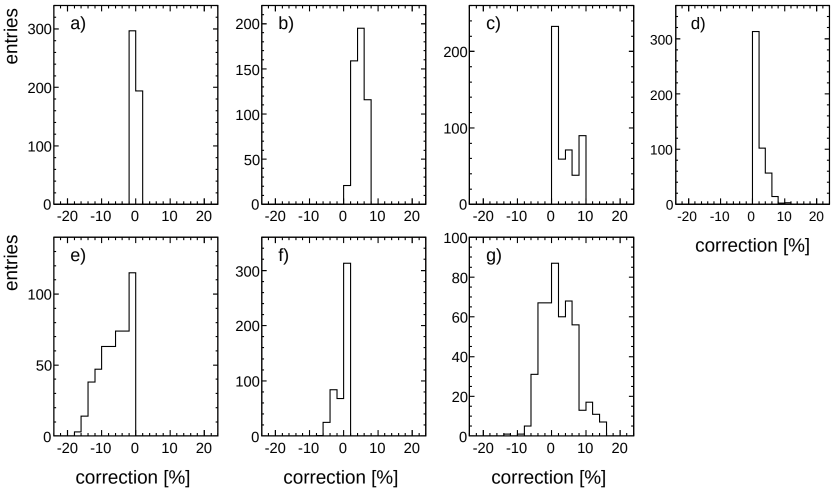

Figure 26: Distribution of proton corrections for a) target re-interaction, b) empty target, c) trigger bias, d) absorption, e) feed-down, f) binning, g) total

6 Results on double-differential cross sections for p and $\bar{p}$

6.1 Data tables

The binning scheme presented in Sect. 3 results in 491 and 121 data values for protons and anti-protons, respectively. These are presented in Tables 2 and 3.

	$f(x_F, p_T), \Delta f$									
$p_T \backslash x_F$	-0.8	-0.75	-0.7	-0.65	-0.6	-0.55	-0.5	-0.45	-0.4	-0.35
0.025			316.4 6.00	217.2 6.91	213.3 6.65	179.8 6.88	173.0 6.61			
0.05			308.1 8.17	262.3 4.46	254.7 5.50	176.0 4.87	166.8 6.09			
0.075			313.1 8.49	275.2 3.55	229.3 3.70	177.0 4.01	163.1 3.93			
0.1			368.4 13.0	279.3 6.70	224.9 5.12	207.2 4.37	165.3 5.32	118.6 3.70	102.0 3.76	78.7 4.24
0.125	465.1 11.1	320.8 16.9								
0.15	539.9 10.7	376.1 7.00		280.8 10.4		194.5 5.08				
0.175	437.5 9.88									
0.2	363.8 6.34	348.5 4.48	306.4 4.67	233.2 4.30	221.7 5.22	184.6 4.93	143.9 5.41	107.2 3.84	86.4 3.59	67.2 4.06
0.25		280.7 6.24								
0.3		217.2 6.52	222.0 6.87	152.7 4.94	150.0 6.18	123.1 4.60	94.4 5.45	88.3 4.45	69.5 3.55	58.8 3.95
0.4			141.3 7.45	128.0 7.51	110.2 7.74	86.1 5.27	72.7 5.46	64.6 4.40	51.0 4.81	45.3 3.74
0.5				65.2 9.40	72.6 8.54	61.5 5.58	53.9 5.37	44.9 5.81	36.7 5.03	32.6 4.23
0.6				38.5 11.2	37.9 10.8	36.8 6.59	32.8 7.74	29.4 6.58	28.4 5.20	20.8 5.13
0.7					21.2 13.3	23.2 7.78	23.0 7.37	19.0 7.57	17.6 7.48	15.47 5.98
0.8						14.0 9.43	11.65 7.96	13.6 8.18	11.10 8.85	9.60 6.00
0.9						9.25 8.80	8.16 8.29	8.64 10.2	6.57 8.91	6.49 8.37
1.1							2.17 13.2	3.14 8.93	2.25 9.51	2.39 8.94
1.3							0.68 21.9	1.21 13.0	1.19 12.5	1.07 12.4
1.5							0.339 20.6	0.504 18.7	0.425 19.0	0.443 19.7
1.7							0.145 19.2			
1.9							0.056 28.9			
$p_T \backslash x_F$	-0.3	-0.25	-0.2	-0.15	-0.1	-0.075	-0.05	-0.025	0.0	0.025
0.1	61.6 6.65	49.1 5.27	38.1 4.51	31.7 9.29	28.36 2.98	29.7 3.85	24.15 2.88	22.92 3.97	21.12 4.08	19.15 4.39
0.2	53.6 6.66	43.7 3.20	32.6 4.15	29.7 6.79	25.5 4.18	25.64 2.95	23.08 2.07	19.43 3.08	20.45 2.97	21.14 2.99
0.3	44.5 4.61	35.7 3.31	30.3 3.56	27.0 5.96	22.49 3.67	20.70 2.69	19.72 1.87	17.97 2.65	17.85 2.66	15.33 3.16
0.4	36.4 4.00	27.45 3.32	23.07 3.59	19.4 6.31	17.38 3.65	16.36 3.77	15.54 2.60	14.95 4.20	14.84 2.58	13.22 3.01
0.5	26.5 4.12	21.0 5.22	17.51 3.68	14.36 6.45	13.32 3.86	12.64 4.49	12.59 2.67	12.63 4.19	11.53 4.31	10.67 3.06
0.6	17.9 5.65	15.68 4.27	12.48 4.39	10.37 7.02	9.30 4.28	9.83 4.73	8.74 3.41	8.71 4.67	7.93 4.84	8.42 4.20
0.7	13.43 5.97	11.73 4.51	8.56 4.99	7.12 5.03	6.71 4.74	6.64 5.44	5.91 3.88	6.72 6.00	5.75 6.35	5.53 4.93
0.8	8.36 7.08	7.08 5.70	6.19 5.51	4.77 5.85	4.36 5.63	4.70 7.35	4.05 5.32	4.04 7.40	4.21 7.21	4.00 7.46
0.9	5.75 8.03	4.91 6.48	3.99 6.70	3.38 6.68	2.81 6.71	3.28 8.49	2.70 6.26	2.82 8.56	2.84 8.61	2.79 8.67
1.1	2.13 8.42	1.86 6.74	1.69 6.58	1.539 6.44	1.426 6.34		1.269 6.26		1.451 5.68	
1.3	0.84 12.6	0.859 11.0	0.703 9.78	0.608 10.0	0.568 9.42		0.566 9.14		0.543 8.88	
1.5	0.345 19.0	0.384 13.2	0.393 12.5	0.305 13.7	0.217 14.7		0.241 13.2		0.281 12.1	
1.7	0.166 20.4		0.134 20.7	0.151 18.2	0.100 21.2		0.116 19.1		0.086 21.4	
1.9	0.080 20.2				0.055 19.9				0.056 18.6	
$p_T \backslash x_F$	0.05	0.075	0.1	0.15	0.2	0.25	0.3	0.35	0.4	0.45
0.1	22.69 4.19	23.5 4.32	24.0 4.93	28.0 3.66	31.2 3.51	43.0 3.15	44.5 3.52	48.6 5.09	58.2 3.57	60.6 4.51
0.2	19.38 3.21	20.18 3.31	23.45 3.58	27.91 2.60	29.52 2.69	38.72 2.48	45.3 2.48	44.4 3.82	51.1 3.30	48.8 3.57
0.3	15.74 2.93	17.56 3.21	17.20 3.41	21.65 2.42	24.82 2.29	31.18 2.27	37.0 2.75	36.5 3.43	40.0 3.03	38.4 3.29
0.4	14.06 3.02	13.33 3.24	15.04 3.21	17.37 2.36	20.98 2.21	24.38 2.45	27.38 2.79	29.1 4.51	30.86 2.98	31.20 3.17
0.5	11.34 3.07	10.80 3.27	11.41 3.35	13.17 2.46	15.92 2.24	19.66 2.46	20.22 2.92	21.73 3.48	22.84 3.12	23.84 3.97
0.6	8.28 3.35	8.90 3.38	8.41 3.63	10.09 2.60	11.31 2.47	12.67 2.80	14.75 3.14	14.74 3.85	17.33 3.28	16.61 4.34
0.7	5.58 3.88	5.46 4.03	6.42 3.91	6.46 3.04	6.34 4.25	8.23 3.23	9.58 3.62	10.29 4.20	11.00 3.83	11.92 4.76
0.8	4.35 4.23	5.02 5.30	4.47 5.78	4.81 3.36	5.06 3.27	5.94 3.99	6.38 4.17	6.83 4.99	7.62 4.72	6.68 5.96
0.9	3.15 7.04	2.60 7.05	3.18 6.64	2.81 4.12	3.12 3.90	3.79 4.74	3.79 5.11	4.69 3.90	4.62 5.77	4.74 6.68
1.1	1.236 5.60		1.230 5.66	1.311 5.64	1.212 5.81	1.556 5.85	1.557 6.27	1.536 6.33	1.582 6.25	1.71 7.10
1.3	0.532 9.13		0.464 10.4	0.544 9.00	0.525 7.82	0.503 9.59	0.452 10.7	0.550 13.6	0.582 9.52	0.549 11.6
1.5	0.240 13.4		0.207 14.7	0.217 13.5	0.203 12.2	0.245 13.1	0.237 14.1	0.218 15.4	0.216 16.4	0.182 18.8
1.7	0.146 16.8		0.092 21.9	0.100 20.0	0.096 23.8	0.080 21.9	0.074 23.9		0.089 24.2	0.048 37.1
1.9			0.0284 28.6				0.0390 21.0		0.0307 27.7	
$p_T \backslash x_F$	0.5	0.55	0.6	0.65	0.7	0.75	0.8	0.85	0.9	0.95
0.05		80.3 12.5								
0.1	67.9 4.52	94.8 8.11	60.9 10.8							
0.15		65.6 7.88	78.9 7.81	71.7 8.64						
0.2	53.3 3.64	60.2 7.12	68.7 7.24	62.0 8.03	71.4 7.96					
0.25		51.8 6.92	79.5 6.01	55.8 7.60	63.6 7.47	70.3 7.50				
0.3	42.3 3.36	43.7 6.88	46.5 7.16	59.9 6.74	46.6 8.01	46.4 8.45	51.3 8.33			
0.35		34.6 7.16	39.5 7.20	48.4 6.93	43.5 7.67	43.4 8.06	49.0 7.91	41.8 8.91		
0.4	30.9 3.43	34.7 6.68	32.2 7.47	40.2 7.09	37.5 7.76	32.3 8.70	31.4 9.24	35.7 9.09	42.9 8.51	
0.45		27.3 7.12	24.6 8.06	28.5 7.96	25.8 8.80	31.3 8.42	29.1 9.09	29.2 9.41	39.6 8.39	47.1 7.76
0.5	22.20 3.64	22.2 7.50	23.0 7.91	25.7 7.98	19.8 10.1	17.9 10.5	20.2 10.3	22.3 10.2	31.1 8.80	45.0 7.54
0.6	15.46 3.98	15.48 4.36	17.28 4.43	16.41 4.85	16.6 6.77	16.0 7.20	13.0 8.28	14.9 8.01	15.7 7.98	25.0 4.82
0.7	11.10 4.36	11.38 4.70	10.21 5.34	11.28 5.40	10.16 7.98	9.64 8.57	8.58 9.41	7.19 10.6	9.02 9.71	14.10 5.95
0.8	8.07 4.77	6.82 5.68	6.66 6.17	5.62 7.14	6.37 9.41	7.11 9.33	5.92 10.5	5.52 11.3	3.72 12.6	7.18 7.83
0.9	4.04 6.34	4.50 6.58	4.08 7.39	4.05 7.91	3.12 12.6	3.64 12.2	3.01 14.0	3.07 14.3	2.89 15.2	3.94 10.0
1.1	1.53 6.54	1.73 6.70	1.64 7.41	1.26 8.91	1.19 9.67	1.27 13.1	1.13 14.4	1.11 15.1	1.01 16.4	1.04 12.5
1.3	0.590 9.45	0.510 11.1	0.657 10.6	0.368 14.9	0.465 14.0	0.531 18.6	0.372 22.9	0.273 27.7	0.53 20.9	0.451 17.4
1.5	0.191 14.8	0.145 18.6	0.107 23.6	0.125 23.6	0.132 24.3	0.202 27.7	0.136 35.4	0.072 50.0	0.216 30.1	0.186 25.0
1.7	0.068 21.3	0.056 26.7	0.045 33.4	0.023 50.0	0.034 44.7	0.054 50.0	0.045 57.7		0.052 57.7	0.051 44.7
1.9	0.0078 35.3		0.0117 40.9		0.0084 57.7					

Table 2: Invariant cross section, $f(x_F, p_T)$, in mb/(GeV^2/c^3) for protons in p+C collisions at 158 GeV/c beam momentum. The relative statistical errors, Δf, are given in %. The systematic errors are given in Table 1

$f(x_F, p_T), \Delta f$														
$p_T\backslash x_F$	-0.2		-0.15		-0.1		-0.075		-0.05		-0.025		0.0	
0.1	3.29	17.9	4.11	12.5	4.80	10.3	5.01	9.25	5.50	8.45	5.41	8.18	4.95	10.2
0.2	2.51	14.8	3.81	9.14	4.22	7.76	5.05	6.77	5.53	6.00	5.27	5.88	4.54	6.24
0.3	2.11	13.2	3.12	8.49	3.53	6.91	4.25	5.96	4.50	5.53	4.49	5.27	4.45	5.26
0.4	1.56	13.3	2.20	8.76	2.81	7.37	3.01	8.76	3.38	7.93	3.46	5.37	3.56	5.21
0.5	1.17	16.6	1.63	10.6	2.10	8.29	2.27	10.6	2.52	8.41	2.61	8.09	2.44	5.75
0.6			1.19	13.6	1.40	10.1	1.48	12.1	1.75	10.8	1.80	9.15	1.89	8.70
0.7	0.617	14.0	0.82	13.8	1.04	12.2	1.14	13.3	1.13	12.8	1.24	11.9	1.35	11.3
0.9	0.250	19.6	0.359	14.9	0.440	11.8	0.537	12.9	0.522	12.5	0.531	12.0	0.532	12.8
1.1	0.103	27.4	0.146	21.2	0.203	16.2			0.235	13.0			0.207	17.9
1.3	0.041	40.6	0.069	28.9	0.078	26.0			0.089	19.6			0.091	25.7
1.5													0.037	40.8

$p_T\backslash x_F$	0.025		0.05		0.1		0.15		0.2		0.3			
0.1	5.30	8.10	4.90	6.22	3.27	8.27	2.23	11.2	1.08	17.6	0.451	15.9		
0.2	4.88	6.06	4.66	4.55	3.05	6.16	1.86	8.84	1.28	11.8				
0.3	4.33	5.37	3.52	4.31	2.52	5.63	1.60	7.78	1.08	10.6	0.317	11.1		
0.4	3.00	5.67	3.03	4.15	2.26	5.27	1.44	7.31	0.817	10.6				
0.5	2.36	5.93	2.228	4.45	1.625	5.70	1.088	7.66	0.633	11.0	0.219	10.6		
0.6	1.44	10.1	1.56	7.10	1.227	6.15	0.913	7.87	0.566	10.9				
0.7	0.98	13.1	1.091	8.05	0.970	6.72	0.616	9.02	0.407	12.1	0.126	15.0		
0.9	0.460	15.0	0.466	9.09	0.422	9.05	0.246	9.08	0.177	14.4	0.069	18.2		
1.1			0.187	14.0	0.170	15.4	0.098	18.8	0.0563	16.1	0.0206	30.4		
1.3			0.073	25.8	0.067	24.0			0.0254	22.7				
1.5					0.0209	33.6			0.0121	31.5				

Table 3: Invariant cross section, $f(x_F, p_T)$, in mb/(GeV^2/c^3) for anti-protons in p+C collisions at 158 GeV/c beam momentum. The relative statistical errors, Δf, are given in %. The systematic errors are given in Table 1

6.2 Data interpolation

As in the preceding publications concerning p+p [1–3] and p+C [4] interactions, a two-dimensional interpolation is applied to the data which reduces the local fluctuations given by the errors of the data points by a factor of 3–4. As there is no possibility to describe the detailed x_F and p_T distributions by simple functions and as any algebraic approximation tends to dilute the data quality by introducing systematic biases, the chosen interpolation relies on a multi-step recursive method using eyeball fits. The quality of the procedure may be controlled by plotting the differences between data points and interpolation, normalized to the statistical errors. The resulting distribution should be a Gaussian centred at zero with variance unity. This is demonstrated in Fig. 27 for protons and anti-protons.

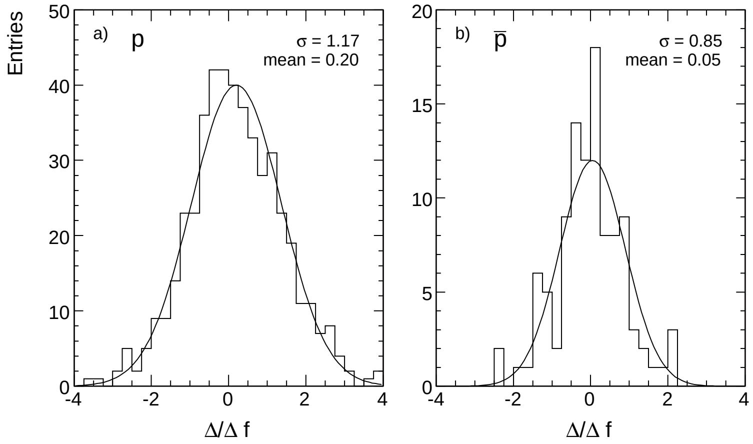

Figure 27: Plots of the normalized difference between data and interpolation for a) protons and b) anti-protons

6.3 Dependence of the invariant cross sections on $\mathbf{p_T}$ and $\mathbf{x_F}$

The distribution of the invariant cross section as a function of p_T is shown in Fig. 28 for protons and anti-protons at negative x_F and in Fig. 29 at positive x_F, indicating the data interpolation by full lines. For better visibility successive values in x_F have been multiplied by a factor 0.5.

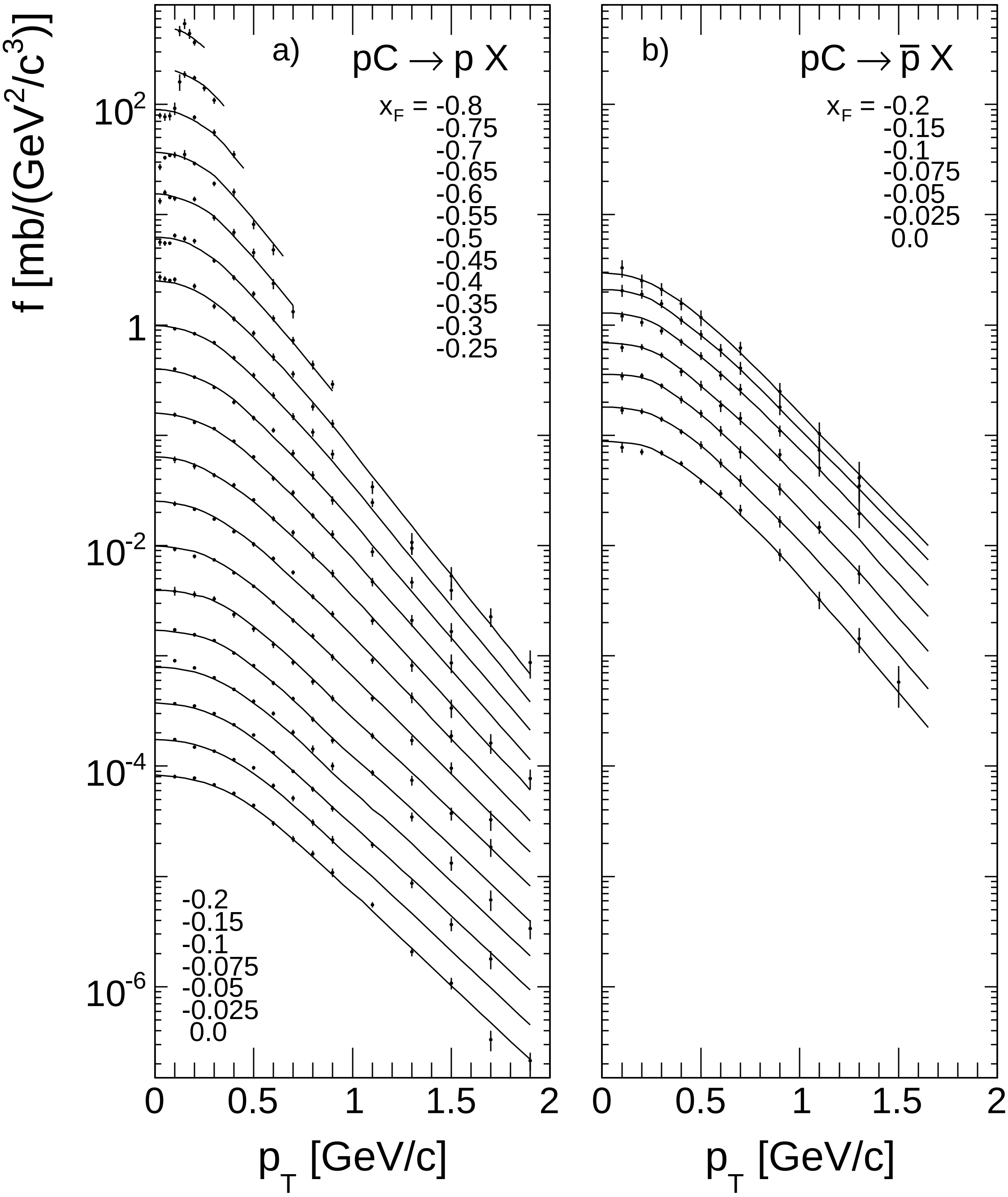

Figure 28: Invariant cross sections and data interpolation (full lines) as a function of p_T at fixed $x_F \leq 0$ for a) protons and b) anti-protons produced in p+C collisions at 158 GeV/c. The displayed cross sections have been multiplied by a factor of 0.5 for successive values of x_F for better visibility

Corresponding x_F distributions are presented in Fig. 30 for protons and in Fig. 31 for anti-protons.

The shape of the p_T distributions resembles, for $x_F \geq 0$ (Fig. 29), the one measured in p+p interactions [3] including details of the deviation from either exponential or Gaussian shape. In backward direction, Fig. 28, a more complex behaviour develops with a steepening

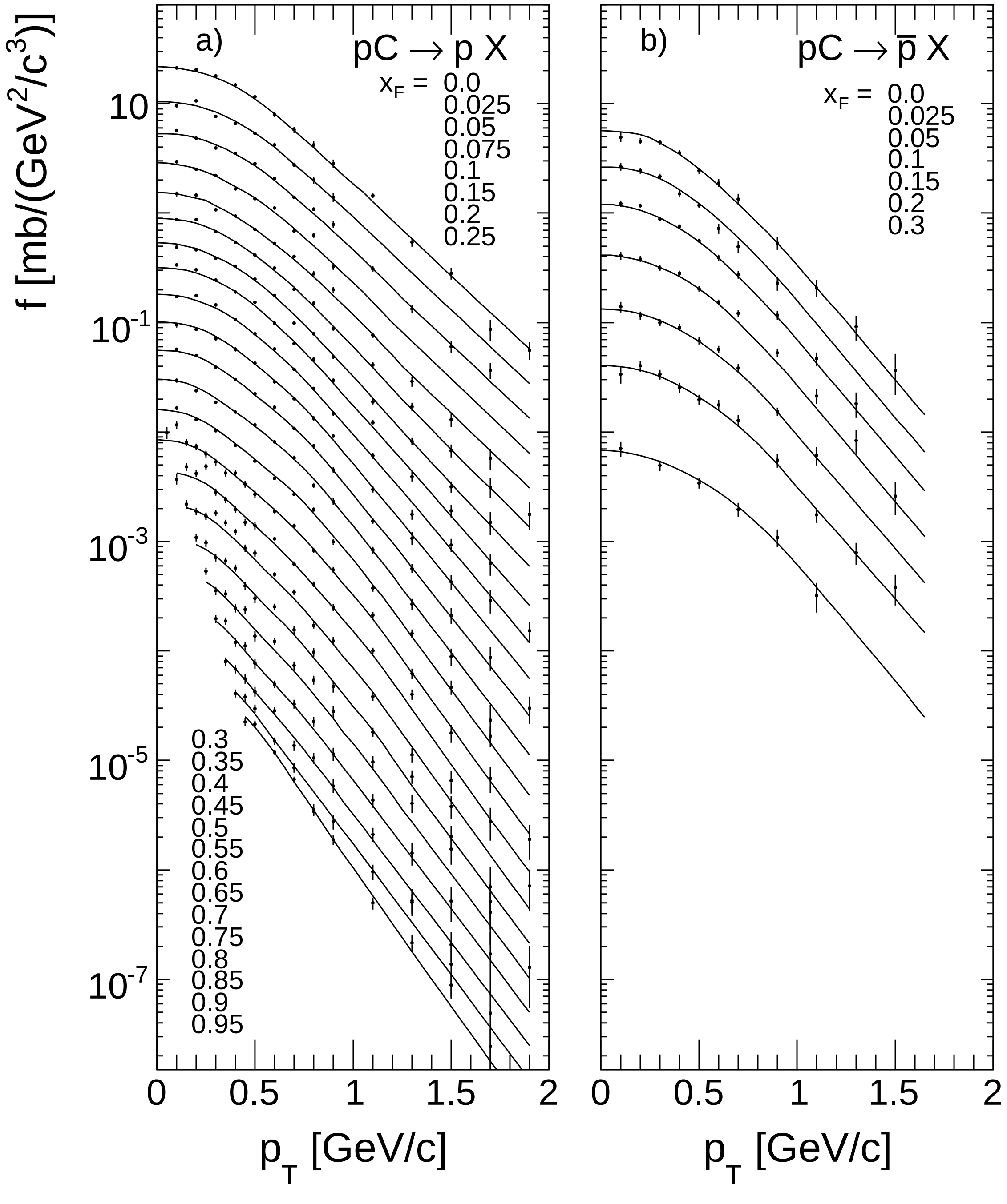

Figure 29: Invariant cross sections and data interpolation (full lines) as a function of p_T at fixed $x_F \geq 0$ for a) protons and b) anti-protons produced in p+C collisions at 158 GeV/c. The displayed cross sections have been multiplied by a factor of 0.5 for successive values of x_F for better visibility

up at $x_F < -0.4$. The basic asymmetry of the p+C interaction is more directly visible in the x_F distributions of Figs. 30 and 31. If at high p_T factors of 1.6–2 are typical between the backward and forward proton yields at x_F = 0.5–0.7, these factors grow to about 3–5 at p_T = 0.1 GeV/c. This allows a first view at the composition of p+A collisions from projectile fragmentation

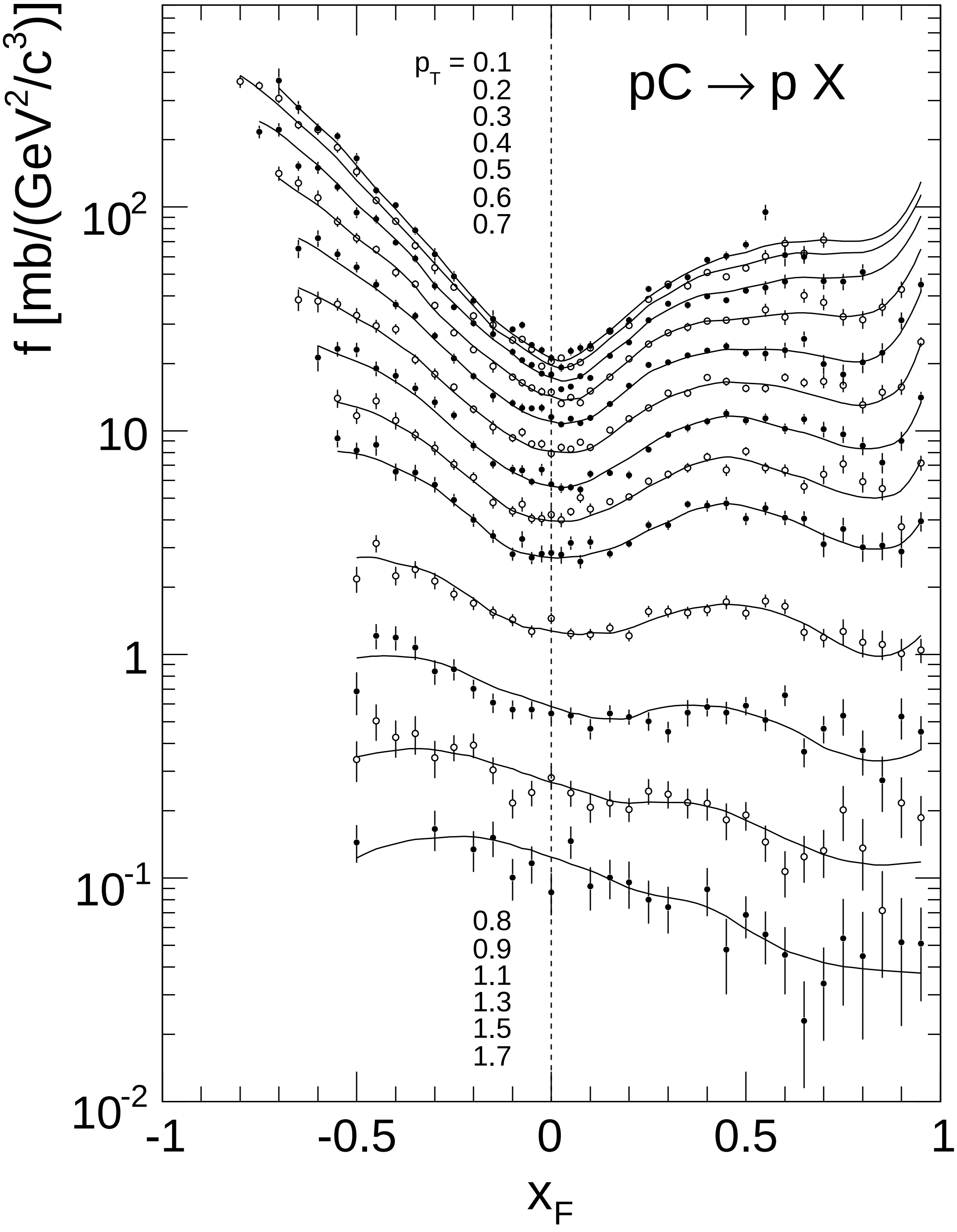

Figure 30: Invariant cross sections as a function of x_F at fixed p_T for protons produced in p+C collisions at 158 GeV/c. The p_T values are to be correlated to the respective distributions in decreasing order of cross section

in forward direction and target fragmentation as well as intranuclear cascading in backward direction. A quantification and separation of these three basic ingredients will be performed in Sects. 12, 13 and 14 below. For anti-protons the x_F distributions clearly peak at negative x_F. The forward-backward asymmetry is, at $|x_F|$ = 0.2, to first order p_T independent and on the order of 1.6–1.9 which is well above the asymmetry of protons at this x_F indicating important effects from isospin and baryon number transfer.

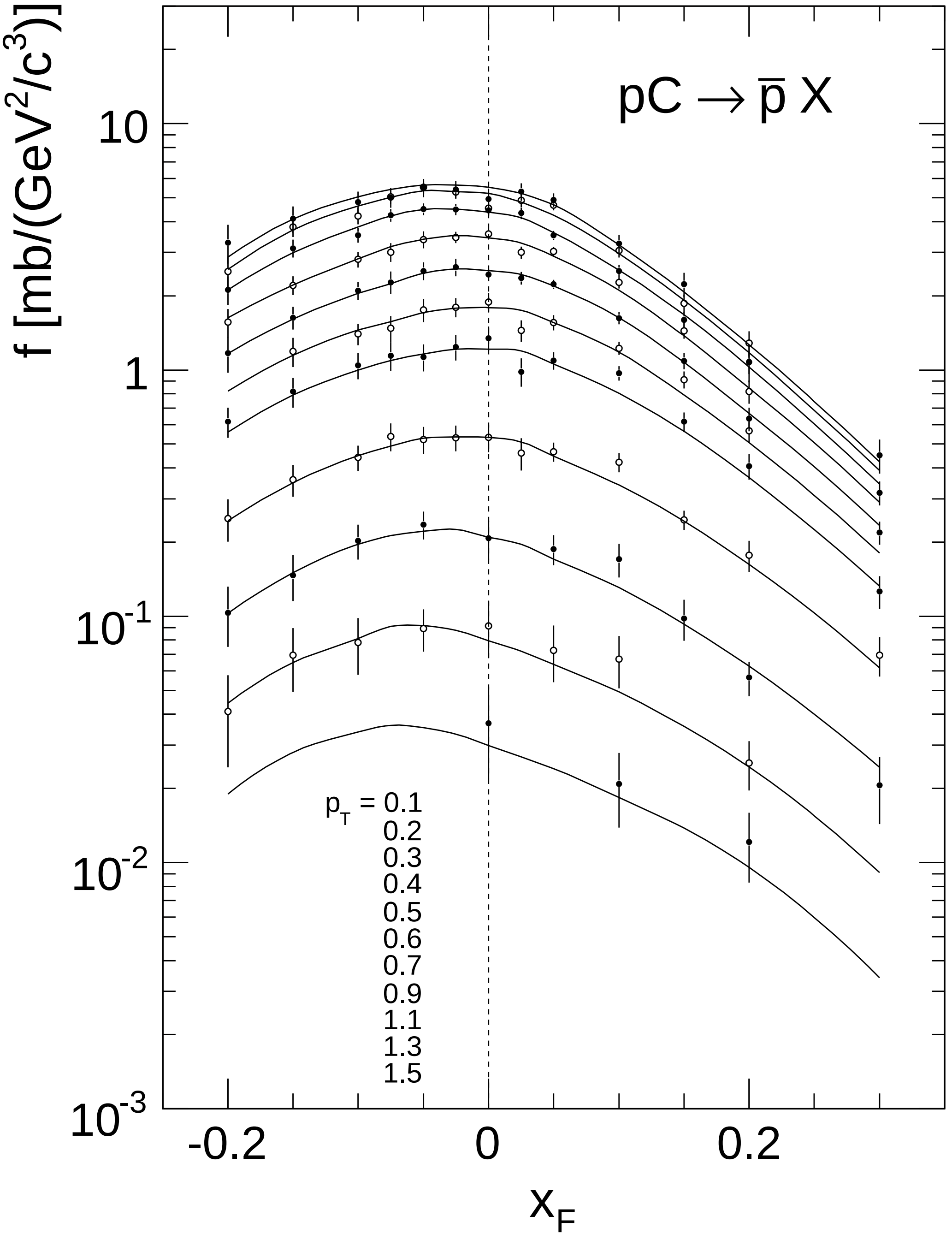

Figure 31: Invariant cross sections as a function of x_F at fixed p_T for anti-protons produced in p+C collisions at 158 GeV/c. The p_T values are to be correlated to the respective distributions in decreasing order of cross section

6.4 Rapidity and transverse mass distributions

The rapidity distribution for protons at fixed p_T presented in Fig. 32 extends to the kinematic limit in forward direction and to -2.6 units in the target hemisphere. Again a clear

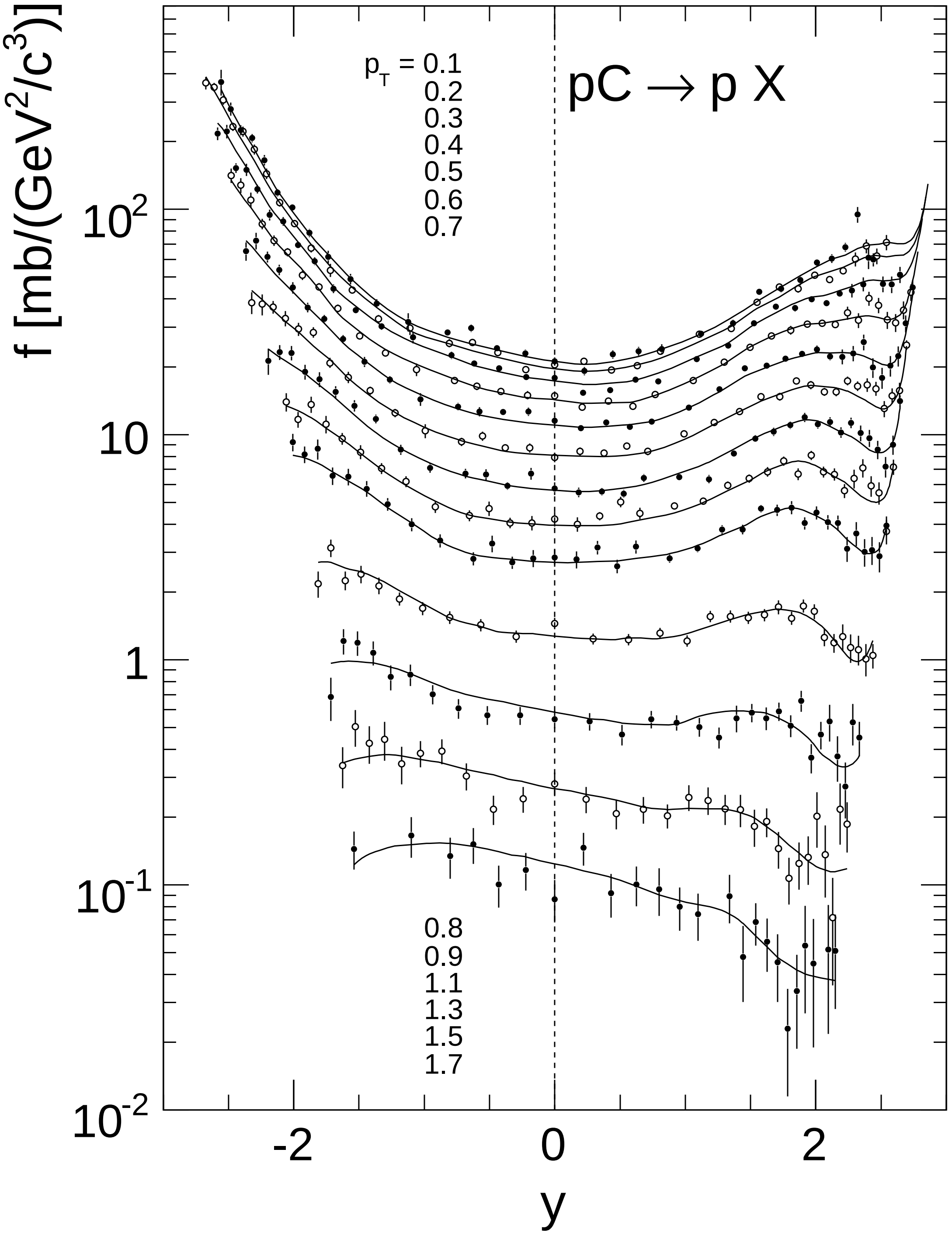

Figure 32: Invariant cross sections as a function of y at fixed p_T for protons produced in p+C collisions at 158 GeV/c. The p_T values are to be correlated to the respective distributions in decreasing order of cross section

view of the asymmetry of the p+C interactions increasing with decreasing p_T is evident.

The rapidity range of anti-protons is limited by statistics to -1.4 to +1.8 units. The corresponding distribution as a function of y for fixed p_T is shown in Fig. 33.

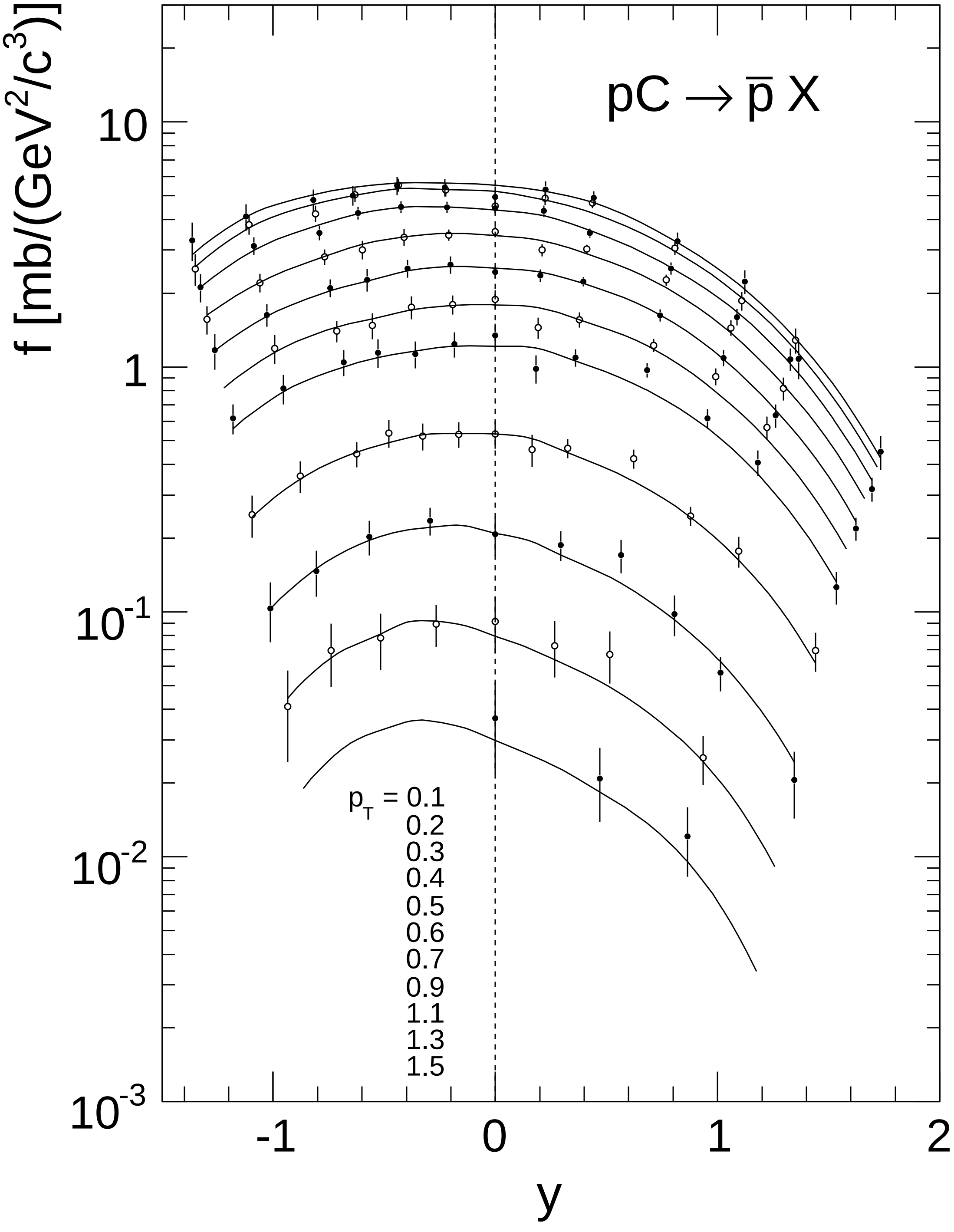

Figure 33: Invariant cross sections as a function of y at fixed p_T for anti-protons produced in p+C collisions at 158 GeV/c. The p_T values are to be correlated to the respective distributions in decreasing order of cross section

Transverse mass distributions at y = 0, with $m_T = \sqrt{m_p^2 + p_T^2}$, are presented in Fig. 34 together with the local inverse slopes. A situation very similar to p+p collisions emerges with a non-exponential behaviour and inverse slope parameters varying strongly with the transverse mass.

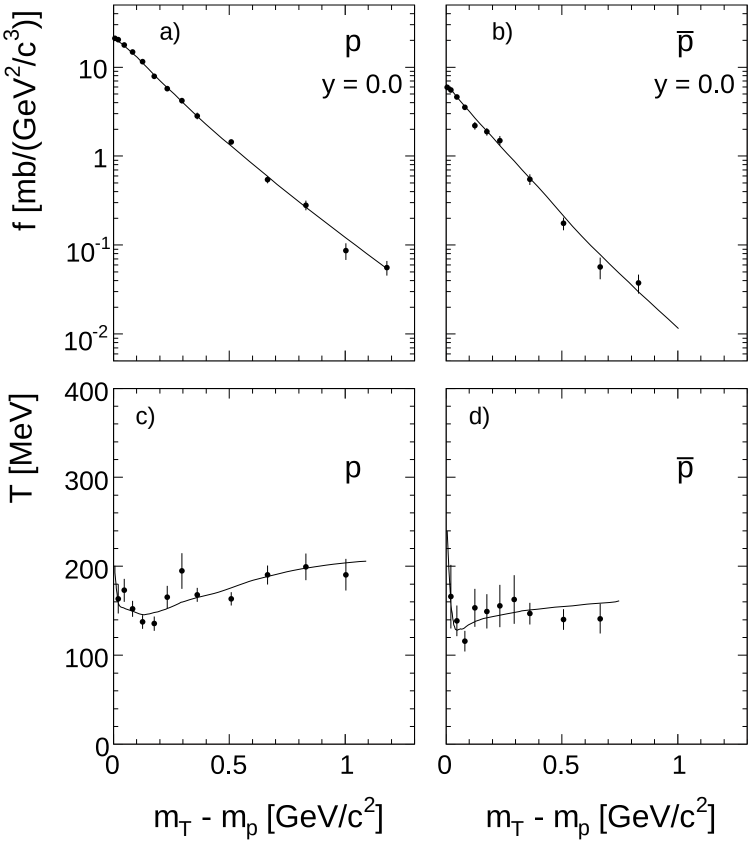

Figure 34: Invariant cross section as a function of $m_T - m_p$ for a) protons and b) anti-protons. Panels c) and d) give the inverse slope parameters of the m_T distributions as a function of $m_T - m_p$ for protons and anti-protons, respectively. The full lines represent the results of the data interpolation

6.5 Comparison to other experiments

As stated in Sect. 2 there are only two experiments providing double differential data in the SPS energy range. The data set [7] which is disjoint from the NA49 phase space coverage will be discussed in detail in the next Sect. 7. As far as the Fermilab data of Barton et al. [9] are concerned there are 10 data points for protons and 4 data points for anti-protons available in overlapping phase space ranges. The situation for protons is shown in Fig. 35 where the invariant cross sections [9] at p_T = 0.3 and 0.5 GeV/c are shown together with the data interpolation of the NA49 experiment as a function of x_F.

The comparison between the two experiments reveals very sizeable systematic offsets with an average of +21% or +6 standard deviations averaged over all data points. This complies with the comparison of pion yields [4] with an average of +25% or +3.6 standard deviations. The good agreement between the particle ratios (K^++π^+)/p demonstrated in Sect. 4.1.4 over the

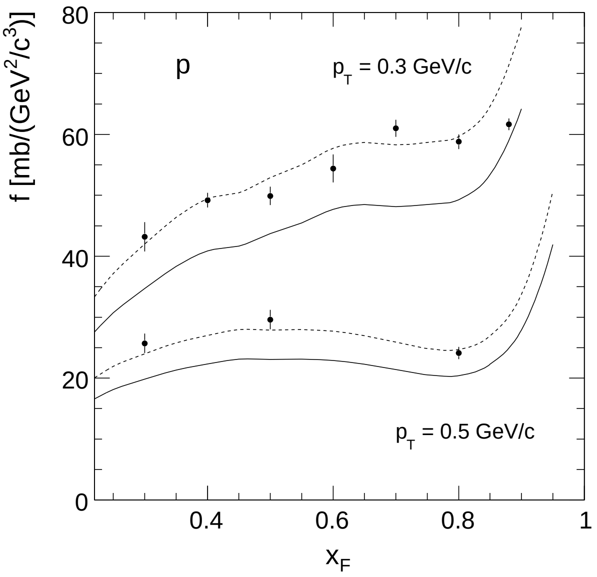

Figure 35: Invariant proton cross sections from [9] for p_T = 0.3 and 0.5 GeV/c together with the data interpolation of NA49 (full lines) and the interpolation multiplied by 1.21 (dashed lines)

full comparable range of x_F and p_T speaks indeed for a normalization problem as the origin of the discrepancies which are not visible in the results of p+p interactions [3].

For anti-protons the situation is considerably less clear due to the very large statistical errors of the data [9] indicating only upper limits for some of the measurements. Fig. 36 gives the x_F dependence of these data for p_T = 0.3 GeV/c together with the NA49 interpolation (full line) which has been partially extrapolated using an exponential shape. The large upward shift of the Fermilab data of about a factor of 2 (dashed line in Fig. 36) is compounded by the fact that due to the lower beam momentum of 100 GeV/c these data should be expected to be about

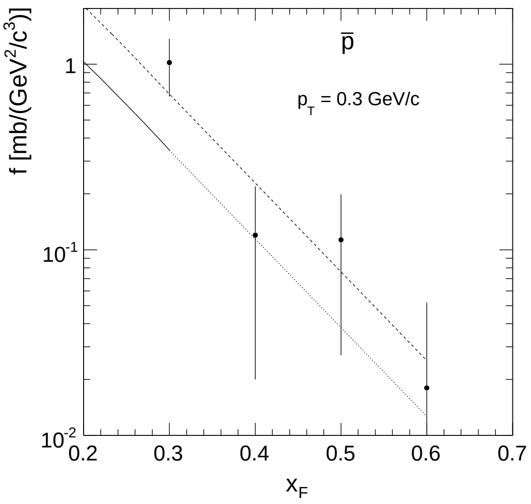

Figure 36: Invariant anti-proton cross sections from [9] for p_T = 0.3 GeV/c as a function of x_F together with the data interpolation of NA49 (full line) which has been extrapolated to x_F = 0.6 with an exponential function (dotted line). The NA49 reference multiplied by a factor of 2 is indicated by the dashed line

30–40% below the NA49 cross sections [3].

In this context it should be mentioned that already in p+p collisions the Fermilab data [11] were high by about +25% for anti-protons.

7 Data extension into the far backward direction

As the backward acceptance of the NA49 detector is limited to the ranges of $x_F >$ -0.8 to $x_F >$ -0.5 at low and high p_T, respectively, it is desirable to extend this coverage into the far backward region to x_F values down to and below -1. A detailed survey of existing experiments in the backward direction of p+C interactions has therefore been undertaken and is being published in an accompanying paper [6]. This survey establishes the detailed s-dependence of measured cross sections for beam momenta between 1 and 400 GeV/c, for lab angles between 10 and 180 degrees, and for lab momenta between 0.2 and 1.2 GeV/c. It shows in particular that the baryonic cross sections in the SPS energy range from about 100 to 400 GeV/c beam momentum may be regarded as s-independent within tight systematic limits of less than a couple of percent. This allows the combination of the extensive data set of the Fermilab experiment [7] at 400 GeV/c beam momentum and lab angles between 70 and 160 degrees with the NA49 data which span the angular range up to 40 degrees.

The relevant kinematic situation is presented in Fig. 37 where lines of constant p_{lab} and Θ_{lab} are shown in the x_F/p_T plane.

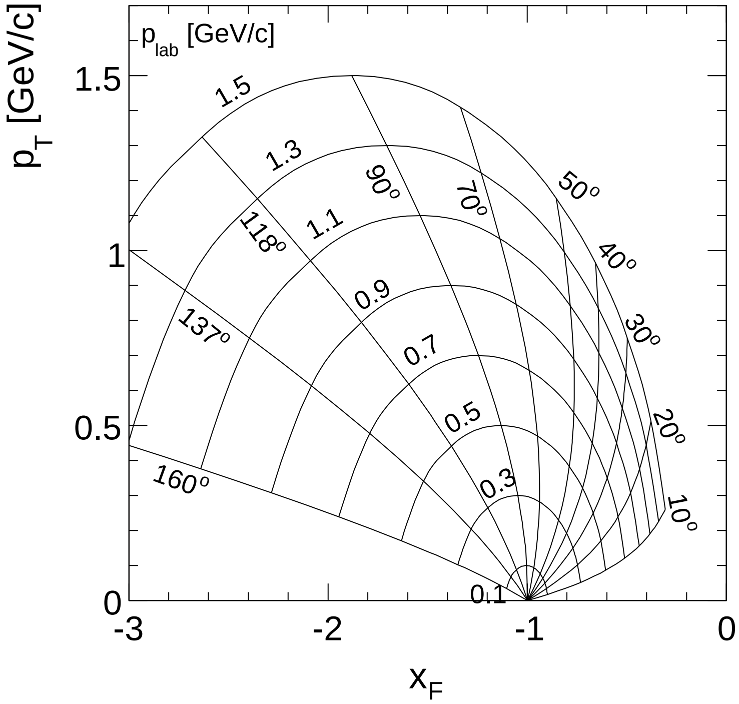

Figure 37: Kinematics of fixed p_{lab} and Θ_{lab} in the x_F/p_T plane

In the necessary transformation between the lab and cms frames involved in Fig. 37 there is very little difference between the beam momenta of 158 and 400 GeV/c. This is shown in Fig. 38 which gives the difference in x_F as a function of p_{lab} for the angular range between 70 and 160 degrees.

One example of the apparent s-independence of the backward baryon yields is shown in

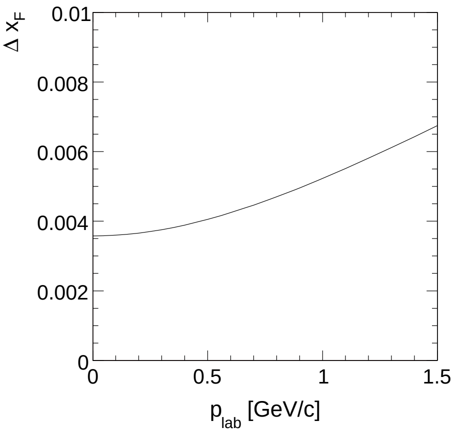

Figure 38: Differences in x_F: $\Delta x_F = x_F^{158} - x_F^{400}$ resulting from the transformation into the cms system between beam momenta of 158 and 400 GeV/c as a function of p_{lab}. The differences are independent of Θ_{lab} in the range $70 < \Theta_{\text{lab}} < 160$ degrees

Fig. 39 which compares data at Θ_{lab} = 162 and 160 degrees for 8.5 [13] and 400 GeV/c beam momentum [7].

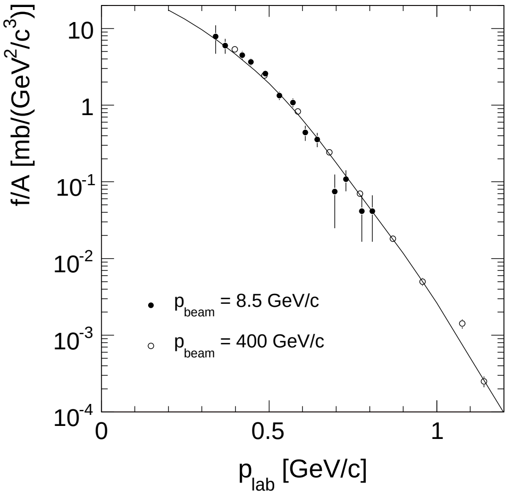

Figure 39: Invariant proton cross sections [13] at Θ_{lab} = 162 degrees and 8.5 GeV/c beam momentum as a function of p_{lab} in comparison with the data from [7] at 160 degrees and 400 GeV/c beam momentum. The full line represents the interpolation of the Fermilab data

Due to the flat angular distribution at Θ_{lab} around 160 degrees, see Fig. 41, the small angular difference in angle between the two measurements has negligible influence on the cross sections comparison. Also the SPS measurements of grey protons by Braune et al. [14] show no dependence on beam momentum in the range from 50 to 150 GeV/c over the complete Θ_{lab} range from 10 to 159 degrees.

7.1 NA49 results at fixed Θ_{lab} and p_{lab} combined with the data from [7]

The kinematic situation presented in Fig. 37 shows that the NA49 acceptance allows the measurement of proton yields as a function of p_{lab} up to Θ_{lab} = 40 degrees. The corresponding data values are tabulated in Table 4.

$f(\Theta_{\text{lab}}, p_{\text{lab}}), \Delta f$								
$p_{\text{lab}} \backslash \Theta_{\text{lab}}$	10^o		20^o		30^o		40^o	
0.3					1.7979	7.58	1.7087	6.20
0.4					1.4154	7.07	1.2310	7.67
0.5			1.2656	11.9	0.8836	7.67	0.8255	8.16
0.6	0.9854	6.11	0.9423	6.94	0.7850	7.20	0.6522	8.22
0.7	0.6654	4.81	0.6714	5.93	0.6167	7.30	0.3868	8.66
0.8	0.6932	7.01	0.5700	6.93	0.4075	8.20	0.2339	17.8
0.9	0.5627	5.12	0.4342	7.44	0.3631	7.99		
1.0	0.4805	7.89	0.3800	7.37	0.2436	9.11		
1.1	0.3810	6.96	0.2932	5.42	0.1924	9.72		
1.2	0.2975	7.23	0.2756	5.22	0.1493	10.4		
1.3	0.3244	6.57	0.2179	5.42	0.0993	12.1		
1.4	0.2578	6.83	0.2147	7.82	0.0670	11.5		
1.5	0.2128	7.19	0.1500	8.87				
1.6			0.1358	8.98				

Table 4: Invariant proton cross sections measured by NA49 at fixed values of Θ_{lab} between 10 and 40 degrees as a for p_{lab} values between from 0.3 to 1.6 GeV/c. The relative statistical errors, Δf, are given in %

These data are shown in Fig. 40 together with the Fermilab data [7] as a function of p_{lab}.

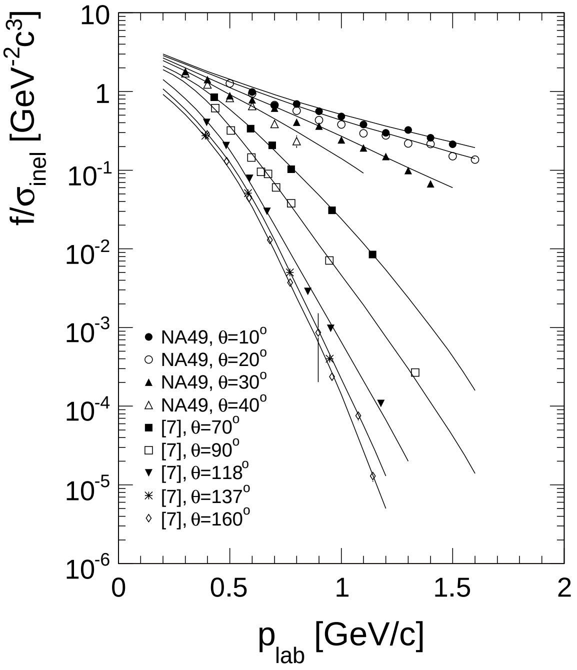

Figure 40: Invariant proton cross sections from NA49 and [7] at lab angles between 10 and 160 degrees as a function of p_{lab}. The data interpolation at fixed angle is given by the full lines

Evidently the two data sets are complementary and offer for the first time an almost complete angular coverage of the backward proton production with double differential cross sections.

A two-dimensional data interpolation has been performed as shown by the full lines in Fig. 40. This allows to produce the combined angular distribution as a function of $\cos(\Theta_{\text{lab}})$ for fixed values of p_{lab} presented in Fig. 41.

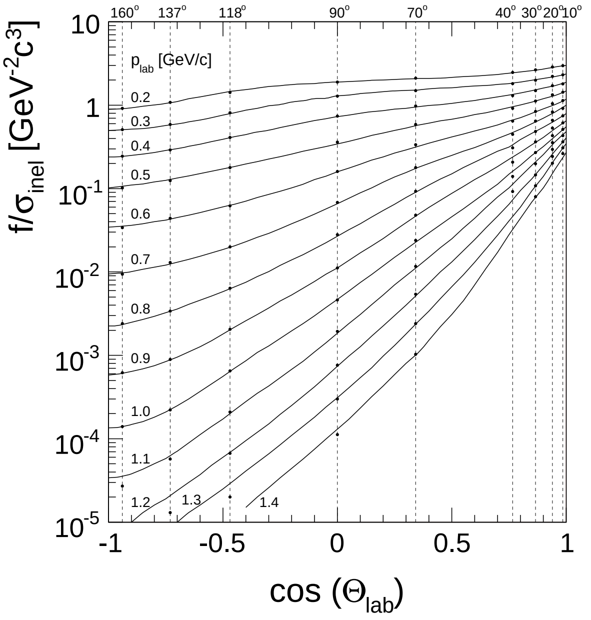

Figure 41: Invariant proton cross sections of the combined NA49 and Fermilab data as a function of $\cos(\Theta_{\text{lab}})$ for fixed values of p_{lab} between 0.2 and 1.4 GeV/c. The data interpolation is shown as full lines

The proton density distributions dn_p/dp_{lab} derived from the interpolated invariant cross sections are shown as a function of p_{lab} in Fig. 42, surface normalized.

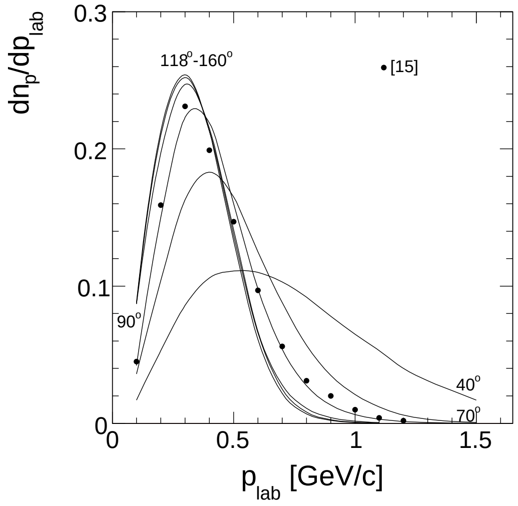

Figure 42: Surface normalized proton density distributions dn_p/dp_{lab} as a function of p_{lab} for fixed Θ_{lab}. The bubble chamber data [15] are shown as full circles

These distributions are closely similar for 160 $> \Theta_{\text{lab}} >$ 118 degrees and develop a tail to large p_{lab} values for angles smaller than 90 degrees indicating increasing contributions from the fragmentation of the participant nucleons hit by the projectile. The ”grey” proton momentum distribution measured in the EHS rapid cycling bubble chamber [15] is positioned close to the Θ_{lab} = 90 degrees result. In this case a strong momentum cut is introduced by requesting bubble densities at 1.3 minimum ionizing rejecting most of the faster forward region.

The dn_p/dp_{lab} distributions shown in Fig. 42 may be integrated over p_{lab} resulting in the proton densities $dn/d\Omega$ shown in Fig. 43 as a function of $cos(\Theta_{\text{lab}})$. Here the integration has been limited to $p_{\text{lab}} < 1.6$ GeV/c as at low angles the target fragmentation contribution will create a divergent behaviour and since the comparison data do not contain this component.

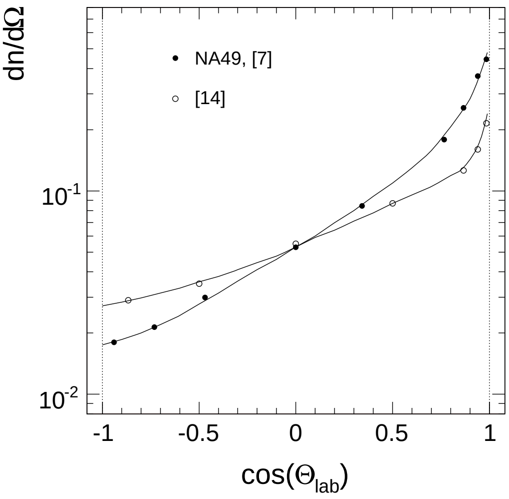

Figure 43: Proton density $dn/d\Omega$ as a function of $cos(\Theta_{\text{lab}})$. Full circles: integrated combined data from NA49 and [7]. Open circles: measurement by Braune et al. [14]

The direct measurements from [14] also presented in Fig. 43 show systematic deviations both at forward and at backward angles. As this experiment uses an energy loss measurement with variable threshold it is not clear to which extent it represents identified proton yields. The authors in fact explain that a contribution from ”evaporation” particles (”black tracks” in emulsion work) cannot be excluded. Such a contribution would typically be characterized by a flatter angular distribution as compared to protons, see also the discussion on light ions in Sect. 8 showing very sizeable d/p ratios. As the d/p and t/p ratios decrease steeply with increasing x_F, see Fig. 45, the yield measured by [14] would increase at $\Theta_{\text{lab}} > 90°$ and decrease towards small angles with respect to the one of identified protons. In addition, a dE/dx cut-off in the detector of [14] will reduce the contribution of fast protons from target fragmentation at small angles.

7.2 Double differential cross section $\mathbf{f(x_F, p_T)}$ as a function of $\mathbf{x_F}$

The invariant cross sections measured in p_{lab} and Θ_{lab} may be transformed into the x_F/p_T variables following the kinematics shown in Fig. 37. The corresponding x_F distributions at fixed p_T are presented in Fig. 44 which shows the x_F range down to -2.0. Both the NA49 data (full circles) and the Fermilab results (open circles) are plotted. The full lines in Fig. 44 represent the interpolation of the two data sets also covering the non-measured angular region between 40 and 70 degrees, see Fig. 41. The thin lines indicate the position of the lab angles of 10, 30, and 50 degrees as well as the five angles measured by [7].

Fig. 44 represents one of the main results of this paper. It shows for the first time a complete coverage of the baryonic phase space in p+A collisions, from x_F = -2 up to the kinematic limit for the projectile fragmentation at $x_F \sim$ +1. Several features merit comment:

- the invariant proton cross sections extend far below the kinematic limit for target fragmentation at x_F = -1

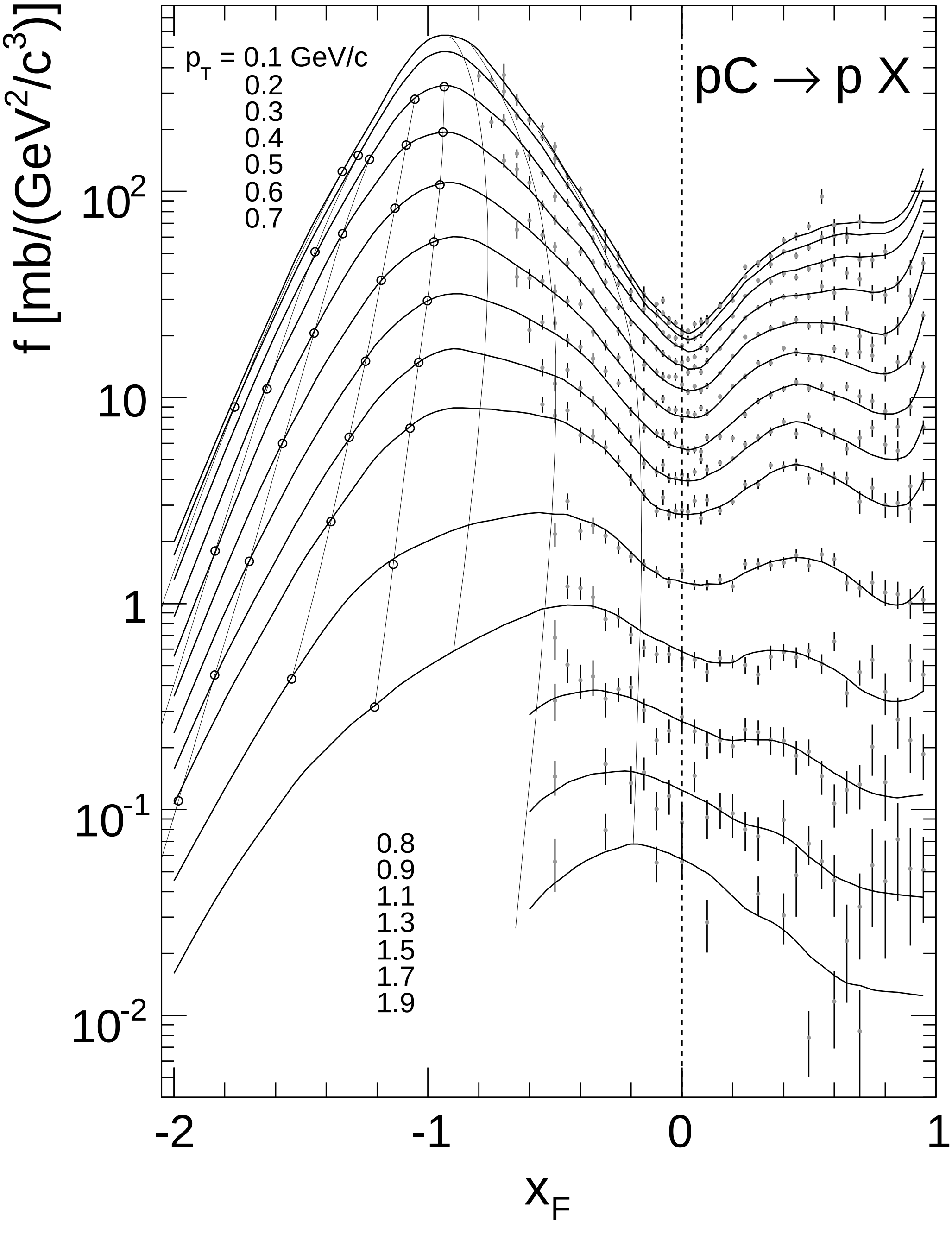

Figure 44: Invariant cross sections at fixed p_T as a function of x_F. Full circles: NA49 data, open circles: data from [7]. The thin lines show the cross section at fixed angles of 10^o, 30^o and 50^o

- there is no indication of a diffractive structure with a peak at $x_F \sim$ -1 as it would be expected from the prompt fragmentation of the hit target nucleons – on the other hand, at $x_F >$ +0.9 there is a diffractive peak in the projectile fragmentation region, see [3] for comparison with p+p interactions
- the backward cross sections peak at $x_F \sim$ -0.9, not at $x_F \sim$ -1 indicating a sizeable longitudinal momentum transfer in the nuclear fragmentation region
- at low p_T or low transverse momentum transfer however, the lines of constant lab angle

are compatible as expected with a convergence towards x_F = -1

A detailed discussion of these features including the de-composition of the measured proton yields into the basic components of projectile, target and nuclear fragmentation, is presented in Sects. 13 and 14.

8 Light ions: deuterons and tritons

As shown in Sect. 4, Fig. 5, the particle identification via energy loss measurement in the NA49 TPC system also allows the extraction of deuteron and triton yields. The accessible kinematic region covers lab momenta from the detector acceptance limit at about 0.25 GeV/c up to the crossing of the energy loss distributions with the ones for electrons, Fig. 3, at about p_{lab} = 2 GeV/c for deuterons and 3 GeV/c for tritons.

As for the proton cross sections, this range is complementary to the Fermilab experiment [8] which gives light ion cross sections in the lab angular range from 70 to 160 degrees, at p_{lab} from 0.5 to 1.3 GeV/c for deuterons and from 0.7 to 1.3 GeV/c for tritons. The NA49 data offer the advantage of reaching low p_T down to 0.1 GeV/c and of covering the forward region from Θ_{lab} = 40 degrees down to about 3 degrees. This allows for the first time to trace the extension of nuclear fragmentation into light ions towards the central region of particle production.

8.1 Ion to proton ratios

In order to clearly bring out the last aspect mentioned above the deuteron and triton yields are given here as ratios to the proton yields in each bin of p_{lab} and Θ_{lab},

$$R_d(x_F, p_T) = \frac{(dn/dp_{\mathrm{lab}} d\Omega)_d}{(dn/dp_{\mathrm{lab}} d\Omega)_p} \tag{4}$$

$$R_t(x_F, p_T) = \frac{(dn/dp_{\mathrm{lab}} d\Omega)_t}{(dn/dp_{\mathrm{lab}} d\Omega)_p} \tag{5}$$

These density ratios are given as functions of x_F and p_T using the proton mass in the transformation from lab to cms variables. They thus give directly the relative contribution of the light ions with respect to protons in the x_F/p_T bins shown in Fig. 2 and Table 2. In forming the ion/proton density ratios, most of the data corrections, Sect. 5, drop out with the exception of absorption which is small but increased for ions, and of hyperon feed-down which is of course only applicable to protons. The resulting ratios are shown as functions of x_F and p_T in Table 5 for deuterons and in Table 6 for tritons.

$R_d(x_F, p_T), \Delta R_d$											
$p_T \backslash x_F$	-0.8	-0.75	-0.7	-0.65	-0.6	-0.55	-0.5	-0.45	-0.4	-0.35	-0.3	-0.25
0.1	11.5 2.1	10.8 2.2	9.08 1.9	14.46 2.6	5.04 1.4	6.20 1.6	8.10 0.9	5.76 0.9	4.80 0.9	5.85 1.0	4.85 1.1	
0.2	12.0 1.3	14.0 1.5	12.4 1.2	9.95 1.2	8.59 1.1	8.02 1.1	6.88 0.8	8.23 1.1	5.09 0.9	7.39 1.7	4.18 1.5	
0.3	10.3 2.0	11.7 1.4	8.8 1.1	9.72 1.1	7.52 1.1	8.41 1.1	8.00 1.1	4.42 1.0	4.95 0.8	4.18 1.0	3.35 1.2	2.90 0.6
0.4		8.5 2.1	6.7 1.1	12.32 1.5	8.12 1.3	8.01 1.2	8.29 1.7	6.39 1.2	5.58 1.2	4.95 1.0	1.72 0.5	
0.5			7.7 1.9	5.97 1.2	7.07 1.2	5.91 1.4	6.98 1.7	3.43 1.1	8.10 1.5	4.02 0.9	1.90 0.6	
0.6				11.43 2.5	6.46 2.9	7.04 1.8	4.56 1.4	4.22 1.1	2.65 0.9	5.03 1.3	1.79 0.8	
0.7					9.26 4.0	9.28 2.9	7.38 2.5	7.65 2.4	3.72 1.5			
0.8						8.84 3.4	2.67 1.4	3.68 1.5	5.20 2.1			
0.9						4.88 2.0	3.73 1.5					
1.1							3.84 2.6					

Table 5: d/p density ratios $R_d(x_F, p_T)$ and their statistical errors ΔR_d in percent as a function of x_F and p_T using proton mass in the transformation from lab to cms system

$R_t(x_F, p_T), \Delta R_t$											
$p_T \backslash x_F$	-0.8	-0.75	-0.7	-0.65	-0.6	-0.55	-0.5	-0.45	-0.4	-0.35	-0.3
0.1	1.22 0.1		1.74 0.9	0.79 0.5		1.18 0.7	1.00 0.3	0.44 0.2	0.31 0.2	0.45 0.3	
0.2	1.12 0.4	2.24 0.6	0.96 0.3	2.39 0.5	1.80 0.5	0.96 0.4	0.76 0.2	1.22 0.4	0.28 0.2	0.34 0.3	
0.3	1.73 0.8	2.14 0.6	2.46 0.6	2.50 0.6	1.27 0.4	1.61 0.5	0.44 0.2	1.06 0.4	0.15 0.1	0.28 0.2	0.41 0.3
0.4		1.02 0.7	0.82 0.4	1.35 0.5	1.27 0.5	0.69 0.3	0.99 0.5	0.43 0.3	0.73 0.4	0.40 0.3	0.47 0.2
0.5				2.08 0.8	1.16 0.5	0.33 0.3	0.67 0.4	0.38 0.3		0.20 0.2	0.36 0.2
0.6						0.45 0.4		0.48 0.4			

Table 6: t/p density ratios $R_t(x_F, p_T)$ and their statistical errors ΔR_t in percent as a function of x_F and p_T using proton mass in the transformation from lab to cms system

In these data tables the cut-offs imposed by the NA49 acceptance at $\Theta_{\text{lab}} \sim 40$ degrees below $x_F \sim$ -0.5 and by the upper limit on p_{lab} imposed by the energy loss measurement at $x_F \gtrsim$ -0.5 are discernible. In addition the fast decrease of the ratios towards higher x_F limits the extraction of tritons due to the low overall event statistics.

8.2 Comparison to the Fermilab data [8]

The density ratios $R_d(x_F, p_T)$ and $R_t(x_F, p_T)$ are presented in Fig. 45 as a function of x_F in comparison to the Fermilab data which are available above $p_T \sim 0.3$ GeV/c.

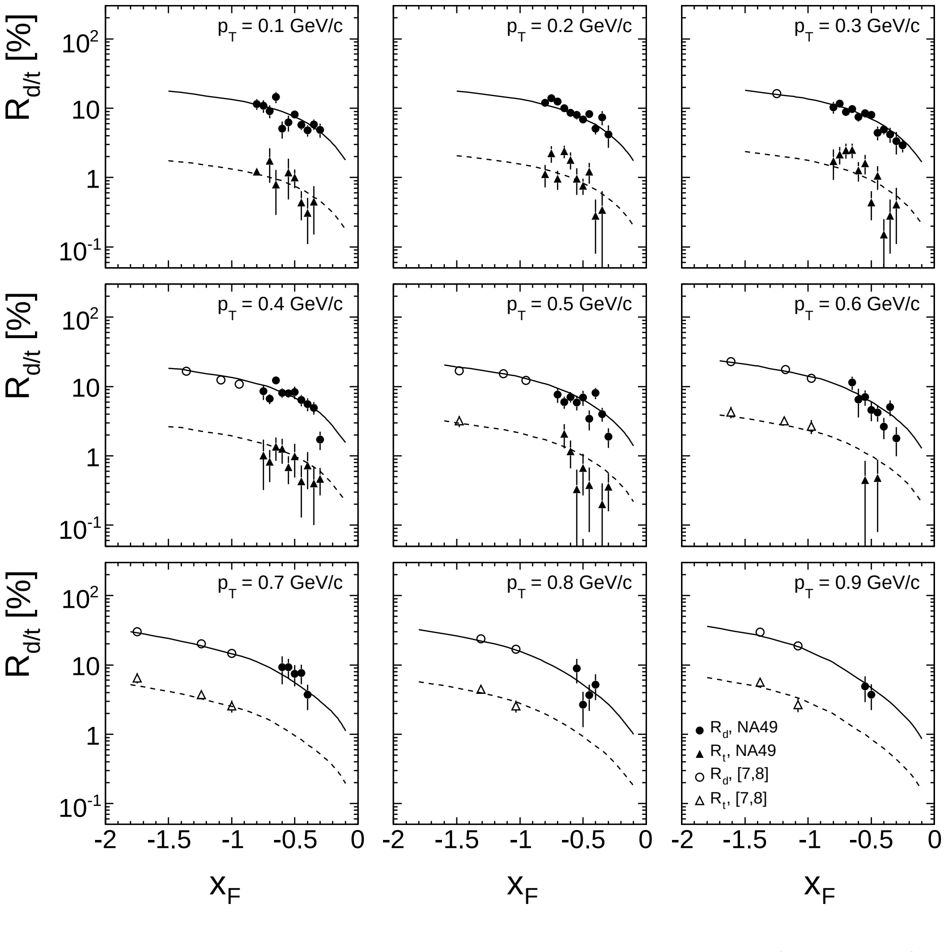

Figure 45: Deuteron and triton to proton density ratios R_d and R_t as a function of x_F for fixed values of p_T between 0.1 and 0.9 GeV/c. The full lines give the two-dimensional data interpolation established for R_d, the broken lines are the same multiplied by the suppression factors shown in Fig. 46

As for the proton data, the good consistency with the Fermilab data in the p_T range above 0.3 GeV/c is confirmed for R_d by the two-dimensional data interpolation shown as the full lines in Fig. 45. R_t shows a similar consistency with [8] over the smaller available region of comparison due to the higher p_{lab} cutoff in the Fermilab data. With respect to R_d, R_t is suppressed by a factor of 0.1 to 0.2 depending on p_T but within statistics independent of x_F. This is demonstrated by the broken lines in Fig. 45 which represent the interpolation of R_d with the suppression factors $R_t/R_d^{\mathrm{interpol}}$ given as a function of p_T in Fig. 46.

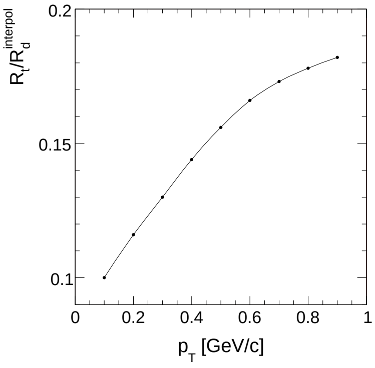

Figure 46: Triton suppression factor $R_t/R_d^{\mathrm{interpol}}$ as a function of p_T

8.3 $\mathbf{x_F}$ and $\mathbf{p_T}$ dependences

The x_F dependences of the density ratios presented in Fig. 45 show a rather complex behaviour. Evidently deuterons and tritons, if seen as nuclear fragments as opposed to coalescing from produced baryons, reach far towards central production. In consequence the separation of nuclear fragmentation and coalescence is not an easy affair especially as fragmentation products, as shown by the tentative extrapolation of the data interpolation towards x_F = -0.1, might well represent a contribution in the sub-percent range even at x_F = 0 and already for the light Carbon nuclei at SPS energy. The p_T dependence of R_d at fixed x_F is as well non-trivial, as shown in Fig. 47.

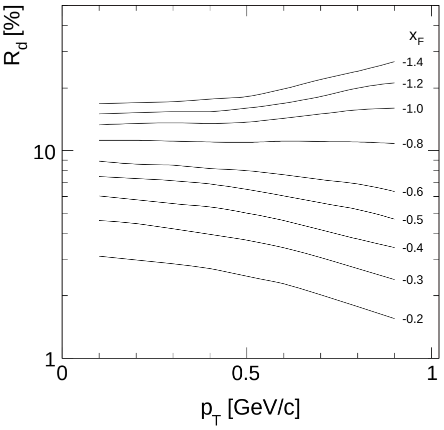

Figure 47: R_d as a function of p_T for fixed values of x_F between -1.4 and -0.2

Evidently R_d tends to decrease with increasing p_T for $x_F >$ -0.8, this tendency inverting itself for $x_F <$ -0.8. The R_t/R_d ratio on the other hand clearly increases with p_T at all available x_F values, see Fig. 46.

9 Particle ratios

The already published data on p+C [4, 5] and p+p [1–3] interactions allow for a very detailed study of particle ratios. In a first overview baryonic ratios will be investigated in this section, both concerning anti-proton/proton ratios in elementary and nuclear collisions,

$$R^{\mathrm{pC}}_{\overline{\mathrm{p}}\mathrm{p}} = f^{\mathrm{pC}}_{\overline{\mathrm{p}}}(x_F, p_T)/f^{\mathrm{pC}}_{\mathrm{p}}(x_F, p_T) \tag{6}$$

$$R^{\mathrm{pp}}_{\overline{\mathrm{p}}\mathrm{p}} = f^{\mathrm{pp}}_{\overline{\mathrm{p}}}(x_F, p_T)/f^{\mathrm{pp}}_{\mathrm{p}}(x_F, p_T) \tag{7}$$

and baryon density ratios directly comparing p+C and p+p reactions,

$$R_{\overline{\mathrm{p}}} = f^{\mathrm{pC}}_{\overline{\mathrm{p}}}(x_F, p_T)/f^{\mathrm{pp}}_{\overline{\mathrm{p}}}(x_F, p_T) \tag{8}$$

$$R_{\mathrm{p}} = f^{\mathrm{pC}}_{\mathrm{p}}(x_F, p_T)/f^{\mathrm{pp}}_{\mathrm{p}}(x_F, p_T). \tag{9}$$

Fig. 48 shows $R^{\mathrm{pC}}_{\overline{\mathrm{p}}\mathrm{p}}$ (closed circles) and $R^{\mathrm{pp}}_{\overline{\mathrm{p}}\mathrm{p}}$ (open circles) together with the corresponding ratios of the data interpolation (full and broken lines) as a function of x_F for several bins of p_T.

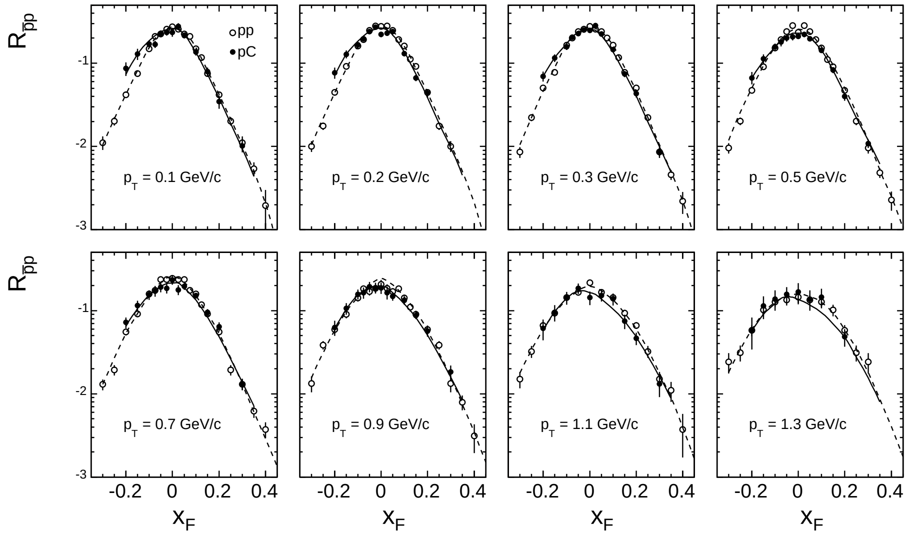

Figure 48: $R_{\overline{\mathrm{p}}\mathrm{p}}$ as a function of x_F for 8 values of p_T comparing p+C (closed circles) and p+p (open circles) interactions. The corresponding ratios of the data interpolations are shown as full lines (p+C) and broken lines (p+p)

This comparison reveals that the ratios are within errors equal in the projectile hemisphere $x_F \gtrsim 0.1$ with the exception of the two highest p_T bins. This means that the transfer of projectile baryon number (”stopping”) towards the central region is equal for protons and for anti-protons. In the backward hemisphere there are distinct differences between p+C and p+p interactions at low to medium p_T. This is a result of isospin effects between the isoscalar C and the p targets. In fact it is known that the anti-proton yields increase and the proton yields decrease in neutron fragmentation [12] with both effects increasing $R^{\mathrm{pC}}_{\overline{\mathrm{p}}\mathrm{p}}$ compared to $R^{\mathrm{pp}}_{\overline{\mathrm{p}}\mathrm{p}}$. The clean extraction of p̄ and p yields in the far backward direction, $x_F <$ -0.4, see Sect. 4 and Fig. 5, allows the extension of $R^{\mathrm{pC}}_{\overline{\mathrm{p}}\mathrm{p}}$ to the x_F range -0.7 $< x_F <$ -0.5. This is presented in Fig. 49 in the p_T interval 0.1 $< p_T <$ 0.4 GeV/c.

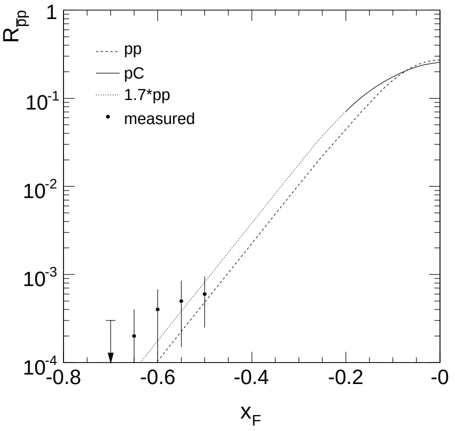

Figure 49: $R^{\mathrm{pC}}_{\overline{\mathrm{p}}\mathrm{p}}$ in the intervals -0.7 $< x_F <$ -0.5 and 0.1 $< p_T <$ 0.4 GeV/c together with $R^{\mathrm{pC}}_{\overline{\mathrm{p}}\mathrm{p}}$ (full line), $R^{\mathrm{pp}}_{\overline{\mathrm{p}}\mathrm{p}}$ (broken line) [3] and $1.7R^{\mathrm{pp}}_{\overline{\mathrm{p}}\mathrm{p}}$ (dotted line)

The broken line represents $R^{\mathrm{pp}}_{\overline{\mathrm{p}}\mathrm{p}}$ [3], the full line the measured $R^{\mathrm{pC}}_{\overline{\mathrm{p}}\mathrm{p}}$ and the dotted line $R^{\mathrm{pp}}_{\overline{\mathrm{p}}\mathrm{p}}$ multiplied by a factor 1.7 which stems from the expected increase in p̄ yield (factor 1.33, [12]) and the decrease in p yield (factor 1.3, [3]) from the isoscalar C nucleus. The fact that the measured backward ratio follows closely the expectation from target fragmentation shows that there is no p̄ production from nuclear cascading. This is in agreement with the upper limit of $R^{\mathrm{pC}}_{\overline{\mathrm{p}}\mathrm{p}}$ of 10^{-4} to 10^{-5} given in [16] for p+^{181}Ta at 90 degrees laboratory angle.

In contrast to the p̄/p ratios discussed above, the baryon yields proper exhibit an important evolution when passing from p+p to p+C interactions. This is presented as functions of x_F for fixed values of p_T in Fig. 50 for R_{p} and in Fig. 51 for $R_{\overline{\mathrm{p}}}$.

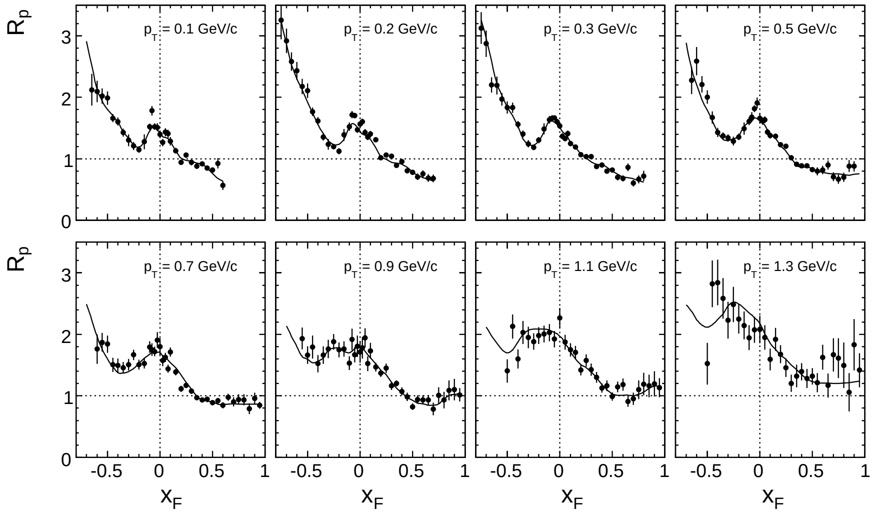

Figure 50: R_p as a function of x_F for fixed p_T values between 0.1 and 1.3 GeV/c. The full lines give the ratios for the corresponding data interpolations

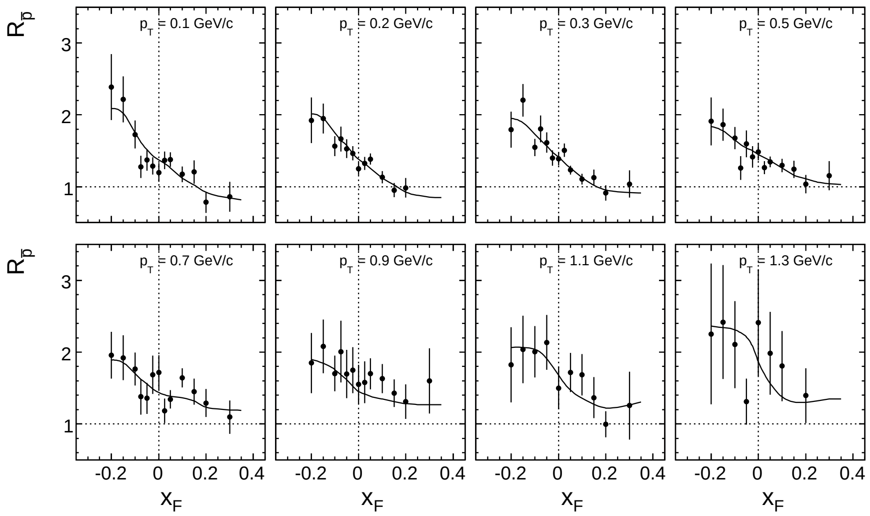

Figure 51: $R_{\overline{\mathrm{p}}}$ as a function of x_F for fixed p_T values between 0.1 and 1.3 GeV/c. The full lines give the ratios for the corresponding data interpolations

Looking first at R_{p}, Fig. 50, where the data give access to a very wide range of x_F, three distinct zones may be distinguished.

A first area is governed by the projectile fragmentation, $x_F \gtrsim$ 0.1. Here the transfer of baryon number from the forward to the central region is clearly evident, with a suppression of the far forward yield by a factor of 0.6 at low to medium p_T followed by a steady increase of proton density with increasing p_T until the densities exceed the p+p values at all x_F for $p_T >$ 1 GeV/c.

A second area is characterized by the fragmentation of the target nucleons hit by the projectile, -0.5 $< x_F <$ 0. Here the pile-up of produced hadrons in the central area due to the 1.6 mean projectile collisions in the C nucleus is visible, followed by a steady decrease of proton density in the backward direction due to the contribution of neutron fragmentation.

A third component is characterized by the steep increase of proton density for $x_F <$ -0.2, at low to medium p_T. This region is governed by the intranuclear cascading of baryons (”grey protons”) in the lab momentum range up to about 2 GeV/c. This component dies out as expected with increasing transverse momentum.

Due to the smaller x_F range experimentally available for the anti-protons, the corresponding ratio $R_{\overline{\mathrm{p}}}$ is more restricted. It has however been demonstrated (Fig. 49) that here no cascading component exists. As argued above, the evolution of the projectile fragmentation ($x_F \gtrsim$ 0.1) follows closely the one for protons including the increase with transverse momentum. As far as the target fragmentation is concerned, the increase of anti-proton density beyond the pile-up from the 1.6 average projectile collisions to about a factor of 2 is expected from isospin symmetry.

A further, more detailed argumentation concerning this phenomenology can be found in the discussion Sect. 12 below.

10 Integrated data

10.1 $\mathbf{p_T}$ integrated distributions

The p_T integrated non-invariant and invariant yields are defined by:

$$dn/dx_F = \pi/\sigma_{\text{inel}} \cdot \sqrt{s}/2 \cdot \int f/E \cdot dp_T^2$$
$$F = \int f \cdot dp_T^2 \qquad (10)$$
$$dn/dy = \pi/\sigma_{\text{inel}} \cdot \int f \cdot dp_T^2$$

with $f = E \cdot d^3\sigma/dp^3$, the invariant double differential cross section. The integrations are performed numerically using the two-dimensional data interpolation (Sect. 6.2). Tables 7 and 8 give the numerical values and the first and second moments of the p_T distributions as functions of x_F and rapidity for protons and anti-protons, respectively. The relative errors quoted are given in percent using the full statistical errors of the measured points. They thus present upper

p												
x_F	F [mb·c]	Δ	dn/dx_F	Δ	$\langle p_T \rangle$	Δ	$\langle p_T^2 \rangle$	Δ	y	dn/dy	y	dn/dy
-0.8	81.6	4.8	1.400	4.8	0.391	2.1	0.208	1.2	-3.2	0.21949	0.8	0.12875
-0.75	73.2	4.5	1.337	4.5	0.402	1.8	0.220	2.9	-3.1	0.43696	0.9	0.13405
-0.7	65.4	3.8	1.278	3.8	0.414	1.6	0.232	2.5	-3.0	0.76998	1.0	0.14070
-0.65	57.0	2.9	1.198	2.9	0.428	1.3	0.249	2.3	-2.9	1.09283	1.1	0.14866
-0.6	50.4	2.9	1.142	2.9	0.442	1.2	0.266	2.1	-2.8	1.23706	1.2	0.15804
-0.55	43.8	2.0	1.079	2.0	0.458	0.82	0.285	1.5	-2.7	1.20270	1.3	0.16829
-0.5	37.7	2.1	1.018	2.1	0.477	0.91	0.308	1.8	-2.6	1.06937	1.4	0.18043
-0.45	32.8	1.8	0.975	1.8	0.494	0.93	0.329	1.9	-2.5	0.91240	1.5	0.19426
-0.4	28.22	1.7	0.935	1.7	0.508	0.80	0.348	1.7	-2.4	0.77367	1.6	0.20672
-0.35	23.92	1.6	0.892	1.6	0.523	0.85	0.369	1.7	-2.3	0.65943	1.7	0.21800
-0.3	19.83	1.8	0.844	1.8	0.538	0.94	0.391	1.9	-2.2	0.56603	1.8	0.22892
-0.25	16.57	1.4	0.818	1.4	0.547	0.76	0.403	1.7	-2.1	0.49330	1.9	0.23773
-0.2	13.88	1.4	0.808	1.4	0.554	0.68	0.414	1.5	-2.0	0.43602	2.0	0.24016
-0.15	11.80	2.1	0.825	2.1	0.554	0.92	0.415	1.7	-1.9	0.38870	2.1	0.23634
-0.1	10.31	1.4	0.873	1.4	0.551	0.60	0.411	1.3	-1.8	0.34565	2.2	0.23645
-0.075	9.71	1.6	0.900	1.5	0.551	0.59	0.410	1.1	-1.7	0.30284	2.3	0.23584
-0.05	9.26	1.1	0.927	1.0	0.549	0.63	0.407	1.4	-1.6	0.26883	2.4	0.23145
-0.025	8.90	1.6	0.938	1.6	0.550	0.61	0.407	1.2	-1.5	0.24220	2.5	0.22097
0.0	8.67	1.5	0.931	1.4	0.551	0.59	0.407	1.1	-1.4	0.22093		
0.025	8.49	1.5	0.893	1.4	0.555	0.68	0.412	1.3	-1.3	0.20292		
0.05	8.53	1.2	0.852	1.2	0.555	0.63	0.412	1.3	-1.2	0.18852		
0.075	8.68	1.3	0.804	1.3	0.555	0.64	0.412	1.2	-1.1	0.17704		
0.1	9.07	1.3	0.768	1.3	0.553	0.75	0.409	1.6	-1.0	0.16671		
0.15	10.16	1.0	0.712	0.9	0.545	0.54	0.396	1.2	-0.9	0.15776		
0.2	11.60	0.9	0.677	0.9	0.538	0.54	0.385	1.2	-0.8	0.14975		
0.25	13.42	1.0	0.663	0.9	0.531	0.45	0.374	1.0	-0.7	0.14307		
0.3	14.87	1.1	0.633	1.1	0.528	0.53	0.370	1.2	-0.6	0.13782		
0.35	16.20	1.4	0.604	1.4	0.525	0.68	0.365	1.4	-0.5	0.13390		
0.4	17.20	1.1	0.569	1.1	0.521	0.60	0.360	1.3	-0.4	0.13026		
0.45	17.74	1.4	0.527	1.4	0.519	0.65	0.357	1.3	-0.3	0.12706		
0.5	17.93	1.3	0.483	1.3	0.511	0.63	0.348	1.2	-0.2	0.12485		
0.55	17.96	2.2	0.442	2.2	0.499	1.1	0.334	1.9	-0.1	0.12318		
0.6	17.90	2.4	0.406	2.4	0.488	0.98	0.321	1.7	0.0	0.12157		
0.65	17.59	2.6	0.369	2.6	0.479	0.87	0.310	1.7	0.1	0.12065		
0.7	17.00	3.0	0.332	3.0	0.470	1.3	0.300	2.3	0.2	0.11939		
0.75	16.48	3.4	0.301	3.4	0.461	1.3	0.290	2.7	0.3	0.11861		
0.8	16.40	3.7	0.282	3.7	0.455	1.2	0.282	2.6	0.4	0.11907		
0.85	17.42	4.2	0.282	4.2	0.449	1.0	0.274	2.2	0.5	0.11975		
0.9	20.6	4.0	0.315	4.0	0.440	1.3	0.261	3.0	0.6	0.12154		
0.95	29.5	3.4	0.428	3.4	0.432	0.75	0.248	1.7	0.7	0.12474		

Table 7: p_T integrated invariant cross section F [mb·c], density distribution dn/dx_F, mean transverse momentum $\langle p_T \rangle$ [GeV/c], mean transverse momentum squared $\langle p_T^2 \rangle$ [(GeV/c)^2] as a function of x_F, as well as density distribution dn/dy as a function of y for p. The statistical uncertainty Δ for each quantity is given in % as an upper limit considering the full statistical error of each measured p_T/x_F bin

limits as the data interpolation in x_F will reduce the statistical fluctuations for the p_T integrated quantities.

p̄												
x_F	F [mb·c]	Δ	dn/dx_F	Δ	$\langle p_T \rangle$	Δ	$\langle p_T^2 \rangle$	Δ	y	dn/dy	y	dn/dy
-0.2	0.910	5.7	0.0533	5.7	0.528	3.3	0.375	6.4	-1.1	0.01399	0.4	0.02215
-0.15	1.282	3.9	0.0905	3.8	0.524	2.1	0.371	4.2	-1.0	0.01692	0.5	0.02054
-0.1	1.627	3.2	0.1395	3.1	0.518	1.7	0.361	3.4	-0.9	0.01915	0.6	0.01876
-0.075	1.780	3.6	0.1676	3.7	0.513	1.6	0.353	3.2	-0.8	0.02118	0.7	0.01689
-0.05	1.902	3.1	0.1940	3.0	0.507	1.4	0.344	2.7	-0.7	0.02284	0.8	0.01492
-0.025	1.940	2.9	0.2094	2.8	0.505	1.4	0.338	2.7	-0.6	0.02419	0.9	0.01295
0.0	1.903	2.9	0.2095	2.7	0.502	1.6	0.333	3.4	-0.5	0.02546	1.0	0.01106
0.025	1.815	3.0	0.1959	2.8	0.505	1.6	0.335	3.2	-0.4	0.02638	1.1	0.00924
0.05	1.607	2.2	0.1642	2.0	0.507	1.4	0.338	2.9	-0.3	0.02690	1.2	0.00748
0.1	1.183	2.4	0.1014	2.3	0.524	1.2	0.359	2.5	-0.2	0.02711	1.3	0.00595
0.15	0.798	3.0	0.0562	3.0	0.543	1.6	0.382	3.3	-0.1	0.02702	1.4	0.00457
0.2	0.506	4.1	0.0295	4.0	0.558	2.1	0.403	3.7	0.0	0.02656	1.5	0.00332
0.3	0.179	6.0	0.0076	6.0	0.570	2.8	0.428	5.0	0.1	0.02609	1.6	0.00225
									0.2	0.02524	1.7	0.00132
									0.3	0.02381		

Table 8: p_T integrated invariant cross section F [mb·c], density distribution dn/dx_F, mean transverse momentum $\langle p_T \rangle$ [GeV/c], mean transverse momentum squared $\langle p_T^2 \rangle$ [(GeV/c)^2] as a function of x_F, as well as density distribution dn/dy as a function of y for p̄. The statistical uncertainty Δ for each quantity is given in % as an upper limit considering the full statistical error of each measured p_T/x_F bin

Concerning the extension of the kinematic coverage into the far backward direction for protons, $x_F < -0.8$, see Sect. 7, additional integrated quantities are given in Table 9 for $-2.0 \leq x_F \leq -0.9$. Again, the data interpolation is used to obtain the numerical values.

p								
x_F	F	Δ	dn/dx_F	Δ	$\langle p_T \rangle$	Δ	$\langle p_T^2 \rangle$	Δ
-2.0	0.466	3.0	0.00323	3.0	0.482	2.0	0.320	3.0
-1.8	1.816	3.0	0.01398	3.0	0.457	2.0	0.283	3.0
-1.6	6.51	3.0	0.0563	3.0	0.435	2.0	0.251	3.0
-1.5	11.46	3.0	0.1057	3.0	0.424	2.0	0.240	3.0
-1.4	19.49	3.0	0.1926	3.0	0.417	2.0	0.230	3.0
-1.3	31.6	3.0	0.336	3.0	0.409	2.0	0.220	3.0
-1.2	48.9	3.0	0.564	3.0	0.400	2.0	0.211	3.0
-1.1	71.0	3.0	0.890	3.0	0.384	2.0	0.197	3.0
-1.0	88.8	3.0	1.224	3.0	0.374	2.0	0.189	3.0
-0.9	93.0	3.0	1.422	3.0	0.378	2.0	0.194	3.0

Table 9: p_T integrated invariant cross section F [mb·c], density distribution dn/dx_F, mean transverse momentum $\langle p_T \rangle$ [GeV/c], mean transverse momentum squared $\langle p_T^2 \rangle$ [(GeV/c)^2] as a function of x_F for protons in the far backward region. The estimated relative statistical uncertainties Δ are given in %

In this region the estimation of the statistical uncertainties is non-trivial as the measured data have been transformed from the laboratory co-ordinates (p_{lab},Θ_{lab}) to the cms quantities (x_F,p_T) using a two-dimensional interpolation. The given errors have been obtained from the total number of measured protons at each lab angle [8] which varies from about 1100 to 3600. The values given in Table 9 are therefore to be regarded as upper limits.

The corresponding distributions for dn/dx_F, F and dn/dy are shown in Fig. 52 for protons and in Fig. 53 for anti-protons.

The p_T integrated p̄/p ratios as a function of x_F are shown in Fig. 54. The first and second moments $\langle p_T \rangle$ and $\langle p_T^2 \rangle$ are presented as a function of x_F in Fig. 55 for protons and in Fig. 56 for anti-protons.

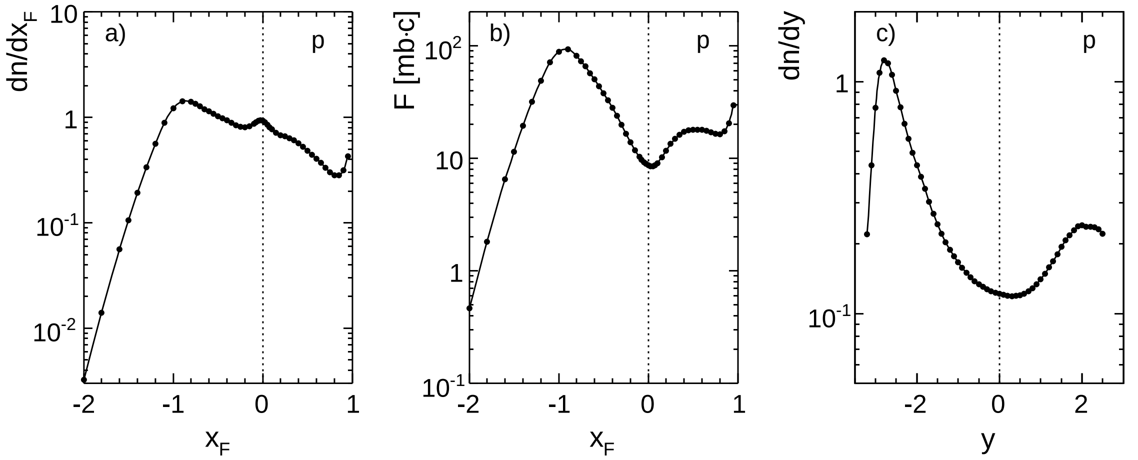

Figure 52: p_T integrated distributions a) dn/dx_F, b) F and c) dn/dy for protons as a function of x_F and y, respectively

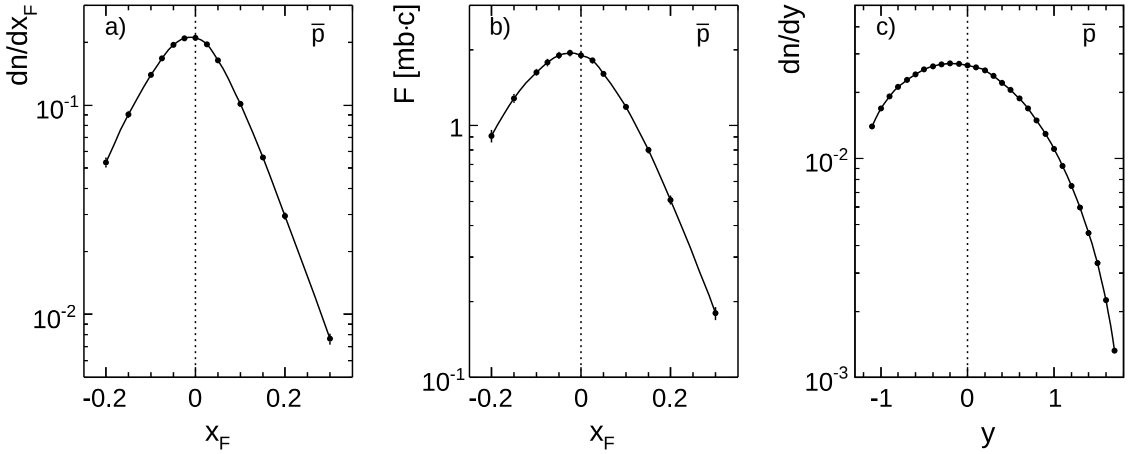

Figure 53: p_T integrated distributions a) dn/dx_F, b) F and c) dn/dy for anti-protons as a function of x_F and y, respectively

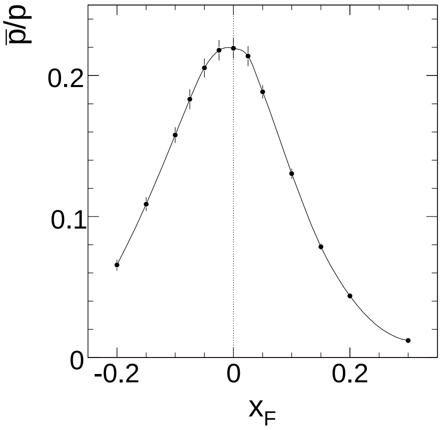

Figure 54: The p_T integrated p̄/p ratios as a function of x_F

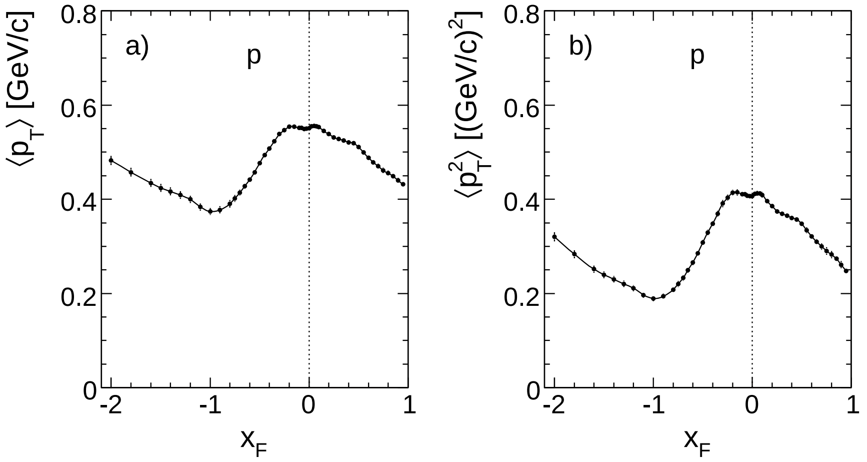

Figure 55: a) mean p_T and b) mean p_T^2 for protons as a function of x_F

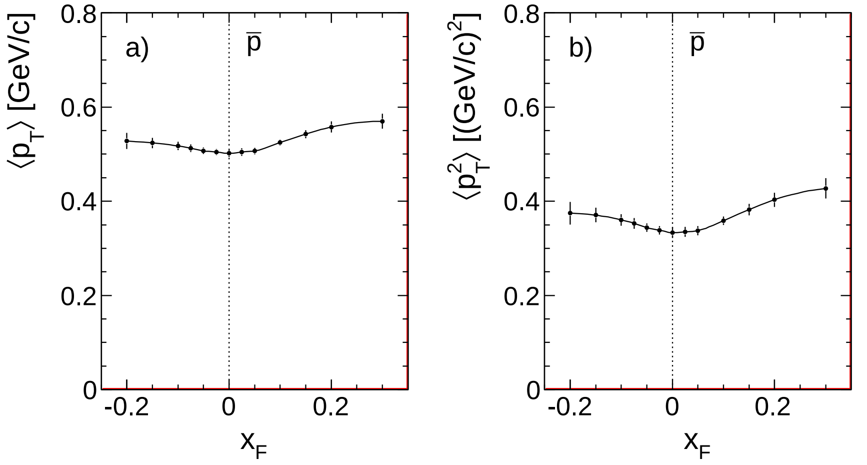

Figure 56: a) mean p_T and b) mean p_T^2 for anti-protons as a function of x_F

10.2 Centrality dependence

The detection of ”grey” protons in the centrality detector of NA49 [10] allows the study of particle densities as a function of the number n_{grey} of protons in the lab momentum range of approximately 0.15 to 1.2 GeV/c. The number distribution dN/dn_{grey} has been shown in [4] to be a steep function of n_{grey} with only 20% and 5% of all events at n_{grey} = 1 and 2, respectively. The determination of double differential cross sections is therefore not feasible in this experiment. As already shown in [4] for pions, the extraction of p_T integrated yields as a function of x_F by fitting the dE/dx distributions over the complete range of p_T is however feasible in a limited range of x_F. This range is determined by the variation of total momentum with p_T and extends from x_F = -0.2 to +0.65 for protons, the upper limit being imposed by the progressive loss of acceptance at low p_T. Two samples with $n_{\mathrm{grey}} \geq 1$ and $n_{\mathrm{grey}} \geq 2$ have been selected. The resulting proton density distributions dn/dx_F are given after correction in Table 10, with the additional use of the complete data sample (see also [4]) which allows for a precise control of eventual systematic effects.

As shown in Fig. 57, the results for the total data sample are compatible within errors with the integration of the data interpolation, Table 7 and Fig. 52.

x_F	$(dn/dx_F)^{\text{all}}$	Δ	$(dn/dx_F)^{n_{\text{cd}}\geq 1}$	Δ	$(dn/dx_F)^{n_{\text{cd}}\geq 2}$	Δ
-0.2	0.797	3.8	1.210	5.3	1.388	8.2
-0.15	0.858	2.4	1.225	5.4	1.461	8.8
-0.1	0.827	3.3	1.230	5.2	1.401	10.1
-0.05	0.852	3.2	1.247	4.6	1.373	8.9
0.0	0.923	3.0	1.167	2.7	1.285	6.0
0.05	0.867	1.5	1.143	2.4	1.201	4.6
0.1	0.774	1.4	0.975	2.2	1.055	4.0
0.15	0.725	1.4	0.824	2.4	0.903	4.7
0.2	0.678	1.5	0.800	2.4	0.838	4.8
0.25	0.682	1.5	0.758	2.5	0.738	5.0
0.3	0.636	1.6	0.649	2.7	0.615	5.5
0.35	0.594	1.5	0.597	2.9	0.541	6.1
0.4	0.579	1.6	0.532	3.0	0.519	6.2
0.45	0.510	1.6	0.462	3.2	0.426	6.8
0.5	0.478	1.7	0.451	3.3	0.424	7.2
0.55	0.441	1.8	0.384	3.7	0.360	7.5
0.6	0.423	2.8	0.388	5.7	0.261	13.7
0.65	0.383	3.4	0.312	6.8	0.298	13.4

Table 10: dn/dx_F distributions for protons as a function of x_F for the complete data sample and the selections $n_{\text{grey}} \geq 1$ and $n_{\text{grey}} \geq 2$. The relative statistical errors are given in %

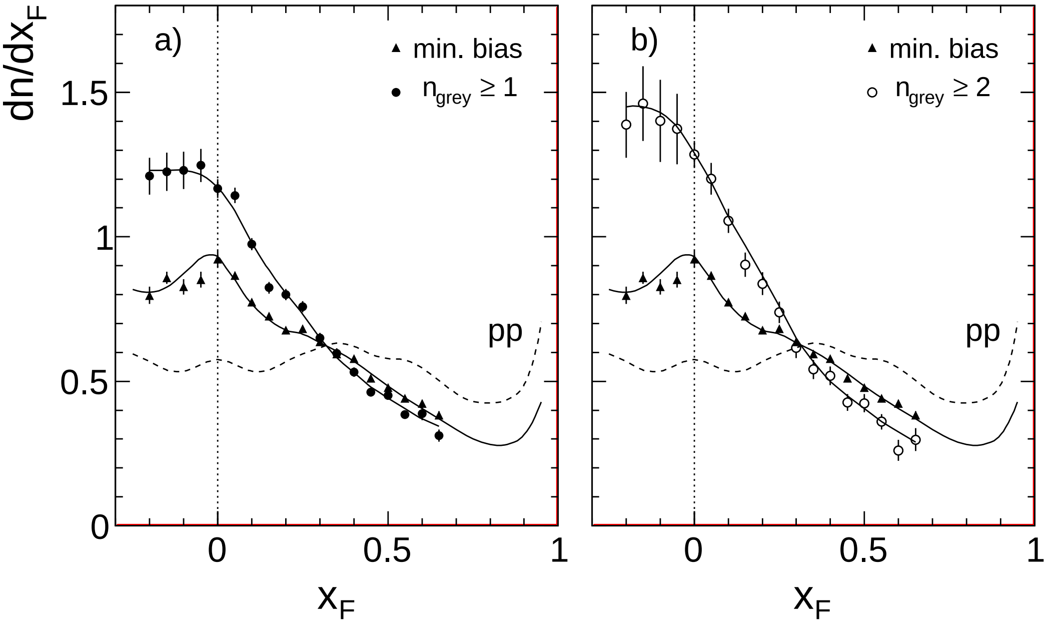

Figure 57: dn/dx_F for protons as a function of x_F for the complete data sample and for the conditions a) $n_{\text{grey}} \geq 1$ and b) $n_{\text{grey}} \geq 2$. The broken line gives the density in p+p collisions [3] and the full line the integration of the interpolated p+C data

As seen from Fig. 57, a systematic and smooth variation of the proton density distributions is evident when passing from p+p to minimum bias p+C and to centrality enhanced p+C interactions. A well defined cross-over with equal number density is visible at x_F = 0.25 ÷ 0.3. Above this value the densities decrease progressively with increasing number of projectile collisions by up to a factor of 0.5 at the experimentally accessible limit of x_F = 0.6. Below x_F = 0.3 this trend is inverted with a density increase of up to factors of 2.5 at negative x_F.

A similar behaviour is also seen for anti-protons, although here only a reduced range in x_F is accessible due to the limiting statistical uncertainties. This is shown in Fig. 58 where the relative difference in baryon density between the n_{grey} selected and minimum bias samples is given in % as a function of x_F for protons (panel a) and anti-protons (panel b).

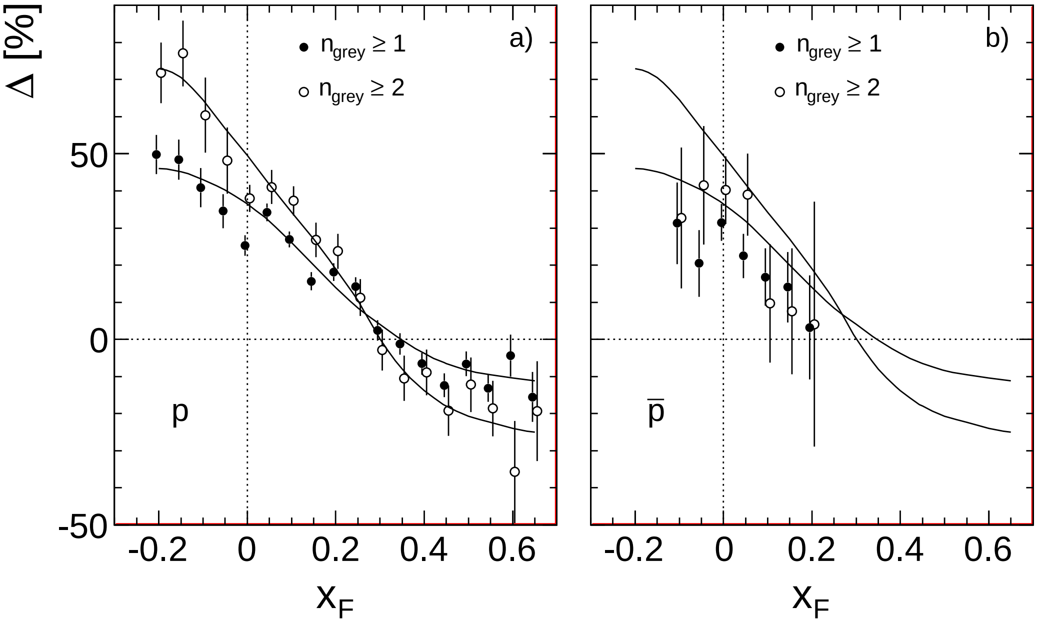

Figure 58: Relative difference Δ in % between n_{grey} selected and minimum bias samples as a function of x_F for a) proton and b) anti-protons. The lines are shown to guide the eye. The lines in panel b) repeat those from panel a)

The interplay between baryon number transfer from the projectile hemisphere and pile-up of baryons from the target fragmentation, including isospin effects, will be discussed in more detail in Sect.12 of this paper.

10.3 Neutron data

The detection of forward neutrons in the Ring Calorimeter of NA49 [10] has been introduced and described in detail in [3]. The neutron analysis concerning the separation of electromagnetic and hadronic deposits, the veto against charged particles, the calorimeter calibration and the energy resolution unfolding may be directly applied to the p+C interactions. The corrections for acceptance and for feed-down from weak decays are shown in Figs. 2 and 23, respectively. The empty target, trigger bias and re-interaction corrections are equal to the ones for protons [3]. The contributions from K^0_L decay and anti-neutron production are obtained from the charged kaon data which are available from NA49 [17] and from the isospin argumentation using the anti-proton data explained in [3].

The resulting neutron densities dn/dx_F are listed in Table 11 together with their ratio to the results from p+p collisions [3].

The p_T integrated neutron density distribution dn/dx_F as a function of x_F is presented in Fig. 59a. Of particular interest in this context is the ratio between neutron densities in p+C and p+p interactions in comparison to the same ratio for protons as shown in Fig. 59b.

Evidently protons and neutrons show within errors the same behaviour when passing from p+p to p+C collisions. The density ratio is equal to 1 at x_F = 0.3, increasing to 1.3 at

x_F	dn/dx_F	Δ	$(dn/dx_F)^{\mathrm{pC}}/(dn/dx_F)^{\mathrm{pp}}$	Δ
0.1	0.621	21.4	1.29	5.0
0.2	0.482	15.1	1.18	3.2
0.3	0.389	13.6	1.03	3.1
0.4	0.303	12.7	0.93	3.2
0.5	0.268	12.8	0.83	3.6
0.6	0.221	11.0	0.75	4.1
0.75	0.194	11.7	0.68	5.2
0.9	0.128	29.1	0.59	8.4

Table 11: p_T integrated neutron density distribution dn/dx_F as a function of x_F and the ratio of neutron densities in p+C and p+p interactions. The relative errors are given in %. They are governed by the systematic uncertainties quoted in Table 1

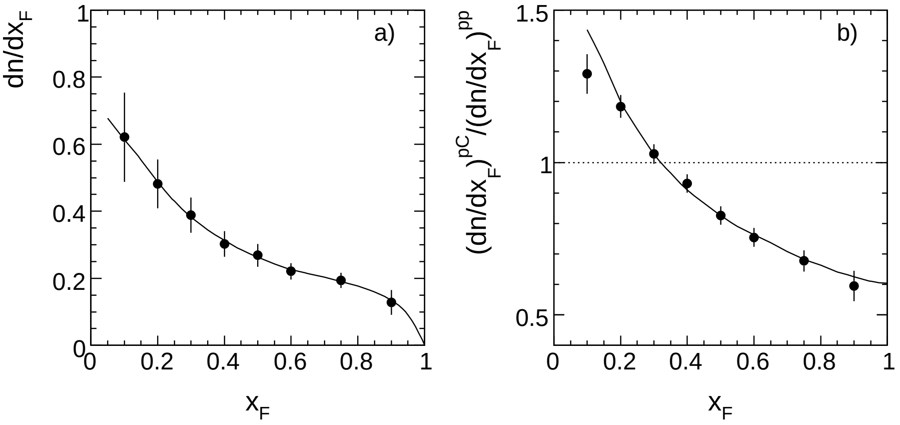

Figure 59: a) p_T integrated neutron density distribution dn/dx_F and b) neutron density ratio between p+C and p+p interactions as a function of x_F. The full line shows the corresponding density ratio for protons

x_F = 0.1 and decreasing to 0.6 at x_F towards +1. The latter value corresponds to the expected fraction of single projectile collisions in p+C interactions derived from the nuclear density distribution [5].

10.4 Comparison to other data

Two data sets are available for comparison with the NA49 integrated data in the SPS energy range. The first set from the ACCMOR collaboration [18] gives the density distribution dn/dx_F of protons for p+A collisions from Be to U nuclei at 120 GeV/c beam momentum. A second, very recent publication from the MIPP collaboration [19] provides neutron densities dn/dx_F for p+C interactions again at 120 GeV/c beam momentum at the FERMILAB Main Injector.

10.4.1 ACCMOR data [18]

The ACCMOR collaboration [18] measured proton densities dn/dx_F with a proton beam at 120 GeV/c momentum at the CERN SPS for five different nuclei (Be, Cu, Ag, W, U) in the x_F range from 0.07 to 0.6. These data may be interpolated from Be to C. This is demonstrated in Fig. 60 which gives the proton density as a function of mass number A for five x_F values from 0.1 to 0.6.

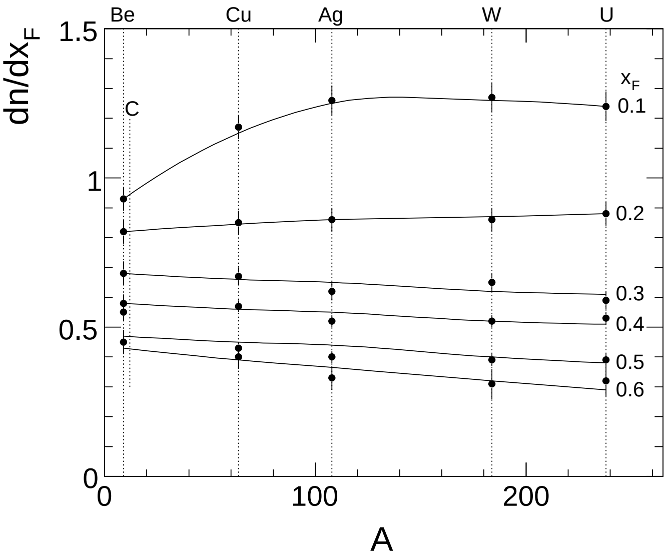

Figure 60: Proton density dn/dx_F as a function of mass number A for p+Be, p+Cu, p+Ag, p+W and p+U nuclei for different values of x_F. The lines describe the data interpolation used for the determination of the corresponding p+C cross sections

The data interpolation of dn/dx_F to p+C interactions is shown in Fig. 61 as a function of x_F in comparison to the NA49 results, Table 7 and Fig. 52 above.

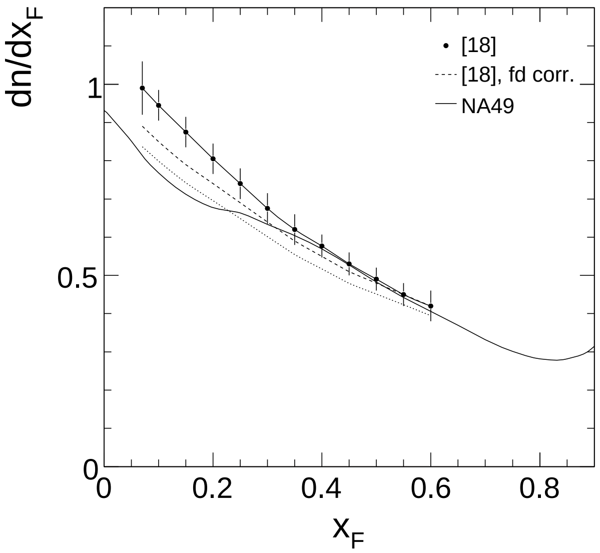

Figure 61: Proton density dn/dx_F as a function of x_F interpolated to p+C from the ACCMOR data. The full line through the ACCMOR results is drawn to guide the eye, the full line shows the NA49 result. The broken line gives the ACCMOR result after a tentative subtraction of proton feed-down from weak decays. The dotted line corresponds to the modification of the total inelastic cross section for p+Be collisions with 6%, see Fig. 62

The ACCMOR data show an upward deviation which increases from about 0 at x_F = 0.6 to about 20% at the lower data limit of x_F = 0.07. This deviation looks similar to the feed-down correction for protons from weak hyperon decays used for the NA49 data, Sect. 5.3, which reaches 15% at small x_F and decreases rapidly to 0 at $x_F \sim 0.7$. As such a correction is not mentioned in [18] and as the geometrical layout of the experiment is similar to the one of NA49 as far as the position of the tracking elements is concerned ($\sim$ 3 m distance between target and first tracking station) it has been tentatively assumed that the on-vertex reconstruction efficiency of decay products might be similar in both experiments. Subtracting the feed-down correction from NA49 results in the broken line in Fig. 52. This line is about 8% above the NA49 results for $x_F < 0.4$. At this point a look at the total inelastic cross sections as a function of A from different references [18, 20], Fig. 62, shows that the cross section for p+Be given in [18] falls low by about 6% compared to the interpolation of other available data [20]. A corresponding correction of the cross section is shown as dotted line in Fig. 61

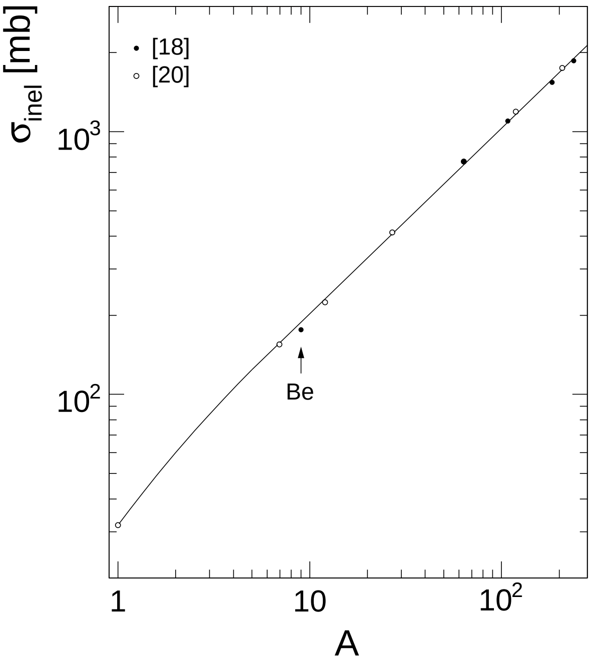

Figure 62: Data summary of measured total inelastic cross sections of p+A interactions as a function of A, [18, 20]

In conclusion it may be stated that the ACCMOR results are compatible with the NA49 results within the quoted systematic uncertainties.

10.4.2 MIPP data [19]

Very recently new data on neutron densities dn/dx_F have become available from the MIPP collaboration at the FERMILAB Main Injector for p+p and p+A interactions [19]. The MIPP neutron densities dn/dx_F for p+C interactions at 120 GeV/c beam momentum are compared to the NA49 results in Fig. 63a, the densities for p+p collisions at 84 GeV/c beam momentum in Fig. 63b.

Important deviations are visible between the two experiments both for p+C and p+p collisions. This is quantified in Fig. 64 where the ratio

$$R_n = (dn/dx_F)^{\text{MIPP}}/(dn/dx_F)^{\text{NA49}} \tag{11}$$

between the two respective interpolations is shown as a function of x_F.

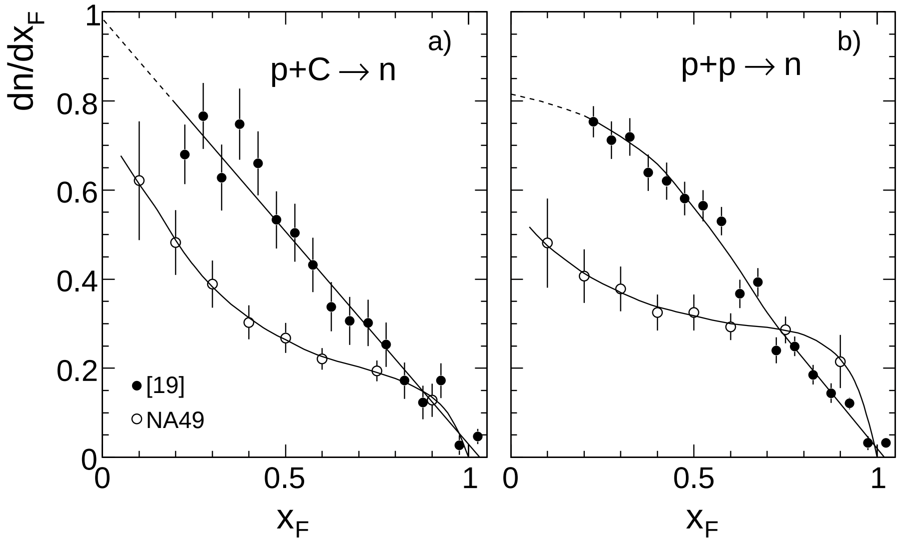

Figure 63: Comparison of MIPP neutron densities dn/dx_F to the NA49 results as a function of x_F, a) for p+C interactions and b) for p+p interactions. Interpolations through the respective data points are shown as full lines

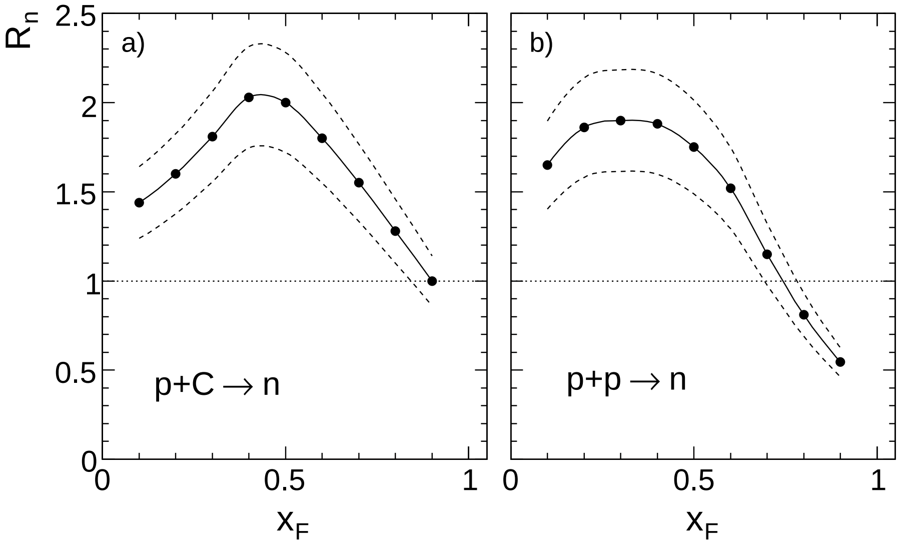

Figure 64: Density ratio $R_n = (dn/dx_F)^{\mathrm{MIPP}}/(dn/dx_F)^{\mathrm{NA49}}$ as a function of x_F, a) for p+C, b) for p+p interactions. The error bands shown are based on the statistical uncertainties of the data points

The density ratios show a remarkable similarity between p+C and p+p interactions, varying systematically from 1.4–1.6 at the lower x_F limit to a maximum of 1.9–2.0 at $x_F \sim 0.4$ and decreasing to 0.5–1.0 at the upper kinematic limit. The total neutron yields in the forward hemisphere obtained by an extrapolation of the measured densities towards $x_F = 0$ as shown in Fig. 63 deviate by about 60% for both reactions, with the integrated MIPP neutron yield resulting in 1 neutron per event for p+p collisions at 84 GeV/c beam momentum.

These large deviations pose a problem for baryon number conservation which may be verified for p+p interactions using published total yields for protons, neutrons, hyperons, pair produced protons and pair produced hyperons. The available data are plotted in Fig. 65 as a function of $\sqrt{s}$ from [21] at 12 and 24 GeV/c beam momentum, [22, 23] at 32 GeV/c beam momentum, [24, 25] at 69 GeV/c beam momentum and from NA49.

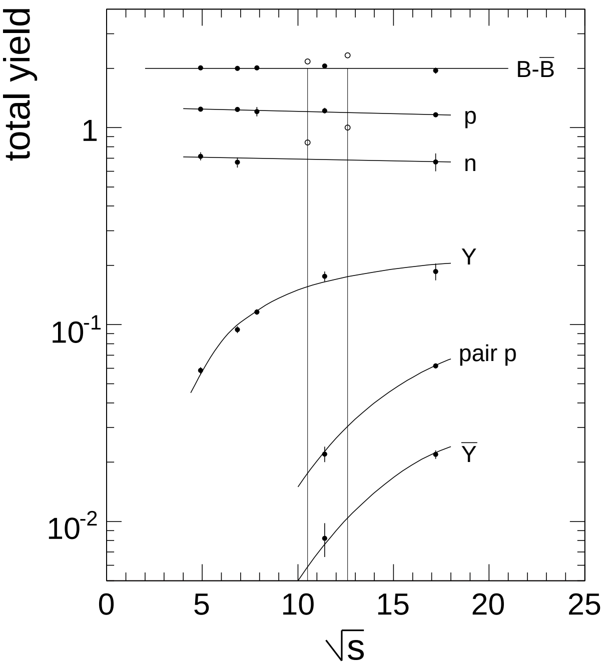

Figure 65: Total yields of protons, neutrons, hyperons, pair produced protons and anti-hyperons, [21–24], as well as the total number of net baryons (B-$\overline{\text{B}}$) as a function of $\sqrt{s}$ between 4.9 and 17.2 GeV. The integrated neutron yields from MIPP [19] at 58 and 84 GeV/c beam momentum are indicated as open circles

The large neutron yields published by MIPP are clearly out of proportion with respect to the available data and are incompatible with baryon number conservation.

11 Two component mechanism of baryon and baryon pair production

An important key to the understanding of hadronic interactions, in particular concerning the asymmetric p+A collisions, is provided by the fact that these may be separated into independent components connected to the fragmentation of the target and projectile systems, respectively. There are several experimental findings which prove this characteristics:

- the absence, at SPS energy, of charge and flavour exchange
- the absence of long-range two-particle correlations between the target and projectile hemispheres at $|x_F| > 0.2$
- the independence of the target fragmentation on the nature of the projectile particle (hadronic factorization)

There is however an overlap of target and projectile fragmentation in the central region at $|x_F| \lesssim 0.2$, where this x_F limit depends on the mass of the secondary particle considered and on the transverse momentum [5]. This has been experimentally verified by the measured forward-backward multiplicity correlations which extend – as they are governed by pion production – to $|x_F| \lesssim 0.1$. A detailed study of extent and shape of this overlap region has been performed for pions with the NA49 detector [5] using the isospin symmetry of the π^+/π^- ratio in π^++p and π^-+p interactions at the SPS. It has also been shown in [5] that the range and shape of the pionic overlap is equal for p+C and p+p collisions. In the following discussion the overlap from projectile to target hemisphere and vice versa will be called "feed-over".

Concerning baryons the situation is somewhat more complicated as a clear distinction between pair-produced baryons and "net" baryons has to be made. Here the "net" baryon yield is defined as the difference between the total yield of a given baryon species and the yield of pair-produced baryons of the same species. Whereas the sum of all net baryon yields is constrained by baryon number conservation, the production of baryon/anti-baryon pairs shows a strong $\sqrt{s}$ dependence. The yield rises sharply from threshold at about $\sqrt{s}$ = 6 GeV through the SPS energy range and flattens towards collider energies in a way characteristic of the production of heavy hadronic systems. The cross section is centred close to x_F = 0 , the central $\overline{\mathrm{p}}$/p ratio reaching about 23% at SPS energy in the minimum bias p+C interactions considered here, see Sect. 10. For ease of distinction, the pair produced baryons will be denoted in the following sections by:

$$\begin{aligned} \text{pair produced protons} &= \widetilde{\mathrm{p}} \\ \text{pair produced neutrons} &= \widetilde{\mathrm{n}} \end{aligned} \tag{12}$$

The situation is further complicated by the fact that baryon/anti-baryon pairs are not limited to the isospin 0 combination but form an isospin triplet. In the case of protons and neutrons this results in the dependence on the isospin-3 component shown in Table 12.

I_3	-1	0	1
baryon pairs	$\overline{\mathrm{p}}\,\widetilde{\mathrm{n}}$	$\overline{\mathrm{p}}\,\widetilde{\mathrm{p}}$ $\overline{\mathrm{n}}\,\widetilde{\mathrm{n}}$	$\overline{\mathrm{n}}\,\widetilde{\mathrm{p}}$

Table 12: Isospin structure of baryon pair production

This phenomenology has been studied by NA49 using the comparison of p+p and n+p interactions. Here it was shown that the anti-proton yield increases (by a factor of about 1.6) when exchanging the I = +1/2 against an I = -1/2 projectile [12], thereby enhancing the I_3 = -1 with respect to the I_3 = +1 combination.

Both the baryon pair and the net baryon feed-over will be studied in the following sections. In fact the extent and the shape of the corresponding overlap functions will be determined in a strictly model-independent way essentially based on measured quantities and isospin invariance. In a first part, the symmetric p+p interactions will be exploited. In a second part it will be shown that the same overlap functions apply to p+C collisions.

11.1 Two component mechanism in p+p interactions

A large sample of 4.8 million inelastic events is available from NA49 [1–3] with both proton/anti-proton and neutron identification in the final state. This allows for the selection of sub-samples of events with defined net baryon number either in the projectile or in the target hemisphere by tagging baryons at sufficiently large $|x_F|$. Sufficiently large means in this context x_F values where the yield of pair produced baryons is low enough to ensure negligible background. For protons this condition is fulfilled for $|x_F| > 0.35$ where the $\overline{\mathrm{p}}$/p ratio is less than 0.5% [3]. The following ranges of x_F have been used for net proton and neutron selection:

$$
\begin{aligned}
&\text{Projectile hemisphere:} && \text{protons} && 0.35 < x_F < 0.5 && (13)\\
& && \text{neutrons} && 0.5 < x_F < 0.7 && (14)\\
&\text{Target hemisphere:} && \text{protons} && -0.75 < x_F < -0.6 && (15)
\end{aligned}
$$

These ranges are given by the constraints of acceptance and proton identification via dE/dx, see Sect. 4, and by the limited energy resolution of the hadron calorimetry for neutrons. In the following the measured baryonic double and single differential densities obtained with net baryon constraint,

$$
\begin{aligned}
\rho^c(x_F, p_T) &= \frac{dn}{dx_F dp_T} \\
\rho^c_{\text{int}}(x_F) &= \frac{dn}{dx_F} \quad ,
\end{aligned}
\tag{16}
$$

will be described by their ratio to the corresponding inclusive yields,

$$
\begin{aligned}
&\rho^i(x_F, p_T) \\
&\rho^i_{\text{int}}(x_F)
\end{aligned}
\tag{17}
$$

by

$$
\begin{aligned}
R^c(x_F, p_T) &= \frac{\rho^c(x_F, p_T)}{\rho^i(x_F, p_T)} \\
R^c_{\text{int}}(x_F) &= \frac{\rho^c_{\text{int}}(x_F)}{\rho^i_{\text{int}}(x_F)}
\end{aligned}
\tag{18}
$$

The double differential cross sections are obtained, due to limited statistics, in the range 0.1 $< p_T <$ 0.7 GeV/c, and the resulting ratios are averaged over this p_T range resulting in the ratios:

$$
R^c_{\text{av}}(x_F) = \langle R^c(x_F, p_T) \rangle \quad . \tag{19}
$$

In a first sub-section the production of anti-protons in these samples will be studied, as the determination of the net proton yields has to rely on the estimation of the cross sections of pair-produced protons.

11.1.1 Anti-protons with final-state net baryon constraint

The ratios $R^c_{\text{av}}(x_F)$ and $R^c_{\text{int}}(x_F)$ for anti-protons are presented in Fig. 66 for forward (13) and backward (15) proton selection.

For both net proton selections, a distinct correlation between the anti-proton yields and the presence of a tagged proton in the respective hemisphere is evident. The yield ratios reach values of 1.55 in the far backward and forward directions, respectively. The excess over 1 is halved at x_F = 0 and ratio goes to 1 in the respective opposite x_F regions. It has been verified that this correlation is not induced by asymmetries in the azimuthal acceptance of the detector. It is therefore due to an isospin effect as expected from the iso-triplet nature of baryon pair

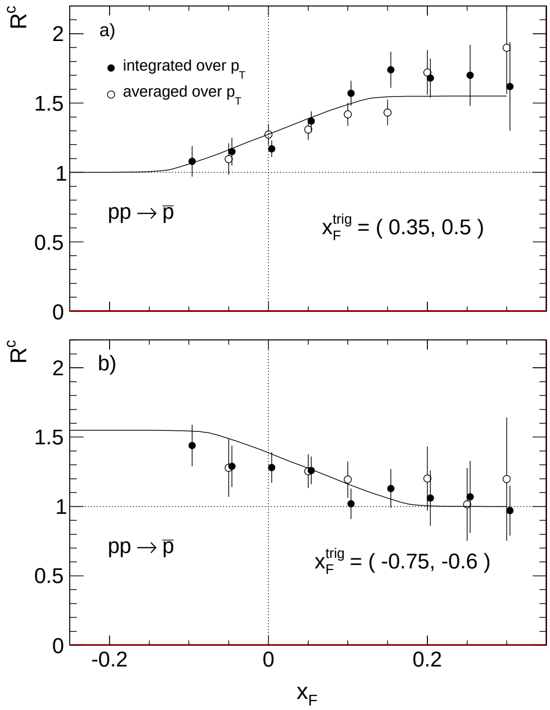

Figure 66: Yield ratios $R^c_{\mathrm{int}}(x_F)$ and $R^c_{\mathrm{av}}(x_F)$ for anti-protons for a) forward and b) backward proton selection, as a function of x_F. The full lines are forward-backward mirror symmetric and represent and estimate of the $\overline{\mathrm{p}}$ overlap function

production, Table 12. Indeed the presence of a net proton will unbalance the isospin structure present in the inclusive event sample towards the I_3 = -1 component of the corresponding heavy mesonic state and thereby enhance the $\overline{\mathrm{p}}\,\widetilde{\mathrm{n}}$ yield in the selected hemisphere. From this argument follows a strict prediction for the tagging with net neutrons: in this case the I_3 = +1 component, hence the $\overline{\mathrm{n}}\,\widetilde{\mathrm{p}}$ combination, should be favoured, and the anti-proton yield should be reduced accordingly with respect to the inclusive sample. This is indeed the case as shown in Fig. 67 for forward neutron tagging, see (14).

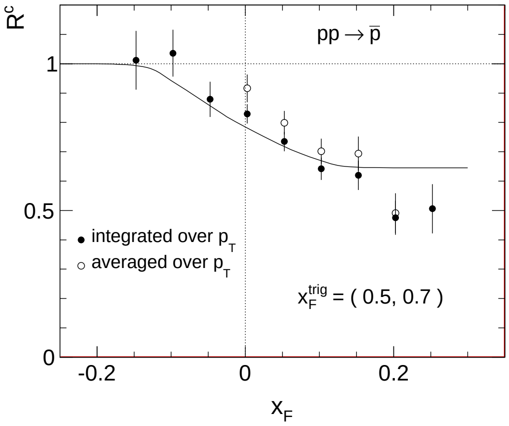

Figure 67: Yield ratios $R^c_{\mathrm{int}}(x_F)$ and $R^c_{\mathrm{av}}(x_F)$ for anti-protons for forward neutron tagging, as a function of x_F. The full line represents the prediction using the extracted overlap function, Fig. 66

This finding has two interesting consequences: it allows for the first time the establishment of the range and shape of the anti-proton overlap function in a completely model-independent way. Secondly it has direct consequences for the possible production mechanism of baryon pairs in hadronic interactions.

The overlap function is related to the full lines presented in Figs. 66 and 67. As the yield ratios are stable at $|x_F| > 0.2$ this means that the $\overline{\mathrm{p}}$ feed-over is limited to $|x_F| < 0.2$. In the application to measured inclusive $\overline{\mathrm{p}}$ yields the function should be normalized for projectile fragmentation to unity in the region $x_F > 0.2$, should reach 0.5 at $x_F = 0$ and vanish at $x_F < -0.2$, with an x_F symmetric shape for target fragmentation. The resulting functions are presented in Fig. 68.

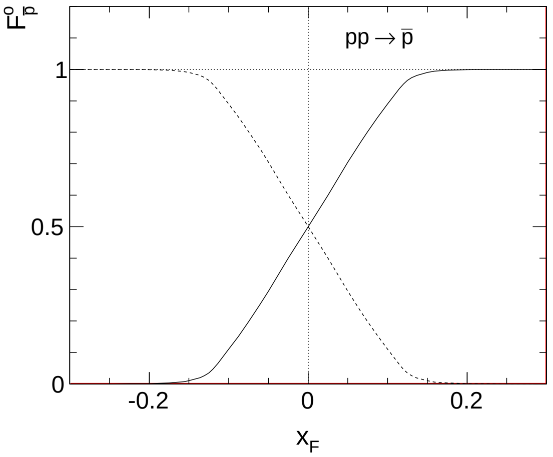

Figure 68: Anti-proton overlap function $F^o_{\overline{\mathrm{p}}}$ as a function of x_F for projectile fragmentation (full line) and target fragmentation (broken line)

Concerning the production mechanism of baryon pairs, the strong isospin correlation both with the final state net baryons and with the hadronic projectile in the initial state speaks against the central production from the quark-gluon sea, as for instance gluon fusion. Concerning current hadronization models using string fragmentation, the ad-hoc introduction of diquark systems in the colliding baryons is necessary in order to describe the net baryon production. In addition quark/anti-quark and diquark/anti-diquark pickup processes have to be introduced for baryon pair production, in close resemblance to the description of hadronization in e^++e^- annihilation, with a multitude of adjustable parameters and doubtful predictive power, see Sect. 11.4.

On the other hand the presence of heavy, high spin mesonic states in the early stage of hadronization of the highly excited baryonic systems in the p+p interaction presents a natural explanation for the observed correlations. In fact most observed heavy meson resonances have a $\overline{\mathrm{p}}\,\widetilde{\mathrm{p}}$ decay branching fraction, or have been discovered in the inverse $\overline{\mathrm{p}}$+p annihilation process. It is interesting to note that baryon pair production, via the high effective mass involved, probes a rather primordial phase of hadronization as compared to the lighter final state hadrons. This again favours the observed strong isospin correlations. In this context it should be recalled that a high mass mesonic origin of baryon pairs was indeed proposed as early as 35 years ago by Bourquin and Gaillard [26] in order to describe the observed inclusive yields.

11.1.2 Pair-produced protons

Following the isospin structure of baryon pair production, see Table 12, anti-protons ($\overline{\mathrm{p}}$) and pair produced protons ($\widetilde{\mathrm{p}}$) are coupled in their yields by isospin symmetry with the I_3

component of either the projectile or the trigger net baryon in the respective hemisphere. This is shown schematically in Fig. 69 where the $\overline{\text{p}}$ and $\tilde{\text{p}}$ yields are presented with respect to the inclusive anti-proton level in p+p interactions.

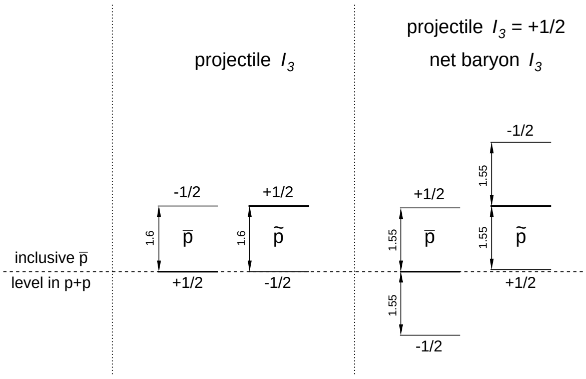

Figure 69: Yield levels of anti-protons ($\overline{\text{p}}$) and pair produced protons ($\tilde{\text{p}}$) with respect to the inclusive $\overline{\text{p}}$ yield in p+p interactions, left: for a change of projectile I_3 from +1/2 to -1/2, right: for a change of the trigger net baryon I_3 from +1/2 to -1/2

Evidently the definition of ”net” protons, which needs the knowledge of pair-produced proton yields, is linked to the measured $\overline{\text{p}}$ yields in a non-trivial fashion. As far as the overlap function between the forward and backward hemispheres is concerned, it is of course the same for $\overline{\text{p}}$ and $\tilde{\text{p}}$ and has to be referred to the yield levels indicated in Fig. 69.

11.1.3 Net proton feed-over

With the above clarification of the yields of pair produced baryons, the inclusive net proton yield may now be defined as:

$$\rho_{\text{p}}^{\text{net}}(x_F, p_T) = \rho_{\text{p}}^{\text{incl}}(x_F, p_T) - \rho_{\tilde{\text{p}}}^{\text{incl}}(x_F, p_T) \tag{20}$$

As $\rho_{\tilde{\text{p}}}^{\text{incl}}$ is 1.6 times higher than $\rho_{\overline{\text{p}}}^{\text{incl}}$, Fig. 69, this means a substantial decrease of the central net proton density with respect to the simple subtraction of the $\overline{\text{p}}$ yield. The consequence of this for the evolution of $\rho_{\text{p}}^{\text{net}}$ with $\sqrt{s}$ has been demonstrated in [12] where it has been shown that the central net invariant proton cross section approaches zero in the ISR energy range.

The net proton feed-over and the corresponding overlap function may be determined, as for the anti-proton case Sect. 11.1.1 above, by fixing a net proton in the projectile or target hemisphere following the selection criteria, (13) and (15) above, respectively. This ensures the absence of net protons in the corresponding hemisphere and results in the constrained net proton density:

$$\rho_{\text{p}}^{c,\text{net}}(x_F, p_T) = \rho_{\text{p}}^{c}(x_F, p_T) - \rho_{\tilde{\text{p}}}^{c}(x_F, p_T) \tag{21}$$

These density distributions may be normalized by dividing by the inclusive yield, (20), resulting in the ratio

$$R_{\text{p}}^{c,\text{net}}(x_F, p_T) = \frac{\rho_{\text{p}}^{c,\text{net}}(x_F, p_T)}{\rho_{\text{p}}^{\text{net}}(x_F, p_T)} \tag{22}$$

In a first instance, it can be shown that $R_{\mathrm{p}}^{c,\mathrm{net}}(x_F, p_T)$ is independent on p_T in the range $0.1 < p_T < 0.7$ GeV/c, see Fig. 70

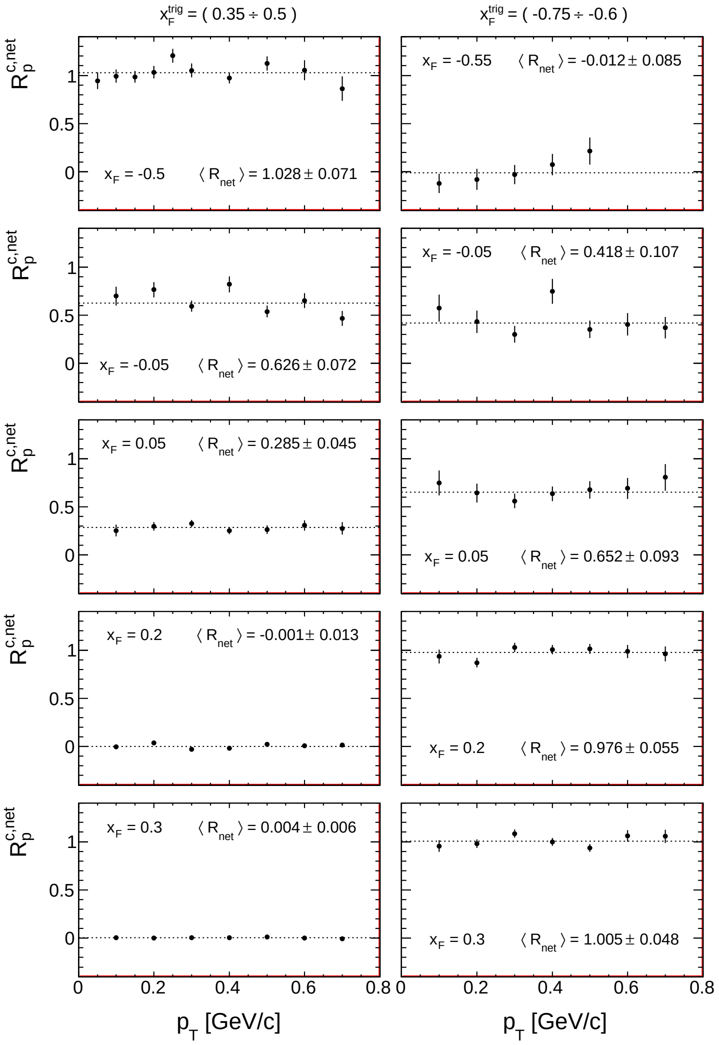

Figure 70: Ratio $R_{\mathrm{p}}^{c,\mathrm{net}}(x_F, p_T)$ between constrained and inclusive net proton densities as a function of p_T at different values of x_F for net proton trigger in the projectile hemisphere (left side panels) and for trigger in the target hemisphere (right side panels)

The x_F dependence for the p_T integrated ratio $R_{\mathrm{p}}^{c,\mathrm{net}}(x_F)$ and the p_T averaged ratio $\langle R_{\mathrm{p}}^{c,\mathrm{net}}(x_F, p_T)\rangle$ are shown in Fig. 71.

Evidently the overlap functions for protons and anti-protons turn out to be the same within the statistical errors of the measurements.

11.2 Proton and anti-proton feed-over in p+C interactions

The study presented above for p+p collisions may be repeated for p+C interactions, albeit with reduced statistical significance due to the smaller available data sample. The density ratio for anti-protons, $R_{\overline{\mathrm{p}}}^{c}(x_F)$ with forward proton tagging is presented in Fig. 72 where the full line represents the feed-over function measured in p+p interactions, see Fig. 66.

Evidently the measurement reproduces the shape and extent of the $\overline{\mathrm{p}}$ overlap in p+p collisions.

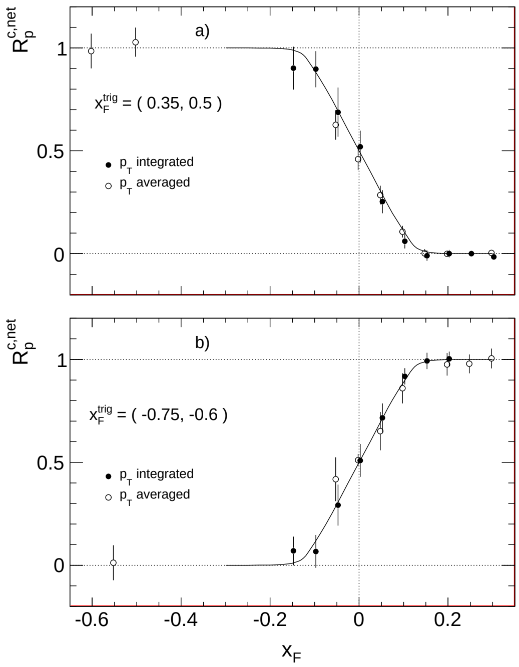

Figure 71: p_T integrated and p_T averaged constrained net proton density ratios $R_{\mathrm{p}}^{c,\mathrm{net}}$ as a function of x_F, a) for forward net proton selection and b) for backward net proton selection. The full lines shown represent the overlap functions presented in Fig. 68

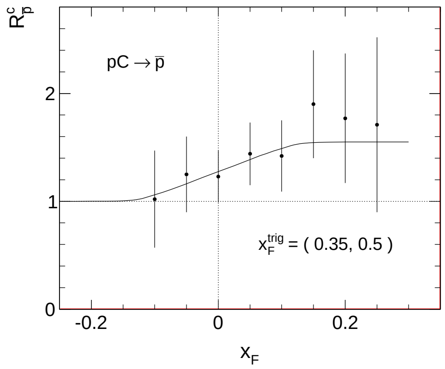

Figure 72: Anti-proton density ratio $R_{\bar{\mathrm{p}}}^{c}(x_F)$ as a function of x_F. The full line represents the feed-over in p+p events

Net proton tagging in the backward hemisphere is not possible for p+A interactions as protons from intranuclear cascading (”grey” protons) which prevail in this area dilute the correlation.

For the net proton density $\rho_{\mathrm{p}}^{c,\mathrm{net}}(x_F)$ with tagging in the projectile hemisphere, a result which might look surprising at first view is found as shown in Fig. 73.

Indeed the constrained net proton density reproduces the one found in p+p interactions down to x_F = -0.2. This reveals an additional internal correlation effect generally present in minimum bias p+A interactions. By selecting a rather forward proton, see (13), single collisions corresponding to peripheral interactions are enhanced. In fact 60% of the minimum bias p+C events correspond to single interactions of the projectile proton with nuclear participants [5]. The situation is clarified by Fig. 74 which presents the inclusive proton yield $dn/dx_F(x_F)$ in

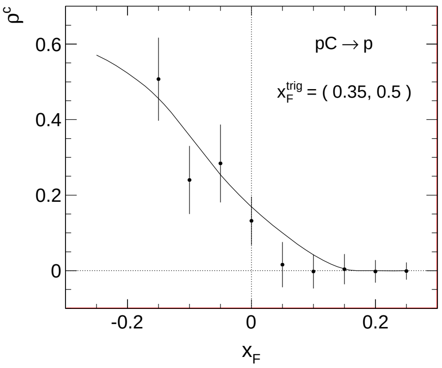

Figure 73: Net proton density in p+C collisions with forward net proton constraint as a function of x_F. The full line corresponds to the net density in p+p interactions

p+C collisions (full line), $0.6 \times dn/dx_F(x_F)$ from p+p (broken line), and their difference (dotted line). It is evident that the bulk of protons in the tagging region (hatched area) comes from single collisions, with the fraction of multiple collisions in addition biased against very inelastic interactions which would favour low-x_F protons by enhanced baryon number transfer. It may however be stated that also for p+C interactions with forward proton tagging the constrained net proton density dies out at $x_F > 0.2$.

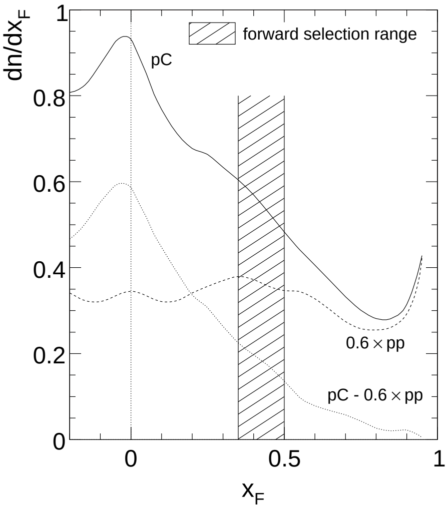

Figure 74: The inclusive proton yield $dn/dx_F(x_F)$ in p+C collisions (full line), $0.6 \times dn/dx_F(x_F)$ from p+p (broken line), and their difference (dotted line). The inclusive proton yield $dn/dx_F(x_F)$ in p+p collisions is shown as well with full line. The hatched area represent the tagging region

11.3 A remark concerning resonance decay

The model-independent extraction of the baryonic feed-over and the experimental determination of the corresponding overlap functions, as described in the preceding sections, may be extended to resonance decay. As in fact most if not all final state baryons stem from resonance decay it is of interest to investigate the consequences of the hadronic two-component mechanism observed for the final state baryons also for the parent generation of resonances.

This will be demonstrated below using as examples the well measured Δ^{++} resonance for the proton and a mesonic resonance approximated by measured tensor meson characteristics for the anti-proton feed-over.

11.3.1 Protons from $\boldsymbol{\Delta}^{++}$ *decay*

The p_T integrated density distribution $dn/dx_F(x_F)$ of the Δ^{++}(1232) resonance has been rather precisely measured by a number of experiments in the SPS and ISR energy ranges as shown by two examples [27, 28] in Fig. 75a. The integration of the interpolated full line yields a total inclusive cross section of 7 mb. The corresponding decay proton distribution from $\Delta^{++} \rightarrow \text{p} + \pi^+$ (100% branching fraction) is presented in Fig. 75b together with the measured total inclusive proton yield as measured by NA49 [3], multiplied by the factor 0.27.

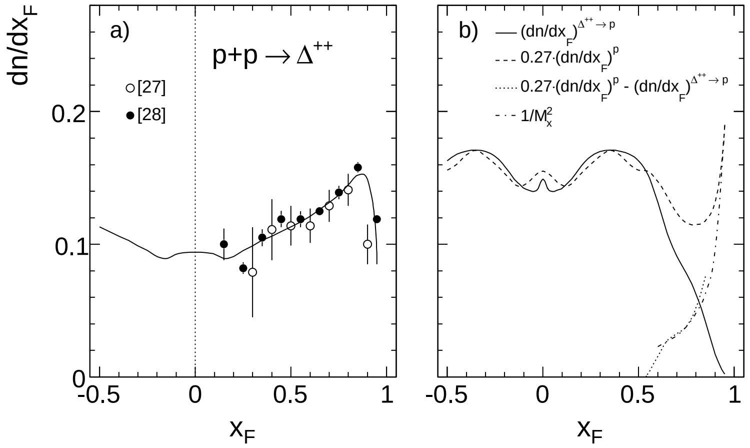

Figure 75: p_T integrated density distributions dn/dx_F as a function of x_F a) for Δ^{++}(1232), b) for the decay protons from $\Delta^{++} \rightarrow \text{p} + \pi^+$ (full lines). The broken line in panel b gives the total inclusive proton yield multiplied by a factor 0.27, the dotted line the difference between the two distributions. Also indicated in panel b is the $1/M_x^2$ distribution (see text) as dash-dotted line

This plot demonstrates several important features:

- the shape of the decay proton distribution from Δ^{++} follows, for $|x_F| < 0.6$, very closely (to within about 5%) the total inclusive proton distribution re-normalized by a factor 0.27. This means that 27% of all protons in this x_F range stem from Δ^{++} decay alone.
- the difference between the decay and inclusive distributions at $|x_F| > 0$ is well described by a $1/M_x^2$ form typical of single diffraction with $M_x^2 \sim s(1 - x_F)$, dash-dotted line in panel b).
- Taking account of the other Δ states Δ^+(1232) and Δ^0(1232) with branching fractions of 66% and 33% into protons, respectively, this means that more than 40% of all non-diffractive protons cascade down from Δ resonances
- the shape difference between the dn/dx_F distributions of the mother resonance and the daughter protons exemplifies the very effective baryon number transfer towards the central x_F region in resonance decay even for low-Q resonances like the Δ.

A number of further comments are due in this context. The absence of charge and flavour exchange in inelastic p+p interactions at SPS energy implies that the observed Δ resonances are not directly produced at least in the primordial phase of target and projectile excitation. They rather turn up as decay products of N* resonances. This fact has been experimentally proven in a number of high precision studies of single and double diffraction into p$\pi^+\pi^-$ states from PS to ISR energies [29–32]. In these final states which cover an $|x_F|$ range from 1 to about 0.6 [32], the initial I, I_3 state is 1/2, +1/2. Although the sub-channels pπ^+ and pπ^- show clear Δ(1232) signals, those are completely contained in the decay mass spectra of a series of N* resonances (N*(1440), N*(1520), N*(1680)). In the more central area of hadronization, this clear isospin signature will become diluted and contain 1/2, -1/2 states, see also the isospin correlations discussed above. Nevertheless the production and decay of N* resonances without intermediate Δ states will provide another important source of final state nucleons.

The two-component mechanism of hadronization should therefore also be considered for baryon resonances with the constraint to reproduce the measured overlap function for final state protons. This is fulfilled for Δ^{++} by the separation of the production cross section into a target and a projectile component as indicated in Fig. 76a. The corresponding x_F distributions for the decay protons are given in Fig. 76b.

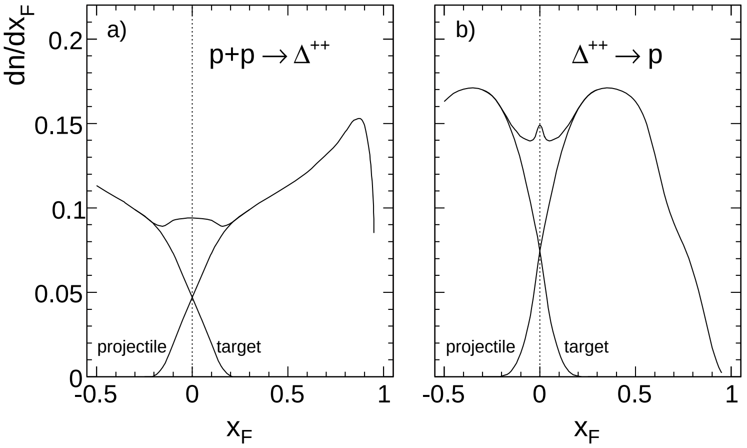

Figure 76: Density distributions dn/dx_F as a function of x_F a) for the target and projectile components of Δ^{++} and b) for the decay protons

This choice results in the ratios $R = (dn/dx_F)_{\text{proj}}/(dn/dx_F)^{\text{incl}}$ between projectile component and inclusive distribution shown in Fig. 77.

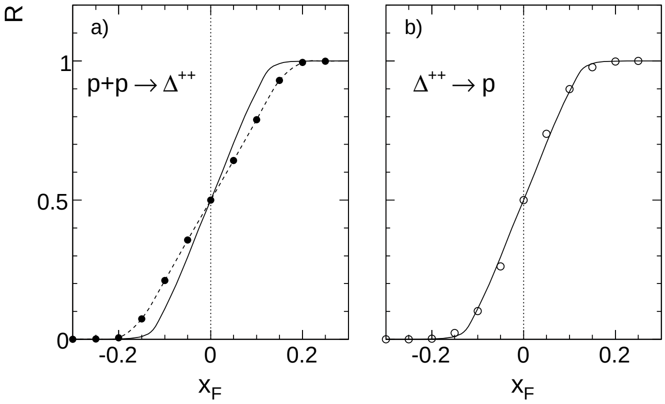

Figure 77: Density ratios $R = (dn/dx_F)_{\text{proj}}/(dn/dx_F)^{\text{incl}}$ a) for Δ^{++}, full circles and hatched line, and b) for the decay protons from Δ^{++} decay, open circles, as a function of x_F. The measured overlap function, see Fig. 71, is indicated as the full line in both panels

Evidently the measured proton feed-over is precisely reproduced, Fig. 77b, if the overlap function of the mother resonance is chosen slightly wider in x_F, Fig. 77a, indicating a certain mass dependence in the x_F scale. In this context the dependence on decay particle mass exhibited by the much reduced feed-over for the decay pions from Δ^{++}, as elaborated in [5], should be recalled here.

11.3.2 Anti-protons from heavy meson decay

A complementary approach may be used for the production of anti-protons from heavy mesonic states [26]. In fact a sizeable number of states above the $p\overline{p}$ mass threshold at 1.88 GeV/c^2 have been observed [33] both in hadronic interactions and in the inverse $p\overline{p}$ annihilation into final state hadrons. If due to the large width and density of these states their direct experimental detection in mass spectra is difficult, the application of Partial Wave Analysis permits their localization and determination of quantum numbers. In the following a hypothetical state at 2.5 GeV mass with a Breit-Wigner width of 0.25 GeV and a two-body decay into $p\overline{p}$ is used in order to study the corresponding daughter x_F distributions and overlap functions. An invariant x_F distribution consistent with the one for vector and tensor mesons published by Suzuki et al. [34] yields the inclusive density distribution dn/dx_F for the decay anti-protons shown in Fig. 78.

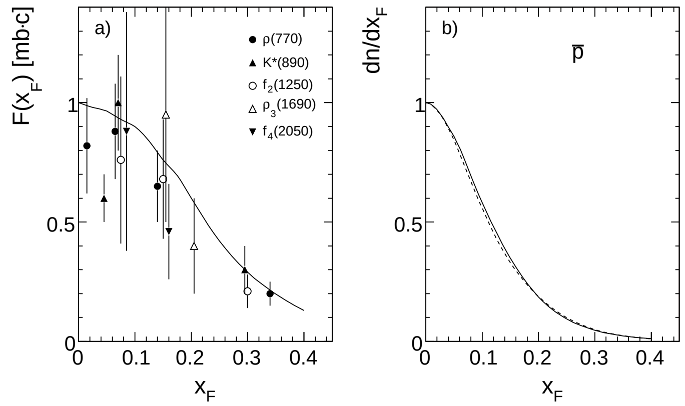

Figure 78: a) Invariant x_F distribution $F(x_F)$ of a mesonic state with 2.5 GeV mass (full line) compared to various vector and tensor mesons [34] normalized to unity at x_F = 0, b) resulting inclusive density distribution dn/dx_F for the decay anti-protons (full line) compared to the measured yields in p+p interactions [3] (broken line)

Evidently this choice reproduces perfectly the measured inclusive anti-proton yields measured by NA49 [3]. Imposing the target-projectile decomposition for the yield distribution of the heavy meson as shown in Fig. 79a, the overlap function for the decay baryons reproduces closely the measured feed-over for anti-protons, Fig. 79b.

As far as the normalization of the resulting inclusive yields is concerned, it may be stated that – compared to the $\overline{p}$ cross section of 1.2 mb [3] – the measurement of [34] indicates 1.6 mb for the $f_4(2050)$ state alone, and the mass dependence of the tensor meson production given in [35] an $f_4(2050)$ cross section in excess of 5 mb at ISR energy. There are, however, almost no measurements of the branching fraction into baryon pairs, and if so, they vary by large factors, for the $f_4(2050)$ for instance from 50% [36] to 0.2% [37]. The amount to which anti-protons cascade from heavy meson decay has therefore to stay an open question.

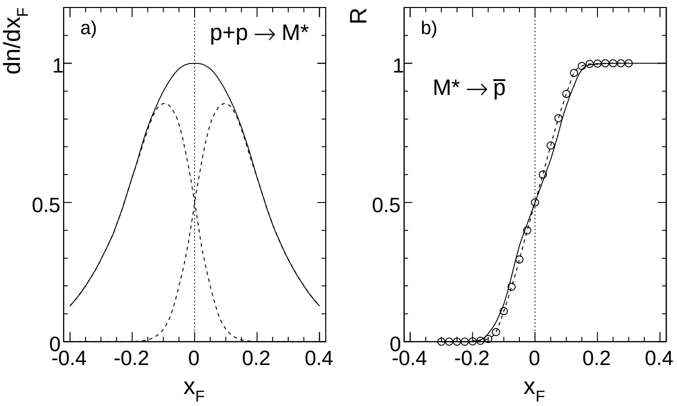

Figure 79: a) Density distribution dn/dx_F for the heavy mesonic state (full line) normalized to 1 at x_F = 0 decomposed into a target and a projectile component (broken lines), b) the corresponding overlap function $R(x_F)$ (full line) superimposed with the measurement (open circles and broken line)

11.4 Comparison to a microscopic simulation code

In the preceding NA49 publications concerning p+p and p+C interactions [1–5] a strictly model-independent approach to the interpretation of these extensive and precise data sets has been followed. Comparison to the multitude of existing microscopic simulation codes has therefore been avoided in clear appreciation of the fact that the actual understanding (or, better, lack of understanding) of the theoretical foundations of the soft sector of QCD calls for improved experimental information rather than ad hoc parametrizations. Given the detailed data concerning baryons both on the inclusive level and on the level of baryonic correlations contained in [3] and in the above discussion, it might however be useful to confront the obtained results with one specific microscopic simulation in order to obtain some idea of the precision and predictive power reached in such approaches.

The relatively recent code named JAM [38] has been chosen for this comparison. This code is supposed to describe hadronization in elementary and nuclear interactions over the complete cms energy range from 1 GeV up to collider energies. It uses, in the SPS energy range, soft string excitation following the HIJING approach which in turn relies on the string fragmentation mechanism developed in the PYTHIA/LUND environment.

11.4.1 Inclusive baryon and anti-baryon density distributions dn/dx_F

The measured proton and neutron density distributions dn/dx_F in p+p interactions are confronted in Fig. 80 with the predictions from JAM.

Large systematic deviations between prediction and data are visible at low x_F (-40%), at medium $x_F \sim$ 0.25 (+50%) and at high x_F (-30%) for the protons. Systematic deviations of similar or bigger size are also seen for the HSD and UrQMD codes [39].

The neutron yields are evidently obtained from the proton densities by a constant multiplicative factor of 0.69 with the exception of the large x_F region where a diffractive component with a $1/M_x^2$ behaviour, see Sect. 11.3.1, is added to the protons. The deviations are +60% at medium x_F and more than -100% at large x_F for the neutrons. A look at the density distributions for n+p interactions, Fig. 81, shows only approximate isospin symmetry which would impose that neutrons from proton fragmentation should be equal to protons from neutrons in the

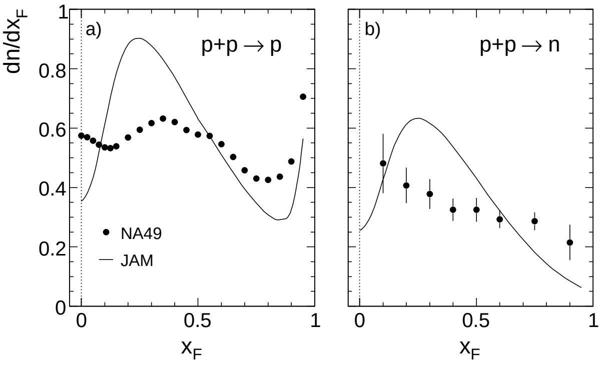

Figure 80: Density distributions dn/dx_F as functions of x_F a) for protons and b) for neutrons (full circles) in p+p collisions compared to the prediction from JAM (full lines)

x_F regions beyond the target-projectile overlap. The same should of course be true for neutrons from neutron beam and protons from proton beam.

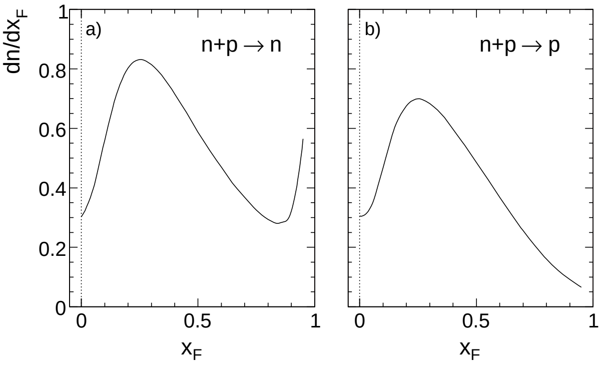

Figure 81: Density distributions dn/dx_F as functions of x_F a) for neutrons and b) for protons in n+p collisions from JAM

The anti-baryon densities shown in Fig. 82 show an interesting pattern, the anti-proton and anti-neutron yields being identical for both projectile-target combinations.

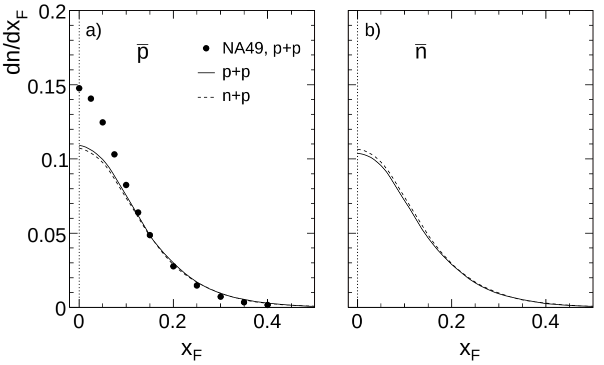

Figure 82: a) anti-proton and b) anti-neutron distributions dn/dx_F as functions of x_F from p+p and n+p interactions. The anti-proton distribution measured by NA49 is shown in panel a) with full circles

This means that only the I_3 = 0 combinations p$\overline{\text{p}}$ and n$\overline{\text{n}}$ are allowed which are produced with equal yields. The comparison with the measured anti-proton density in p+p collisions shows a sizeable underestimation of the yield by 35% at x_F = 0 and an equally large overestimation at $x_F \sim$ 0.3. Invoking the isospin effect measured in n+p interactions [12] this difference will increase to 50% in this reaction.

11.4.2 Baryonic correlations

If it might be a straightforward possibility to remedy the observed discrepancies between the prediction and the inclusive data by modifying some of the many parameters involved in the simulation codes, the correlation data will probe the "physics" input on a deeper level. This applies especially to the measured isospin effects.

A first comparison concerns the net proton density correlated with a trigger baryon in the projectile hemisphere resulting in the overlap function $R_{\text{p}}^{c,\text{net}}$, (22), as shown in Fig. 83 for the two trigger x_F bins defined in Sect. 11.1, Eqs. 13 and 14.

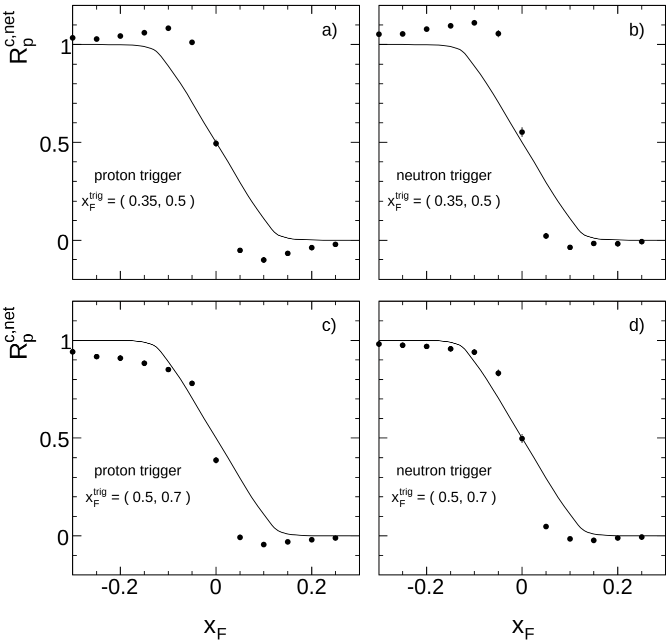

Figure 83: Net proton overlap function $R_{\text{p}}^{\text{c,net}}(x_F)$ as a function of x_F for a) proton trigger at x_F = 0.35 to 0.5, b) neutron trigger at x_F = 0.35 to 0.5, c) proton trigger at x_F = 0.5 to 0.7 and d) neutron trigger at x_F = 0.5 to 0.7. The full lines represent the measured function, Sect. 11.2, the points come from the JAM simulation code

The microscopic simulation results in a feed-over behaviour which only reaches to about ±0.06 in x_F. This is considerably sharper than the measured behaviour (full lines in Fig. 83) and corresponds to the pionic feed-over extracted in [5]. In addition there is an asymmetric long range tail that extends up to and beyond $|x_F| \sim$ 0.3 and is different both for proton and neutron trigger and for the two trigger x_F bins in contrast to the data.

The anti-proton feed-over behaviour characterized by the ratio $R_{\overline{\text{p}}}^{\text{c}}(x_F)$ of correlated to inclusive densities, Eq 18, is presented in Fig. 84 again for the two available trigger x_F bins and for proton and neutron trigger.

A rather complicated pattern concerning the simulation emerges. Evidently the symmetric isospin effect observed experimentally between proton and neutron triggers is not re-

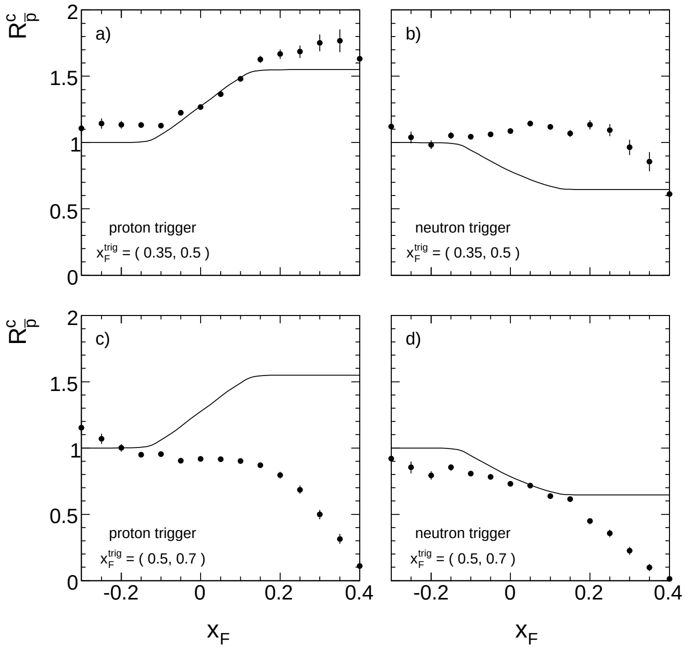

Figure 84: Anti-proton density ratio $R^c_{\overline{\mathrm{p}}}(x_F)$ as a function of x_F for a) proton trigger at x_F = 0.35 to 0.5, b) neutron trigger at x_F = 0.35 to 0.5, c) proton trigger at x_F = 0.5 to 0.7 and d) neutron trigger at x_F = 0.5 to 0.7. The full lines represent the measured function, Sect. 11.1.1, the points come from the JAM simulation code

produced although there is a general reduction of the density ratio in the trigger hemisphere with neutron triggers. As only isospin singlet baryon pairs are generated, see Sect. 11.4.1, any isospin effect is not really expected. The strong suppression of the density ratio in the high-x_F trigger bin already starting at $x_F \sim 0.2$ indicates an effect of energy-momentum conservation in the baryon pair simulation which is probably the result of the details of string fragmentation.

In conclusion the microscopic simulation results in major deviations from the data both on the level of the inclusive and of the correlated yields. The absence of a proper treatment of isospin effects both concerning the I_3 component of the projectile and of the final state baryons is flagrant. This puts into doubt the application of this approach to p+A and especially A+A interactions where the neutron component is preponderant.

12 Hadronization in p+C collisions: anti-protons

The two-component hadronization mechanism studied experimentally in the preceding section allows, in conjunction with the precision data on anti-proton production in p+p interactions published by NA49 [3], the confrontation of the measured $\overline{\mathrm{p}}$ yields in p+C collisions with a straight-forward prediction based on elementary reactions. This is simplified in the case of anti-protons by the fact that there is, in contrast to proton and pion production, no contribution from nuclear cascading (see Sect. 9 above). In consequence the superposition of target and projectile fragmentation should suffice to completely describe the observed cross sections. In a first step it may be assumed that the projectile contribution corresponds exactly to the one in p+p interactions. For the target contribution the same basic assumption may be made with two important additional constraints taking account, firstly, of the multiple intranuclear collisions of the projectile, and secondly, of the isospin factor involved in the fragmentation of the neutrons contained in the nucleus.

The mean number of projectile collisions $\langle\nu\rangle$ in minimum bias p+C collisions has been investigated in [5] using three different methods:

- a Monte Carlo simulation using the measured nuclear density profile as input with the result $\langle\nu\rangle$ = 1.6
- the measured p+C inelastic cross section which gives, via the relation

$$\langle\nu\rangle = \frac{A \cdot \sigma(pp)}{\sigma(pA)} \tag{23}$$

  an estimation of $\langle\nu\rangle$ under the assumption that the intranuclear inelastic interaction cross section stays constant for all subsequent projectile collisions, resulting in $\langle\nu\rangle$ = 1.68
- the measured increase of pion yields in the backward hemisphere using the fact that the contribution from intranuclear cascading as well as the one from projectile fragmentation die out at $x_F \sim$ -0.1, yielding $\langle\nu\rangle$ = 1.6.

The isospin factor for $\overline{\mathrm{p}}$ production from the isoscalar C nucleus may be calculated, using the measured increase of $\overline{\mathrm{p}}$ yields in n+p collisions $g^n_{\overline{\mathrm{p}}}$ [12] as

$$g^C_{\overline{\mathrm{p}}} = 0.5(1 + g^n_{\overline{\mathrm{p}}}) = 1.3, \tag{24}$$

with $g^n_{\overline{\mathrm{p}}}$ = 1.6. The combined overall factor to be applied to the target component is 1.6×1.3 = 2.08.

12.1 p_T integrated density $\mathbf{dn/dx_F(x_F)}$

The evolution of the p_T integrated anti-proton density $dn/dx_F(x_F)$ from the elementary p+p to the p+C interactions using the superposition of target and projectile components discussed above is presented in Fig. 85.

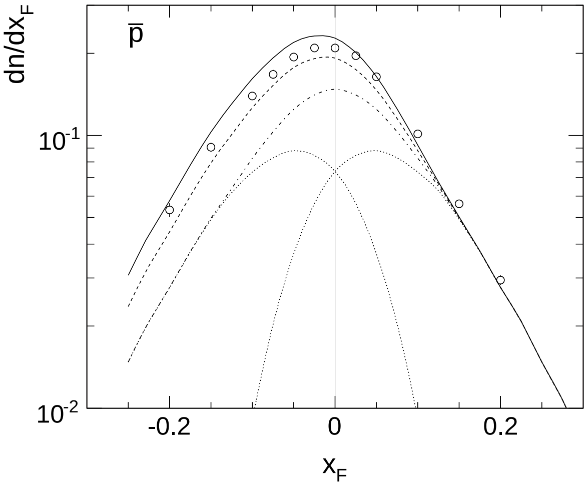

Figure 85: Measured p_T integrated anti-proton density $dn/dx_F(x_F)$ in p+C interactions (open circles) confronted with the superposition of target and projectile components in p+p collisions (dotted lines) and total yield (dash-dotted line), with multiplication factors $\langle\nu\rangle$ = 1.6 and 1 for target and projectile, respectively, broken line, and with the additional isospin factor 1.3 for the target component (full line)

This most straight-forward superposition picture evidently reproduces the measured $\overline{\mathrm{p}}$ densities quite closely, overestimating them by about 10% in the target area and underestimating them by the same amount in the projectile region. This can be remedied by decreasing the target multiplication factor by 12% from 2.08 to 1.84 and by increasing the projectile contribution by 10% resulting in a reasonable fit of the experimental data compatible with their statistical errors as shown in Fig. 86.

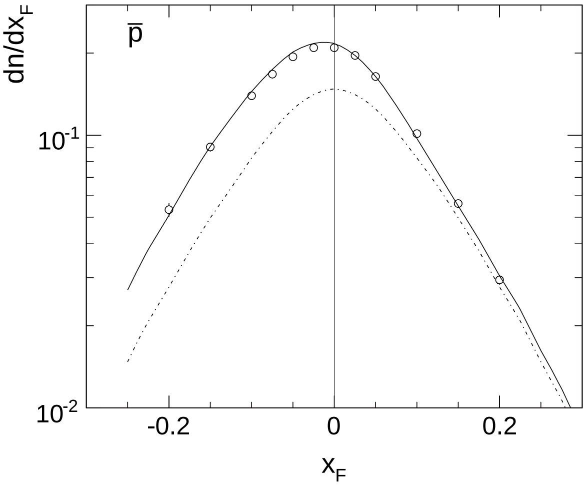

Figure 86: Measured p_T integrated anti-proton density $dn/dx_F(x_F)$ in p+C interactions compared with a target-projectile superposition scheme with factors 1.84 and 1.1, respectively, for the target and projectile components. The yield from p+p is shown with dash-dotted line

The increase of the p̄ yield by 10% in the projectile hemisphere with respect to the direct estimation from p+p collisions is a first interesting consequence of this study. It is equal to the increase of the pion yields deduced in [5].

The reduction of the target contribution by about 12% with respect to the simple superposition of elementary hadronization processes as characterized by the mean number of collisions $\langle\nu\rangle$ and isospin symmetry, is a second important result. The magnitude of this reduction being relatively small it is nevertheless on the limit allowed by the experimental determination both of $\langle\nu\rangle$ [5] and of the isospin effect on anti-proton production from neutrons [12].

Regarding the excitation mechanism of colliding hadrons by the exchange of gluons or gluonic (charge and flavour-less) objects, the observed effects are however to be expected. The projectile interacts in its multiple collisions subsequently with "fresh" nucleons which did not undergo previous exchanges. Hence its effective excitation level will increase with $\langle\nu\rangle$. The projectile on the other hand suffers in each collision a loss of its gluonic component such that less excitation energy with the target nucleons can be exchanged in subsequent interactions. In this sense the nucleus may be regarded as a gluon filter, the description of this phenomenology by the term of "energy loss" giving only a very general and somewhat misleading impression.

The anti-proton yields regarded here are especially sensitive to this notion as at SPS energy the s-dependence of the production cross section is still rather steep with about 10% per GeV in $\sqrt{s}$ [26]. This is in contrast to the production of mesons, with 5% per GeV for mean kaons [2] and only 3% per GeV for mean pions [40]. In this sense the study of pion yields in the target hemisphere approaches a precise measure of $\langle\nu\rangle$ [5] whereas the observed anti-proton cross section indicates an effective loss in $\sqrt{s}$ of about 1 GeV in target fragmentation for p+C collisions. Evidently the extension of this study to heavier nuclei is of considerable interest in this respect. The data on p+Pb collisions with controlled centrality available from NA49 will illuminate this point, as is already visible in the preliminary results shown in [41].

12.2 Double differential invariant densities $\mathbf{f(x_F, p_T)/\sigma_{inel}}$

Further details of the two-component hadronization mechanism detailed above become visible if comparing the double differential invariant densities to the optimized prediction from target and projectile fragmentation obtained from the p_T integrated yields, see Fig. 86. This is shown in Fig. 87 where the invariant cross sections $f(x_F, p_T)$ per inelastic event (open circles) are presented together with the predicted densities (full line).

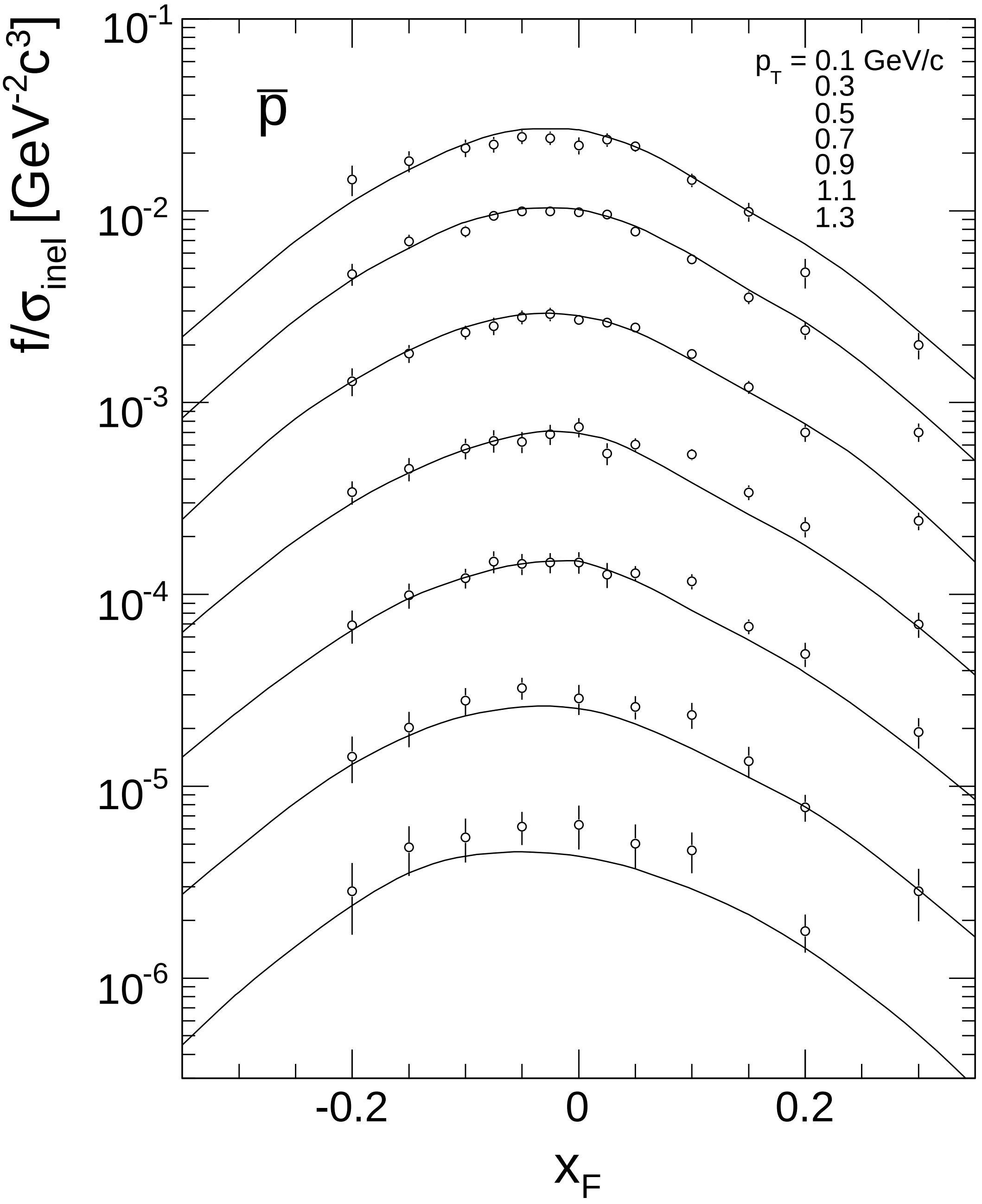

Figure 87: Double differential invariant anti-proton densities per inelastic event (open circles) compared to the prediction from the two component fragmentation mechanism (full lines) as a function of x_F, for different values of p_T between 0.1 and 1.3 GeV/c. The distributions for different p_T values are successively scaled down by 2 for better separation

Three main features may be extracted from these plots:

- the target component reproduces, within the experimental errors, the densities predicted from elementary interactions for $p_T < 1$ GeV/c.
- the projectile component reveals a definite p_T dependence. The measurements fall below the prediction for $p_T \lesssim$ 0.5 GeV/c and increase smoothly above the prediction above this value.
- in the range of $p_T > 1$ GeV/c the excess of the projectile component starts to extend well into the target hemisphere down to $x_F \sim$ -0.2.

This behaviour is detailed in Fig. 88 which presents the ratio R between measurement and prediction for the p_T values shown in Fig. 87.

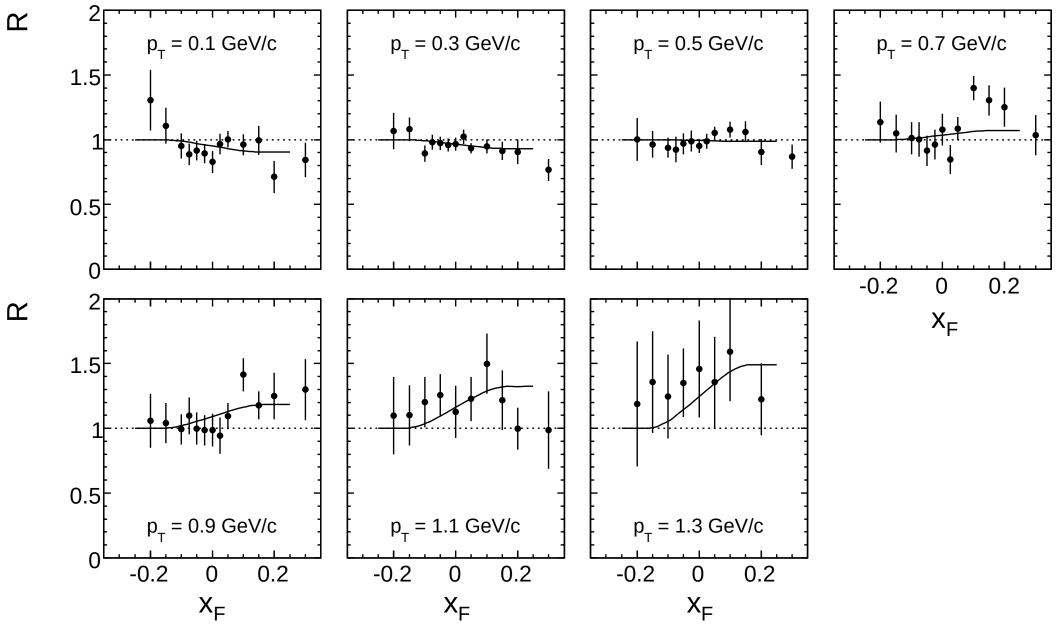

Figure 88: Ratio R between measured and predicted anti-proton densities for different p_T values between 0.1 and 1.3 GeV/c as a function of x_F. The full lines represent the parametrization $R = (1 - F^o_{\overline{\mathrm{p}}}) + R^{\mathrm{proj}} F^o_{\overline{\mathrm{p}}}$

The same ratio is plotted against p_T for different values of x_F in Fig. 89.

It should be stressed here that these experimental results are in strong support of the independent target-projectile fragmentation in p+C interactions. The modification of the p_T distribution of the projectile component which superimposes itself to the 10% increase in total yield, indicates that the Cronin effect, whose onset is visible here, is limited to the projectile hadronization. The increase of yields at higher p_T which extends well into the target hemisphere might be due to an extension of the feed-over range with p_T (see also [5] for pions), although the limited statistics does not allow for quantitative statements. The increase of R in the projectile hemisphere may be parametrized as

$$R^{\mathrm{proj}} = 0.9 + 0.35 p_T^2 \tag{25}$$

Its modification in the transition to the target hemisphere is then predicted by the projectile overlap function $F^o_{\overline{\mathrm{p}}}$ (Fig. 68) resulting in the full lines indicated in Figs. 88 and 89.

Further information is contained in the detailed comparison of the average p_T values to p+p interactions given in Fig. 90.

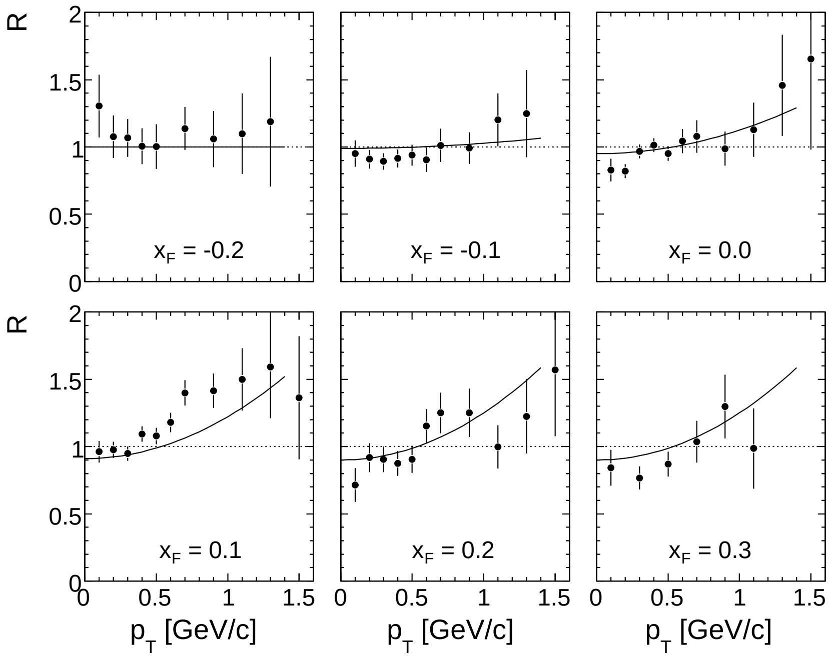

Figure 89: Ratio R between measured and predicted anti-proton densities for different x_F values as a function of p_T. The full lines represent the parametrization $R = (1 - F^o_{\overline{\mathrm{p}}}) + R^{\mathrm{proj}} F^o_{\overline{\mathrm{p}}}$

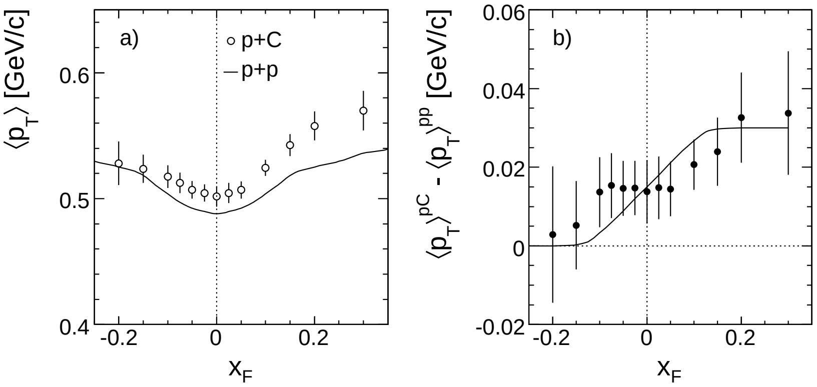

Figure 90: a) comparison of average p_T between p+p collisions (full line) and p+C interactions (data points), b) difference in $\langle p_T \rangle$ between p+C and p+p interactions. The full line in panel b) represent the anti-proton overlap function $F^o_{\overline{\mathrm{p}}}$ from Sect. 11.1.1

The convergence of the difference in $\langle p_T \rangle$ towards zero in the backward hemisphere, Fig. 90b, and its description by the overlap function $F^o_{\overline{\mathrm{p}}}$, Fig. 68, is to be regarded as yet another manifestation of the two-component mechanism of hadronization as discussed in Sect. 11.

13 Proton production in p+C collisions: p$_T$ integrated yields

As in the preceding section on anti-protons, proton production will be first discussed using the p_T integrated yields dn/dx_F in order to clearly visualize and separate the three basic contributions to the overall proton cross section. After establishing the net proton density by subtracting the yield of pair produced protons, the fragmentation of the hit target nucleons, the projectile fragmentation and the contribution from intra-nuclear cascading will be treated in turn.

13.1 Pair produced protons and net proton density

It has been shown above that the iso-triplet nature of baryon pair production imposes a detailed follow-up of isospin effects all through the hadronization process. This means of course that the yield of anti-protons is in general not identical to the yield of pair-produced protons. It is therefore not sufficient to subtract the anti-proton density as established in the preceding section from the proton yield in order to obtain the net proton density. In the case of the asymmetric p+C interaction, the equality of anti-proton and pair-produced proton yields is only valid for the target part of the overall cross section due to isoscalar carbon nucleus, invoking isospin symmetry. For the projectile component on the other hand this does not apply. In the absence of precision data for anti-proton production in n+C collisions it may be assumed that the same enhancement of pair-produced protons over anti-protons as in p+p interactions applies where a factor of 1.6 has been established [12]. This modifies the superposition scheme for anti-protons described in Sect. 12 by increasing the projectile contribution from 1.1 to 1.76 with respect to the input p+p densities. The resulting p_T integrated density distribution for pair produced protons (hereafter denoted as $\widetilde{\mathrm{p}}$) is shown in Fig. 91.

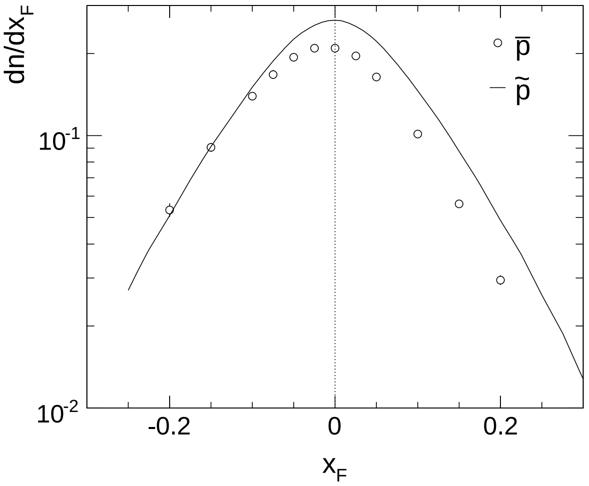

Figure 91: Density distribution $dn/dx_F(x_F)$ for pair produced protons ($\widetilde{\mathrm{p}}$) as a function of x_F (full line). The data points are the measured anti-proton densities

This distribution is in contrast to Fig. 80 almost symmetric and the comparison to the measured anti-proton densities demonstrates that this isospin effect is by no means negligible.

The corresponding net proton density distribution results from the subtraction of the pair produced protons from the total proton density distribution, Table 7 and Fig. 52. It is presented in Fig. 92 in the x_F range influenced by pair production, -0.4 $< x_F <$ +0.4.

The net proton density shows, in contrast to the total proton yield, a smooth behaviour around x_F = 0.

13.2 Target and projectile components in net proton production

The fragmentation of those nucleons in the carbon nucleus which are hit by the through-going projectile, here called the "target component", is a quantity which should be closely related to the proper superposition of net proton production in the elementary p+p and p+n

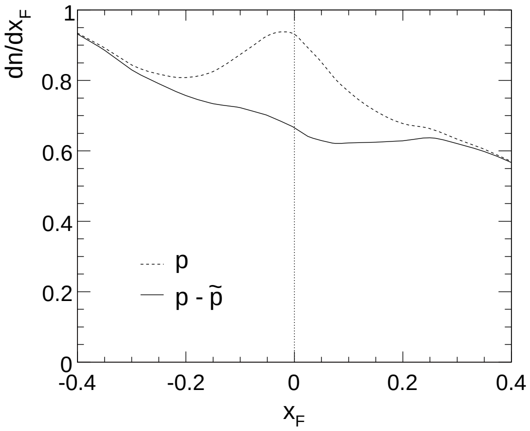

Figure 92: Density distribution $dn/dx_F(x_F)$ for protons (broken line) and for net protons (full line) as a function of x_F in the range -0.4 $<$ x_F $<$ +0.4

interactions, multiplied by the number of projectile interactions. Such a superposition has been shown to describe the target component of the anti-proton yields, Sect. 12, up to a loss of about 12% specific to multiple collisions and related to the strong s-dependence of baryon pair production. For baryons this loss should be negligible as the baryon density is to first order s-independent at SPS energy.

For the prediction of the target component, knowledge about the two basic contributions from

$$\mathrm{p+p} \rightarrow \widetilde{\mathrm{p}} \quad \text{and} \quad \mathrm{p+n} \rightarrow \widetilde{\mathrm{p}} \tag{26}$$

is needed. The latter process may be related, via isospin symmetry, to the reaction

$$\mathrm{p+p} \rightarrow \widetilde{\mathrm{n}} \tag{27}$$

which is measured by the NA49 experiment [3]. The resulting prediction for the isospin averaged net proton density from p+p collisions is described in the following section.

13.2.1 Isospin averaged net proton density from p+p collisions

The p_T integrated proton and neutron densities dn/dx_F as measured by the NA49 experiment are shown in Fig. 93 as dotted and broken lines. The corresponding net proton yield is obtained by subtracting 1.6 times the measured anti-proton yield. For the net neutron yield, the subtraction of the measured anti-proton yield is indicated by the isospin symmetry of baryon pair production. In the case of the isoscalar carbon nucleus, a simple average of the two distributions is to be performed as indicated by the full line in Fig. 93.

13.2.2 Predicted target component of net proton production

In order to obtain the predicted target component of net proton production in p+C interaction, the predicted yield from p+p collisions has to be multiplied by the number of projectile collisions $\langle\nu\rangle$ = 1.6 and by the target overlap function, Sect. 11.2. The resulting distribution is shown in Fig. 94 together with the total net proton yield, Sect. 13.1.

As a first result it may be seen that the target component nearly saturates the total yield at $x_F \sim$ -0.2.

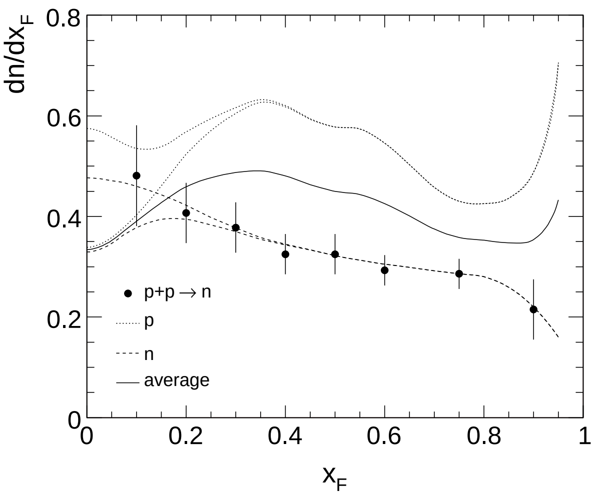

Figure 93: Total and net proton density $dn/dx_F(x_F)$, dotted lines, total and net neutron densities (broken lines) together with the measured neutron cross sections (data points from [3]) and the isospin averaged net proton density(full line), as a function of x_F

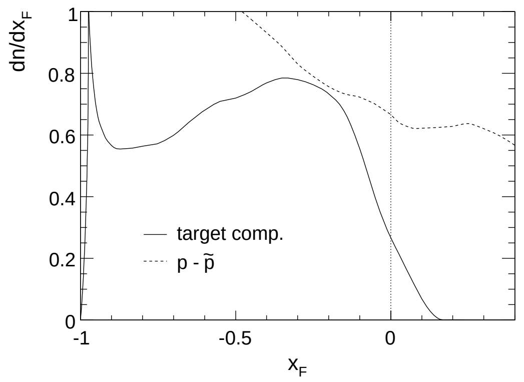

Figure 94: Total net proton density $dn/dx_F(x_F)$, broken line, and predicted target contribution (full line) as a function of x_F

13.3 The projectile component of net proton production

The subtraction of the predicted target component from the overall net proton density, Fig. 94, allows now for the extraction of the projectile component of the p+C interaction. This is demonstrated in Fig. 95 which shows the net projectile component (full line) in comparison with the net projectile component in p+p collisions (broken line, Sect. 11.2).

Several features of these distributions are noteworthy:

- this study allows for the first time the isolation of the net proton projectile component in p+A collisions over the full phase space
- in principle this net proton component is strongly constrained by baryon number conservation in comparison to p+p collisions, to the extent that the surface under the two distributions should be equal up to second order effects like a relative increase of neutron or hyperon production.
- in fact the integrated yields are 0.547 and 0.52 net protons per inelastic event for p+p and p+C interactions, respectively. In view of the multi-step methodology involved in extracting this experimental result, the agreement to within about 5% is certainly com-

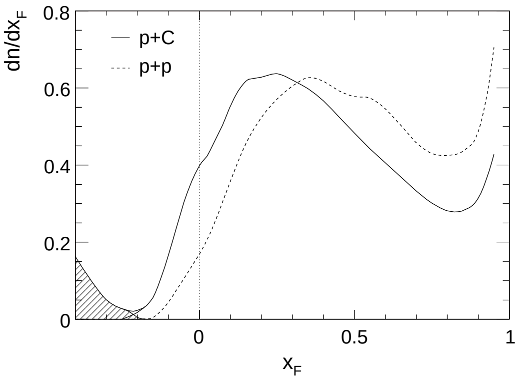

Figure 95: Net proton density $dn/dx_F(x_F)$ for the projectile component in p+C interactions (full line) and in p+p collisions (broken line) as a function of x_F. The shaded area indicates the onset of the contribution from the nuclear component in p+C interactions

patible with the systematic uncertainties.

- a relative increase of the net neutron yield, which is in principle not excluded in multiple hadronic interactions, is improbable as it has been shown, see Sect. 10.3, that the baryon number transfer is identical for neutrons and protons.
- a relative increase of hyperon production can as well only have limited influence as an increase of Λ and Σ production by 50% would only reduce the observed difference from 5% to 4%.
- the shapes of the two distributions are rather similar, with a downward shift of about 0.15 units in x_F in p+C except for the diffractive region which is governed by single projectile collisions
- at $x_F <$ -0.2 there is a steep increase of the target-subtracted density (shaded region in Fig. 95) which is due to the tail of protons from intra-nuclear cascading. This contribution will be discussed in detail below (Sect. 13.4). It is however to be noted that a clean separation of the projectile component from both the target and the nuclear cascading contributions is being achieved at SPS energy. At lower cms energies, the nuclear component will extend into higher x_F ranges, covering x_F = 0 at AGS energy, as it scales in p_{lab} rather than x_F.

It is interesting to extract the projectile overlap function from the ratio $R_{\text{p}}^{c,\text{net}}$, see (22), between the projectile component and the symmetrized total density. This is shown in Fig. 96 in comparison with the corresponding function in p+p collisions.

As a further important result of this study it may be stated that in multiple collisions the width of the proton feed-over from the projectile to the target hemisphere widens. In view of the discussion of resonance decay in Sect. 11.3 above, this would be compatible with an increase of the effective mass in the process of projectile excitation.

13.4 The nuclear component of net proton production

If the subtraction of the target component from the total net proton density distribution reveals the projectile component at $x_F >$ -0.2, it also should allow for the extraction of the nuclear component at $x_F \lesssim$ -0.2. Here the nuclear component is defined as the retarded proton density produced by the intra-nuclear cascading of nucleons following the momentum transfer from the projectile to the nucleus, as opposed to the prompt fragmentation of those nucleons which are hit by the projectile.

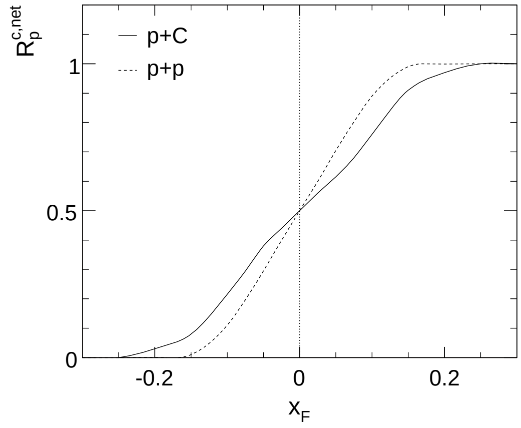

Figure 96: Projectile overlap function $R_{\mathrm{p}}^{c,\mathrm{net}}(x_F)$ as a function of x_F from p+C interactions (full line) compared to the same function from p+p interactions (broken line)

The situation is clarified in Fig. 97 which shows the total net proton density dn/dx_F for x_F $<$ -0.2 (full line) together with the target component discussed in the preceding section (broken line), Fig. 94.

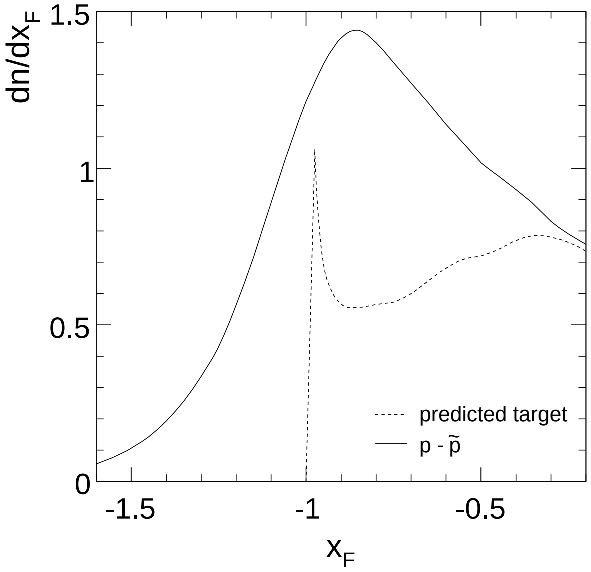

Figure 97: Net proton density dn/dx_F as a function of x_F in the range -1.6 $<$ x_F $<$ -0.2. Full line: total measured yield, broken line: predicted target component

The subtraction of the target component from the total yield, Fig. 98 (full line), results in a rather particular pattern.

This pattern features two distinct regions in x_F. For the region of ±0.2 units around x_F = -1, an abrupt bipolar instability arises from the presence of a diffractive peak in the predicted target component, whereas for the regions -1.6 $<$ x_F $<$ -1.2 and -0.8 $<$ x_F $<$ -0.2 a smooth x_F distribution results which is well fitted by a Gaussian of the form

$$\frac{dn}{dx_F} = 0.95 e^{-\frac{(x_F+0.92)^2}{2 \cdot 0.265^2}} \tag{28}$$

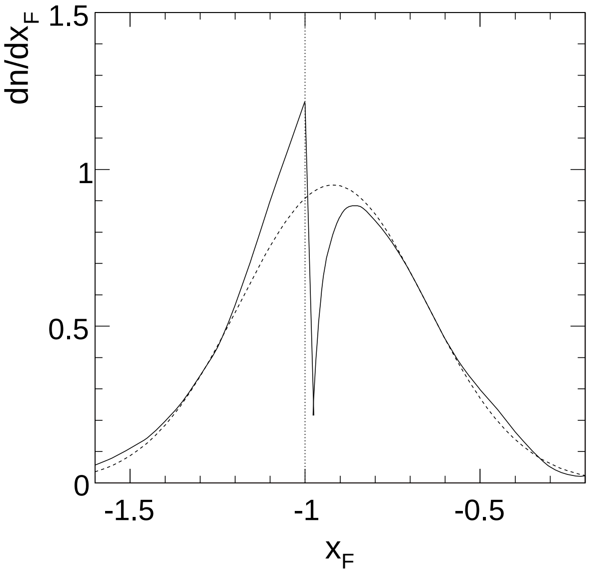

Figure 98: Net proton density dn/dx_F as a function of x_F in the region -1.6 $<$ x_F $<$ -0.2 resulting from the subtraction of the predicted target density from the total measured proton yield (full line) and a Gaussian fit to the difference in the two regions -1.6 $<$ x_F $<$ -1.2 and -0.8 $<$ x_F $<$ -0.2, broken line

centered at x_F = -0.92 with an rms of 0.265 as shown by the broken line in Fig. 98.

The diffractive component of the predicted target density should show up in any measurement of the total proton density in the region around x_F = -1 if the nuclear component would have as expected a smooth behaviour across this region. Assuming the Gaussian fit to describe this smooth behaviour one may tentatively subtract the Gaussian shape from the total proton density as shown in Fig. 99.

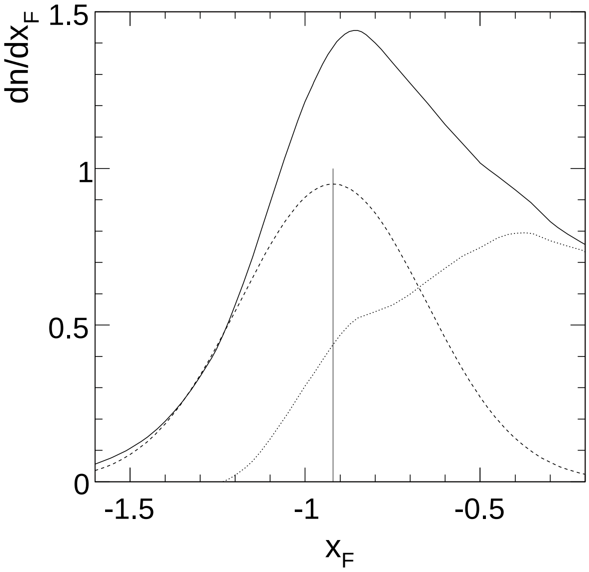

Figure 99: Net proton densities dn/dx_F in the region -1.6 $<$ x_F $<$ -0.2 as a function of x_F, full line total measured yield, broken line Gaussian fit to the target density in the regions -1.6 $<$ x_F $<$ -1.2 and -0.8 $<$ x_F $<$ -0.2, dotted line difference of the two distributions

This results in a modified target component (dotted line in Fig. 99) which reaches down to x_F values at $\sim$ -1.2 and goes smoothly through x_F = -1. The difference between the modified and predicted target component is bipolar around x_F = -1 and conserves, to first order, the total integrated density, as shown in Fig. 100.

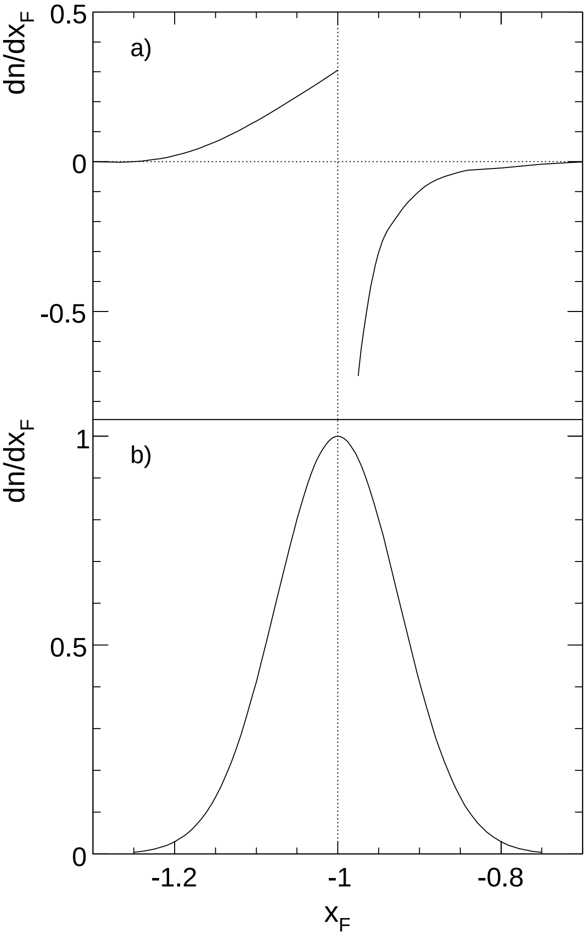

Figure 100: a) Difference between the modified target component (Fig. 97, broken line) and the predicted component obtained by subtraction of the Gaussian nuclear component (Fig. 99, dotted line). b) Gaussian longitudinal proton density distribution as obtained in quasi-elastic scattering of alpha-alpha collisions at $\sqrt{s}$ = 30 GeV/nucleon at the CERN ISR [45]

In this context the action of the Fermi motion of the hit nucleons on the momentum distribution of protons in the diffractive peak should be recalled. Fermi motion may be approximated by a Gaussian momentum distribution of about 75 MeV/c rms width in the nuclear rest system. This translates at SPS energy to an rms width of about 0.085 in x_F. Low momentum transfer processes like quasi-elastic scattering or diffraction convolute with this momentum distribution. This leads to a smearing of the peak structure characterized by a base width of ±2-3 times the Fermi rms around x_F = -1. This is quantified by the Gaussian x_F distribution with rms 0.085 in Fig. 100b which covers exactly the range of the observed deviation from the predicted diffractive peak. This convolution has been studied in quasi-elastic alpha-alpha scattering at the CERN ISR [45] where it was shown that low momentum transfer re-scattering processes have only small influence on the longitudinal width in contrast to a substantial broadening of the transverse momentum distribution, see Sect.14 below.

The extracted width of the nuclear component in longitudinal momentum with an rms of 0.265 units in x_F is much larger than the spread expected from Fermi motion. This feature is known from quite a number of experiments since some decades [6] but is shown here for the first time to be symmetric, however not around x_F = -1 but around x_F = -0.92. This substantial transfer of baryon number needs comment. One effective mechanism contributing to the transfer of nucleons in longitudinal momentum is certainly the production of pions in the intra-nuclear cascade. In the excitation of I = 3/2 states at pion threshold, the decay products are located at x_F = -0.85 and x_F = -0.15, respectively, for protons and pions, and for isobars at $x_F \sim$ -1. For isobar masses above threshold the x_F values of the decay baryons will shift further up.

The production of pions in the nuclear cascade has indeed been studied in the accompanying publication [6]. The backward pion yields have been separated into the two components of target fragmentation which may be predicted from elementary hadronic collisions, and of nuclear cascading, in close similarity to the argumentation carried out here for baryons. As a result the total number of pions in the nuclear component has been determined to 0.3 per inelastic event.

The Gaussian distribution of the nuclear component, Fig. 99, integrates to 0.6 protons per inelastic event, see Sect. 13.6 below. Isospin symmetry and the absence of charge exchange in the primary p+C interaction at SPS energy ask for an equal number of neutrons to be produced. This means that every fourth proton in the nuclear cascade produces a pion. In the decay of the isospin 3/2 isobars involved with pion production, the decay protons are transferred to x_F = -0.85 at pion threshold with the decay pions being centred at x_F = -0.15 for low lab momenta. Integrating over the pion transverse momentum distribution this center shifts down to about -0.2 [6] with a rather long tail towards lower x_F. The corresponding nucleons will be placed at x_F = -0.8 and above. The center of the nuclear component at x_F = -0.92 is therefore compatible with pion production in the nuclear cascade via isobar excitation near threshold and the subsequent decay into baryons and pions. The symmetry of the nuclear component would however ask for a bigger pion yield at about one pion for every second proton. Here de-excitation processes without pion emission like final state isobar-nucleon re-scattering could be involved to reduce the pion yield.

In conclusion of the preceding sections on p_T integrated proton distributions it may be stated that a three-component mechanism of convincing internal consistency has been established in a quantitative and precise way. These three components are defined by

- the fragmentation of the projectile which obeys baryon number conservation and shows a transfer in longitudinal momentum corresponding to 0.15 units in Feynman x_F.
- the prompt fragmentation of the nucleons hit by the projectile. This component has been predicted from elementary proton-nucleon interactions invoking isospin symmetry and the mean number of projectile collisions.
- the nuclear component which arises from intra-nuclear cascading and is partially accompanied by pion production.

At SPS energy the nuclear component extends up to x_F = -0.2. It is well separated from the projectile fragmentation which feeds over into the target hemisphere down to the same value of x_F = -0.2. The target fragmentation in turn reaches from x_F = +0.2 down to x_F = -1.2. The latter range is well beyond the kinematic limit of elementary fragmentation with a diffractive peak close to and above x_F = -1. This sharp diffractive structure is evidently diluted and smoothed by quasi-elastic re-scattering of its low-momentum nucleons in accordance with experimental results from other experiments.

13.5 A remark about s-dependence

If the SPS energy range is, as shown above, a well suited region for the separation of the three components contributing to the measured net baryon density, it is interesting to look at the expected evolution with $\sqrt{s}$.

13.5.1 *The nuclear component*

The study [6] of backward proton production in p+C interactions shows that only small changes in the momentum distributions are to be expected by increasing $\sqrt{s}$ to RHIC energy and beyond, or by decreasing it into the AGS energy region. Indeed one has to move down to $\sqrt{s}$ below about 3 GeV in order to see threshold effects drastically reducing the proton density. In terms of the range in x_F covered by the nuclear component, however, kinematics will extend the upper limit of $\sim$ -0.25 at SPS energy to higher values until x_F = 0 is reached at $\sqrt{s} \sim$ 4 GeV. This purely kinematic effect is presented in Fig. 101 where x_F is plotted as a function of 1/$\sqrt{s}$ for two values of p_{lab} and three values of p_T.

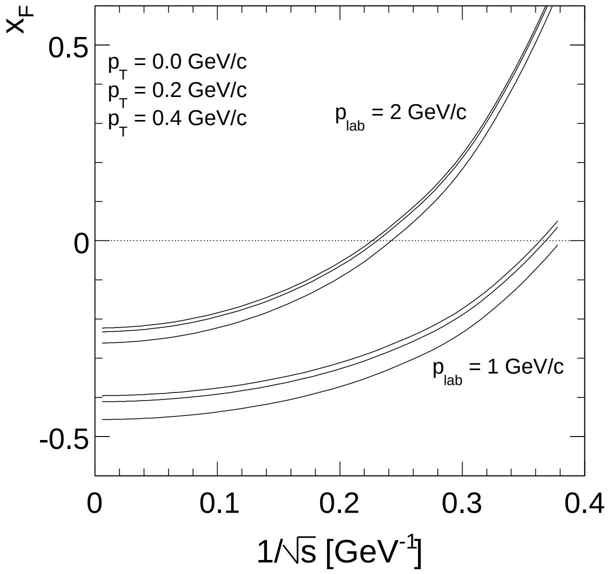

Figure 101: x_F as a function of 1/$\sqrt{s}$ for p_{lab} = 1 and 2 GeV/c, varying p_T from 0 to 0.4 GeV/c

This behaviour means that for given x_F (or rapidity) the nuclear contribution will increase with decreasing beam momentum. This effect is of course also to be expected for peripheral heavy ion collisions where the separation of prompt baryons from the delayed nuclear cascade will become more important but also more difficult with decreasing interaction energy.

13.5.2 *The target fragmentation*

As shown above prompt net baryons from target fragmentation are well described by the superposition of elementary proton-nucleon collisions. With increasing $\sqrt{s}$ this means that this contribution will move back in x_F due to increasing transparency until at the highest ISR and at RHIC energies the central region around x_F = 0 will be only populated by pair produced baryons. In the x_F region below $\sim$ -0.3 the yields will not change appreciably due to the approximate scaling behaviour. Towards lower $\sqrt{s}$ the feed-over of the target fragmentation into the projectile hemisphere will accordingly increase. Together with the increasing nuclear component a clear separation will therefore become more involved.

13.5.3 The projectile component

The evolution of the projectile component with collision energy is of considerable interest as it carries unique information about multiple hadronic collisions. Since its diffractive part is connected - for minimum bias p+A collisions - to the fraction of single projectile collisions which is as discussed above on a level of 60% for p+C interactions, there should be approximative energy scaling with a progressive widening of the peak towards lower energies as measured in p+p interactions. For the non-diffractive part the situation is however much less clear, in particular as there is no theoretical understanding of the observed baryon number transfer and as there is only very limited experimental information available on the required level of precision. It has been shown above that the net baryon density distribution shifts downward by 0.15 units of x_F in p+C collisions, the same shift being observed for the neutrons. It has also been shown that this baryon number transfer increases with centrality as indicated by the dependence on the number of grey protons. It has also in addition been indicated that resonance production and decay presents a very effective source of baryon transfer. If with increasing interaction energy the excitation of the projectile proton in its multiple collisions also increases and therefore the spectrum of produced resonances extends to higher masses, the reduction of central net baryon density via transparency should be reduced or even compensated. At lower $\sqrt{s}$ the situation should become, as for the two other contributions, more obscure due to the increased mutual overlap of the different components.

13.6 Proton and net proton multiplicities

Using the p_T integrated density distributions dn/dx_F extracted above for the inclusive p+C interaction as well as for the different sub-components, the corresponding baryonic multiplicities may now be determined by integration over x_F. This results in the following numbers:

$$\text{inclusive proton multiplicity} \qquad \langle n_\mathrm{p} \rangle = 1.881 \tag{29}$$

$$\text{inclusive anti-proton multiplicity} \qquad \langle n_{\bar{\mathrm{p}}} \rangle = 0.052 \tag{30}$$

$$\text{multiplicity of pair produced protons} \qquad \langle n_{\bar{\mathrm{p}}} \rangle = 0.0653 \tag{31}$$

$$\text{inclusive net proton multiplicity} \qquad \langle n_\mathrm{p}^\mathrm{net} \rangle = 1.816 \tag{32}$$

There are two predictions respectively for the net projectile component and for the expected net target component established from the elementary p+p collisions [3]:

$$\text{predicted net projectile component} \qquad \langle n_\mathrm{p}^\mathrm{proj,pred} \rangle = 0.550 \tag{33}$$

This assumes baryon number conservation and a negligible increase in neutron and hyperon production.

$$\text{predicted net target component} \qquad \langle n_\mathrm{p}^\mathrm{targ,pred} \rangle = 0.690 \tag{34}$$

This uses isospin invariance and the measured number of 1.6 projectile collisions.

Subtracting the predicted target component from the total net proton density in the projectile fragmentation region, the multiplicity of net projectile protons is measured as

$$\text{measured net projectile component} \qquad \langle n_\mathrm{p}^\mathrm{proj,meas} \rangle = 0.520 \tag{35}$$

which reproduces the expected multiplicity to within 5.5% and leaves room for some increase of the hyperon yields in p+C collisions.

Subtracting the predicted target component from the total net proton density in the backward region, the nuclear component is measured as

$$\text{measured nuclear component} \qquad \langle n^{\text{nucl,meas}} \rangle = 0.655 \tag{36}$$

A Gauss fit to the nuclear component in the symmetric regions of the target-subtracted proton density yields the multiplicity

$$\text{Gaussian nuclear component} \qquad \langle n^{\text{nucl,Gauss}} \rangle = 0.631 \tag{37}$$

which complies to within 3.6% with the straight-forward subtraction.

Finally there is the modified target component obtained by subtraction of the Gaussian nuclear component from the overall proton density which smooths the diffractive peak in accordance with the Fermi motion of the hit nucleons. This modified target component results in the multiplicity

$$\text{modified target component} \qquad \langle n^{\text{targ,mod}} \rangle = 0.670 \tag{38}$$

which reproduces the predicted multiplicity (34) to within 2.9%.

In conclusion it may be stated that the total measured net proton multiplicity of 1.82 per inelastic event is made up by the superposition of three components of comparable magnitude, namely a projectile multiplicity of 0.52, a target multiplicity of 0.67 and a nuclear component of 0.63 units. The multiplicities of anti-protons and pair produced protons are 0.052 and 0.0653, respectively, corresponding to 2.9% and 3.6% of the total net proton yield.

14 Proton production in p+C collisions: p_T dependence

Following the study of p_T integrated yields in the preceding section, the double-differential proton cross sections will now be studied for the three components of projectile fragmentation, target fragmentation, and nuclear cascading, thus adding the transverse dimension to the experimental scrutiny. In order to comply with the discussion of the integrated proton yields dn/dx_F, Sect. 13, the double differential cross sections will be used in their non-invariant form

$$\frac{1}{p_T}\frac{d^2n}{dx_F dp_T} = \frac{2\pi}{\sigma_{\text{inel}}}\frac{\sqrt{s}}{2}\frac{f(x_F,p_T)}{E} \tag{39}$$

see also (10). In a first step, the net proton cross sections will be defined using the results on anti-protons, Sect. 12. A detailed comparison of the overall backward cross sections with the predicted contribution from target fragmentation will reveal a necessary p_T dependent modification of this component which will then be employed to extract in turn the projectile and nuclear components in their p_T dependence.

14.1 Pair produced protons and net proton density

Using the results of the discussion of the double differential anti-proton yields and their separation into target and projectile components in Sect. 12.2, the yield of pair produced protons may be estimated by multiplying the projectile component by the isospin factor 1.6, maintaining the p_T enhancement as parametrized in (25). The target component stays equal to the anti-proton yield due to isospin symmetry. The total and the resulting net proton densities are shown in Fig. 102 as a function of x_F for different values of p_T.

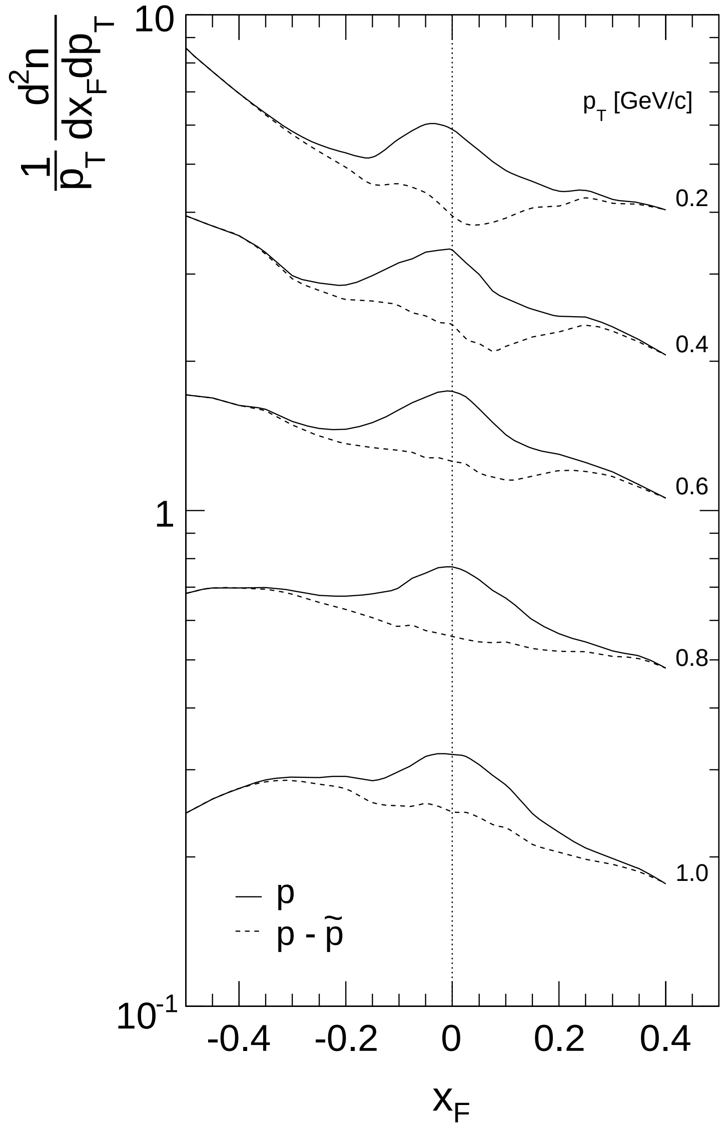

Figure 102: Total and net proton density $\frac{1}{p_T}\frac{d^2n}{dx_F dp_T}$ as a function of x_F for different p_T values indicated in the panel. The distribution at p_T = 0.2 GeV/c is multiplied by factor of 1.2 for better separation

14.2 Target component

As discussed in Sect. 13.2.2 the target component of net proton production in p+C interactions may be predicted from p+p collisions using the number of projectile collisions $\langle \nu \rangle$ = 1.6, the target overlap function $R_{\mathrm{p}}^{c,\mathrm{net}}$ (22) and Fig. 71, and the measured proton and neutron cross sections [3]. The only additional assumption to be made for the double differential yield is the equality of the p_T distributions for neutrons and protons, see [3] for experimental evidence. The result for the target component and its subtraction from the overall proton yield is shown in Fig. 103.

Compared to the same prediction and subtraction for the p_T integrated densities, Figs. 94 and 95, a p_T dependence becomes visible. It is the region of x_F between -0.2 and -0.3 which is extremely sensitive to the predicted target yield. At transverse momenta below the mean p_T (Fig. 55) the prediction overshoots the total density by about 20%, whereas for higher p_T it falls

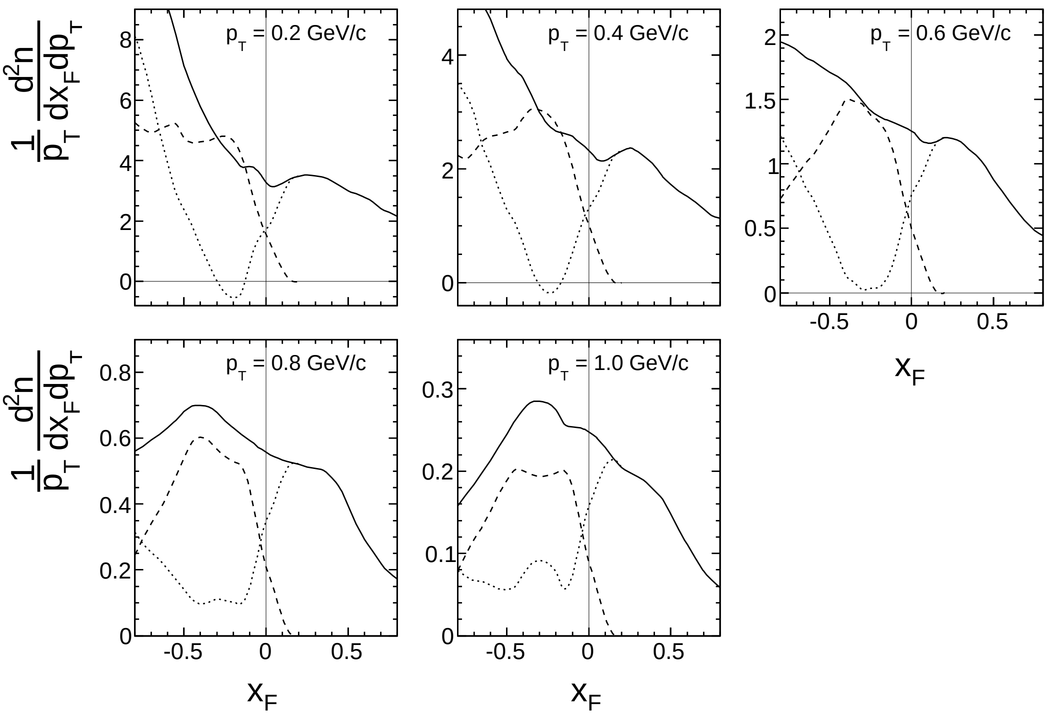

Figure 103: Double differential net proton yield $\frac{1}{p_T}\frac{d^2n}{dx_F dp_T}$ as a function of x_F for five different values of p_T. Full line: total yield, broken line: predicted target component, and dotted line: after subtraction of the target component

low by up to 40% at p_T = 1 GeV/c. In this x_F region neither the possible projectile feed-over nor the nuclear component may explain, by their limited x_F range, the observed p_T dependence. Instead a yield suppression at low p_T followed by an enhancement at high p_T similar to the one found for anti-protons, Sect. 12.2, has to be invoked also for the target contribution. In order to preserve a physical x_F dependence of the projectile and nuclear components, see Sects. 14.3 and 14.4 below, an x_F dependent pattern of the target enhancement as shown in Fig. 104 imposes itself.

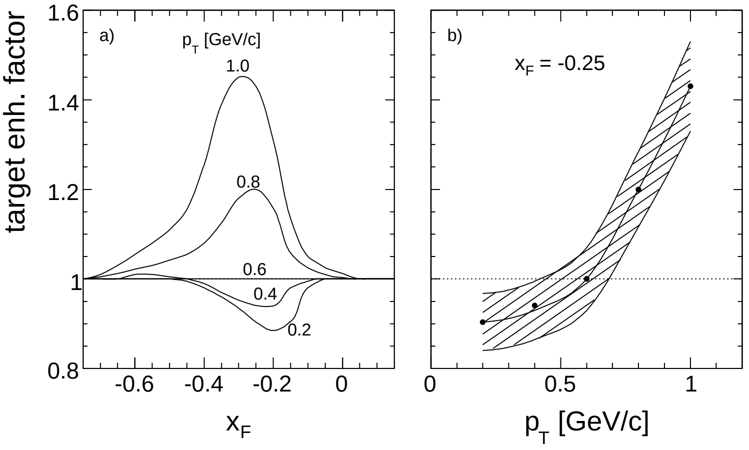

Figure 104: Enhancement factor of the target component a) as a function of x_F for p_T values between 0.2 and 1 GeV/c and b) as a function of p_T for x_F = -0.25. The shaded region represents the error margins

This phenomenon is also borne out by a comparison of the mean p_T values between p+C and p+p interactions shown in Fig. 105.

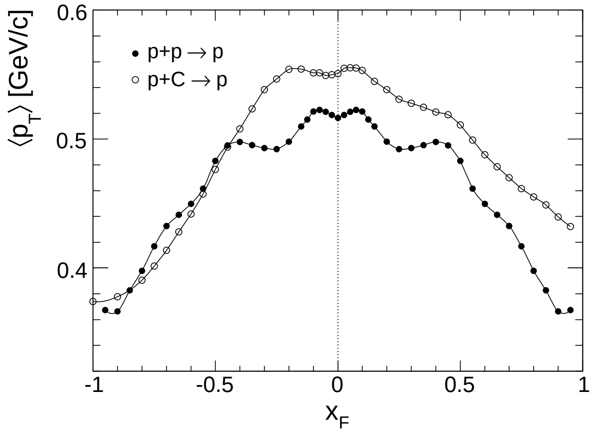

Figure 105: Comparison of the mean p_T values of protons in p+C (open circles) and p+p interactions (closed circles) as a function of x_F from x_F = -1.0 to x_F = +0.95

If the target component would show a p_T dependence equivalent to p+p interactions, the mean p_T values should approach the ones for p+p at x_F around -0.2 to -0.3 where target fragmentation prevails.

Applying this enhancement, the target component and its subtraction from the total measured yield take the pattern shown in Fig. 106.

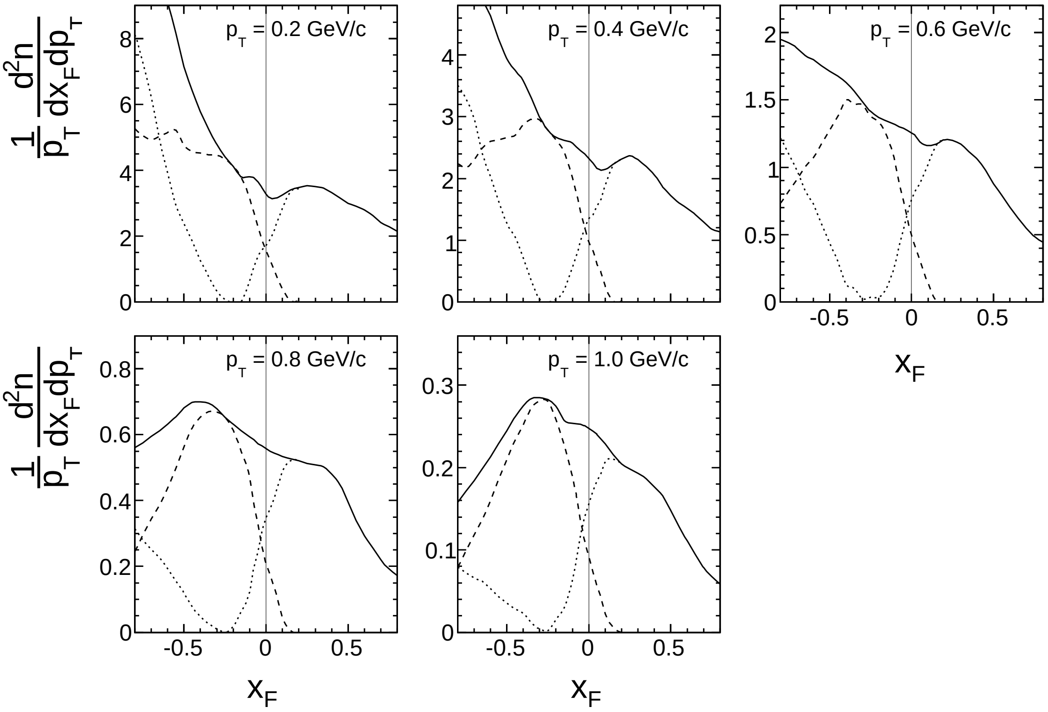

Figure 106: Double differential net proton yield $\frac{1}{p_T}\frac{d^2n}{dx_F dp_T}$ as a function of x_F for five values of p_T. Full line: total yield, broken line: predicted enhanced target component, dotted line: after subtraction of the enhanced target component

This subtraction leaves clearly defined and separated projectile and nuclear components which will be discussed in the subsequent sections

14.3 The projectile component

The hadronization of the projectile is already clearly visible in the dotted line of Fig. 106. It saturates the total yield at $x_F > 0.2$ and comes down to zero at $x_F \sim$ -0.2 due to the limited range of the baryonic overlap function. In order to put this behaviour in perspective as far as the x_F distributions for different transverse momenta are concerned, the projectile components normalized to their maximum densities are presented in Fig. 107.

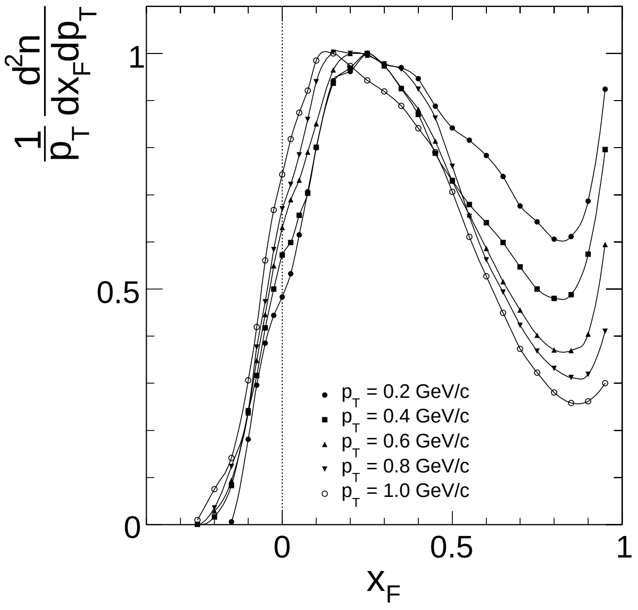

Figure 107: Net proton density $\frac{1}{p_T}\frac{d^2n}{dx_F dp_T}$ from projectile fragmentation as a function of x_F normalized to its maximum value for five p_T values between 0.2 and 1 GeV/c

Compared to the p_T integrated distribution, Fig. 95, there is a clear dependence of baryon number transfer on p_T. The maximum density shifts from x_F = 0.3 at low p_T to x_F = 0.1 at 1 GeV/c. The density at $x_F \gtrsim 0.6$ corresponding to low mass excitation is strongly reduced with increasing p_T whereas the transfer function is successively extending further into the backward hemisphere.

Further information concerning the p_T dependence comes from a direct comparison to p+p interactions. Extracting the projectile component from the symmetric p+p collision using the baryonic overlap function determined in Sect. 11.1 the ratio

$$R^{\mathrm{proj}} = \left(\frac{1}{p_T}\frac{d^2n}{dx_F dp_T}\right)^{\mathrm{pC}} \Bigg/ \left(\frac{1}{p_T}\frac{d^2n}{dx_F dp_T}\right)^{\mathrm{pp}} \tag{40}$$

may be obtained as shown in Fig. 108 as a function of p_T for different values of x_F.

A clear increase with p_T of the net proton yields is visible for all values of x_F. The overall increase of the cross sections with decreasing x_F is due to the general baryon number transfer in p+C interactions visible in the p_T integrated distributions of Fig. 57 ("minimum bias" compared to p+p). This can be normalized out by multiplying R^{proj} by the integrated density ratio between p+p and p+C collisions:

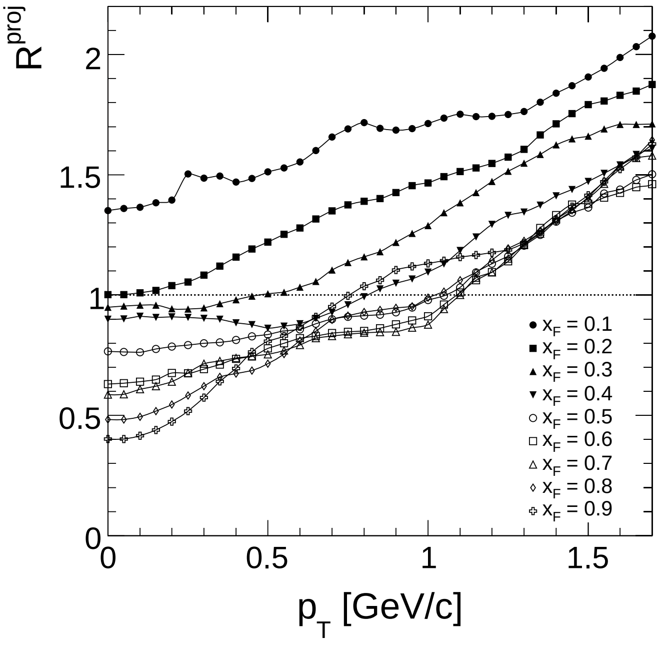

Figure 108: Density ratio R^{proj} of the projectile components of p+C and p+p interactions as a function of p_T for different values of x_F

$$R^{\text{proj}}_{\text{norm}} = R^{\text{proj}} \left(\frac{dn}{dx_F}\right)^{\text{pp}} \bigg/ \left(\frac{dn}{dx_F}\right)^{\text{pC}} \tag{41}$$

The resulting ratio $R^{\text{proj}}_{\text{norm}}$ is shown in Fig. 109 again as a function of p_T for different values of x_F.

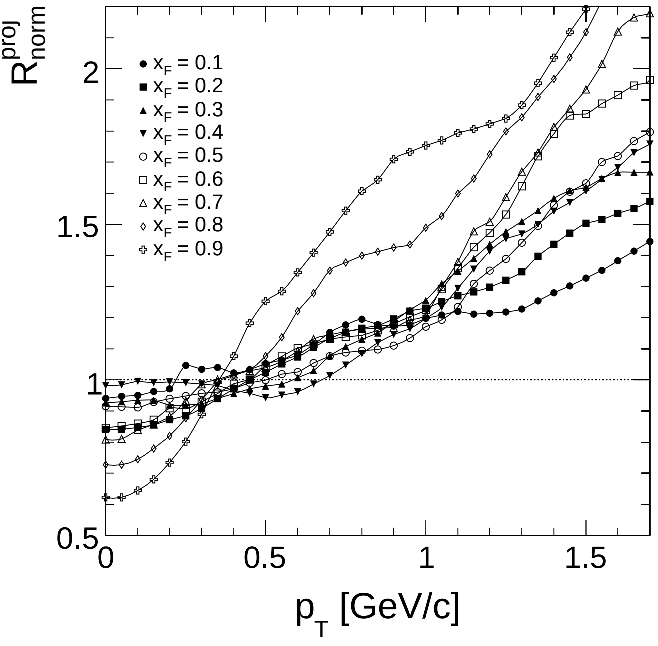

Figure 109: Normalized density ratio $R^{\text{proj}}_{\text{norm}}$ as a function of p_T for different values of x_F

The wide spread observed in Fig. 108 reduces to a narrow band of p_T enhancements which are about independent on x_F except for the x_F range approaching diffraction. Again, as for p̄ in Sect. 12.2 and for the target component in the preceding section, the normalized densities are reduced by 10-20% at low p_T and enhanced to factors of about 1.5 at p_T = 1.5 GeV/c.

14.4 The nuclear component

The onset of the contribution from nuclear cascading is already visible in Fig. 106 by the dotted lines at $x_F < -0.25$. This range is extended to the far backward hemisphere down to x_F = -1.6 in Fig. 110. In this Figure the total proton density, the predicted target contribution and the target subtracted yield are shown as a function of x_F for five values of p_T between 0.2 and 1 GeV/c.

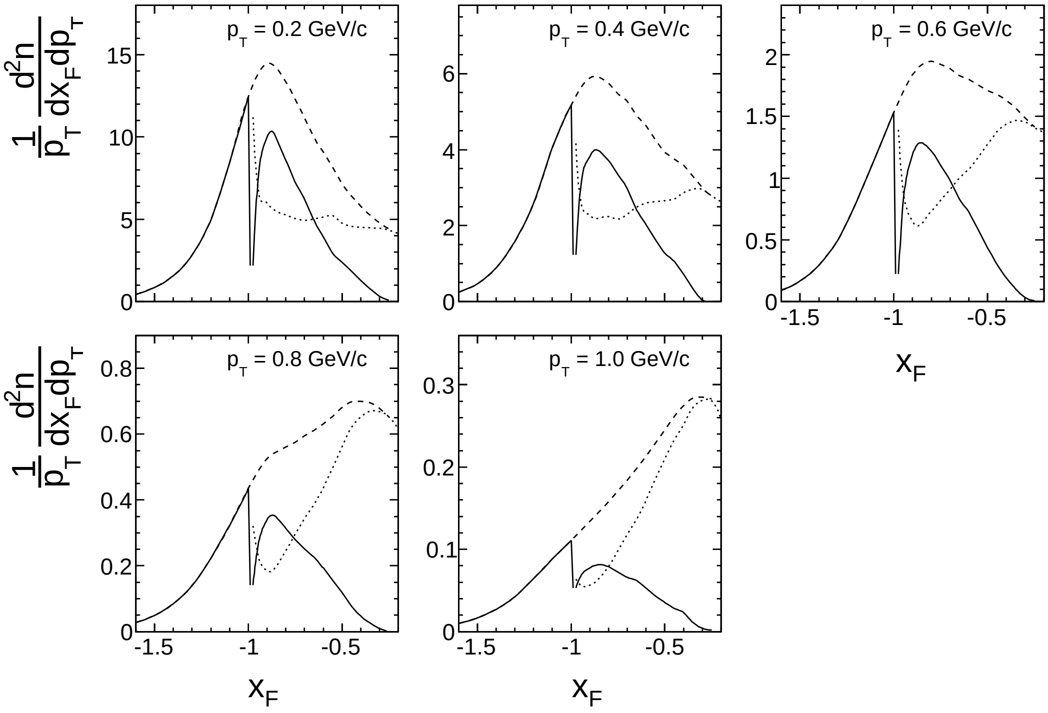

Figure 110: Double differential net proton yield as a function of x_F for five values of p_T. Broken line: total proton yield, dotted line: predicted target contribution, full line: target subtracted proton density

As already discussed for the p_T integrated densities in Sect. 13.4 (Figs. 97 and 98), the presence of the diffractive peak from proton fragmentation in the predicted target contribution creates a sharp spike between $x_F \sim$ -0.9 and x_F = -1.0 which should be visible in the total proton density distribution in this area. The absence of such structure in the measured yield indicates, as argued in Sect. 13.4, a smoothing of the predicted structure via quasi-elastic re-scattering of the diffrative protons inside the Carbon nucleus. This re-scattering extends typically up to ±0.2 units of x_F around x_F = -1 [45]. Beyond this range the target subtracted yield shows a Gaussian behaviour as presented in Fig. 111.

The fit parameters show, within tight errors, a stable mean value in x_F between -0.92 and -0.93 in agreement with the p_T integrated fit (28). The rms deviation increases with p_T from 0.22 to 0.3 units of x_F. The p_T dependences of the maximum density and of the yield integrated over x_F are shown in Fig. 112.

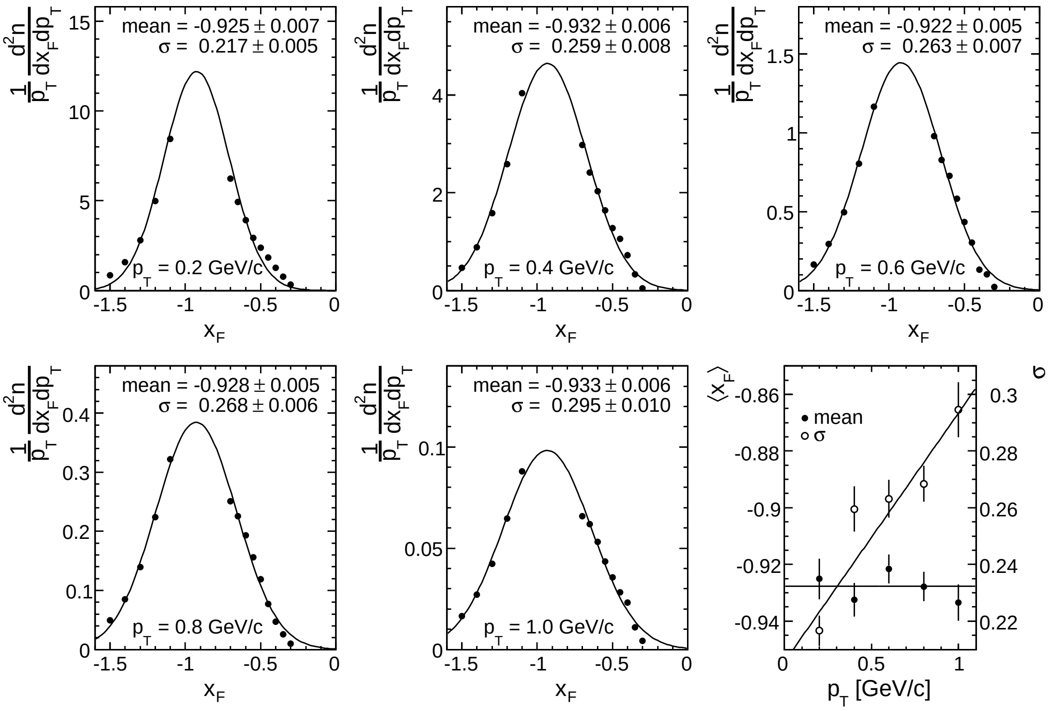

Figure 111: Double differential, target subtracted proton yields as a function of x_F for -1.6 $<$ x_F $<$ -0.3 with the exclusion of the range -1.1 $<$ x_F $<$ -0.8 for five values of p_T between 0.2 and 1.0 GeV/c. Superimposed as full lines are Gaussian fits with mean values $\langle x_F \rangle$ and σ indicated in each panel. The last panel shows plots of $\langle x_F \rangle$ (left scale) and σ (right scale) as a function of p_T

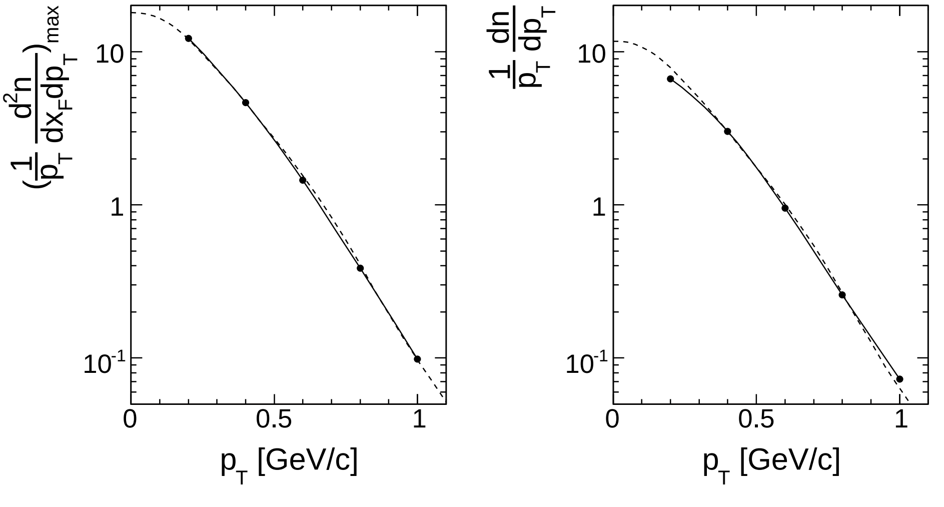

Figure 112: a) Maximum proton density and b) yield $\frac{1}{p_T}\frac{dn}{dp_T}$ integrated over x_F of the nuclear component as a function of p_T. The full lines represent data interpolations, the broken lines correspond to the p_T dependence of the proton density in p+p interactions at $|x_F|$ = 0.95 [3], normalized at p_T = 0.4 GeV/c

It is interesting to observe that the p_T dependence of the nuclear component is not Gaussian and corresponds to the one measured in the diffractive region of p+p interactions [3].

Using the Gaussian fits as an estimator of the nuclear component a modified target component may be obtained by subtracting these fitted densities from the total proton yield as shown in Fig. 113.

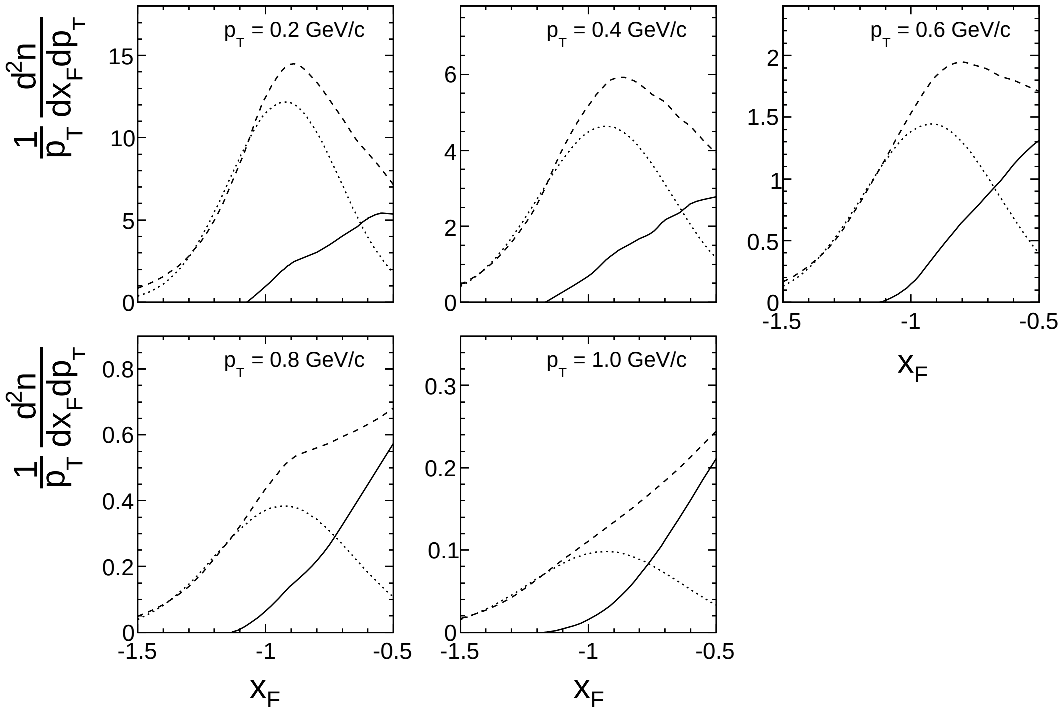

Figure 113: Double differential proton yields as a function of x_F for five values of p_T. Broken lines: total proton yield, dotted lines: Gaussian fit to the nuclear component, full lines: modified target component obtained by the subtraction of the Gaussian fits from the total proton density

The resulting modified target component extends now to x_F values below -1.0 and shows a smooth behaviour through the region of proton diffraction in accordance with the p_T integrated yield, Sect. 13.4.

15 Conclusion

As part of a comprehensive study of hadronic production in elementary and nuclear collisions at the SPS, new data from the NA49 experiment on proton, anti-proton, neutron and light ion production in minimum bias p+C interactions are presented. Making full use of the acceptance coverage and the particle identification capabilities of the NA49 detector, a wide phase space area from the far forward direction at Feynman x_F of 0.95 to the far backward direction down to x_F = -0.8 has been exploited. Using available data from a Fermilab experiment the data coverage could be further extended into the nuclear fragmentation region down to $x_F \sim$ -2.0. In addition, deuteron and triton production have been studied in the lab momentum range from 0.25 to 3 GeV/c making available there for the first time cross sections in the low to medium p_T region. In addition a limited amount of data with grey proton detection allows for a first look at the centrality dependence of baryon number transfer.

Given the complete phase space coverage of the combined data set, the main aim of this publication is the separation and isolation of the three components of hadronization in p+C collisions, namely projectile fragmentation, target fragmentation and nuclear cascading. This study has been conducted both for p_T integrated quantities and using double differential cross sections to obtain a complete view of the p_T dependence. For this aim, the baryonic overlap functions from the projectile to the target regions and vice versa have been determined experimentally using both the elementary p+p and the asymmetric p+C interactions. This has been achieved in a completely model-independent way relying essentially on baryon number conservation and isospin symmetry. For anti-proton production the absence of a nuclear contribution has been shown and the superposition of the target and the projectile fragmentation has been established using the known number of projectile collisions inside the Carbon nucleus. This allows for the definition of the yield of pair produced protons and thereby of net proton densities.

In contrast to the a priory unknown projectile and nuclear components, the target fragmentation occupies a special place as it should at least to first order be describable by a superposition of single nucleon fragmentations taking of course into account the number of projectile collisions and isospin effects. This approach works out well for p_T integrated proton densities with the exception of the diffractive contribution contained in the elementary interactions. This contribution is evidently smeared out by secondary, quasi-elastic interactions of the corresponding low momentum protons in the nuclear rest system. The subtraction of the thus predicted target component yields both the projectile and the nuclear components. The former is proven to preserve baryon number combined with a sizeable amount of baryon transfer of order 0.15 units of x_F. The latter turns out to have a Gaussian shape in x_F centred at x_F = -0.92 with a substantial FWHM of 0.6 units far in excess of the narrow x_F distribution centred close to -1.0 which might be expected from Fermi motion alone. In the case of the p+C collisions studied here, the three components have comparable total yields of 0.52, 0.67 and 0.65 net protons respectively for the projectile, target and nuclear contributions. This sums up to 1.84 net protons in total which complies with the direct yield integration to within 1%.

The study of double differential cross sections gives access to the additional dimension of transverse momentum. All three components show a distinct transverse activity which goes beyond the naive expectation from elementary collisions or nuclear binding. The projectile component features, both for protons and anti-protons, a suppression by 10-20% at low p_T followed by an enhancement of about 50% at p_T = 1.5 GeV/c. This pattern is rather x_F independent in the forward hemisphere. The target component shows a similar behaviour, however with a distinct x_F dependence centred at $x_F \sim$ -0.3. The nuclear component finally has a wide, non-Gaussian p_T dependence which goes far beyond the one expected from Fermi motion and which is shown to be comparable to the one measured in the diffractive region of p+p interactions.

As for the previous publications [1–4] the measured cross sections and two-dimensional interpolation values are available on the Web Site [46].

Acknowledgements

This work was supported by the Polish State Committee for Scientific Research (P03B00630), the Polish Ministry of Science and Higher Education (N N202 078735), the Bulgarian National Science Fund (Ph-09/05), the EU FP6 HRM Marie Curie Intra-European Fellowship Program, the Hungarian Scientific Research Fund OTKA (T68506) and the Hungarian OTKA/NKTH A08-77719 and A08-77815 grants.

References

[1] C. Alt et al., Eur. Phys. J. **C45** (2006) 343
[2] T. Anticic et al., Eur. Phys. J. **C68** (2010) 1
[3] T. Anticic et al., Eur. Phys. J. **C65** (2010) 9
[4] C. Alt et al., Eur. Phys. J. **C49** (2007) 897
[5] G. Barr et al., Eur. Phys. J. **C49** (2007) 919
[6] O. Chvala et al., A survey of backward proton and pion production in p+C interactions at beam momenta from 1 to 400 GeV/c
[7] Y. D. Bayukov et al., Phys. Rev. **C20**, (1979) 764
[8] S. Frankel et al., Phys. Rev. **C20**, (1979) 2257
[9] D. Barton et al., Phys. Rev. **D27** (1983) 2580
[10] S. Afanasiev et al., Nucl. Instrum. Meth. **A430** (1999) 210
[11] A. E. Brenner et al., Phys. Rev. **D26** (1982) 1497
[12] H. G. Fischer et al., Heavy Ion Physics **17** (2003) 369
[13] N. A. Burgov et al., Sov. J. Nucl. Phys. **30** (1979) 371, Yad. Fiz. **30** (1979) 720
[14] K. Braune et al., Z. Phys. **C13** (1982) 191
[15] J. L. Bailly et al., Z. Phys. **C35** (1987) 301
[16] N. A. Nikiforov et al., Phys. Rev. **C22** (1980) 700
[17] NA49 collaboration, Inclusive charged kaon production in p+C interactions, to be published
[18] R. Bailey et al., Z. Phys. **C29** (1985) 1
[19] T. S. Nigmanov et al., Phys. Rev. **D83** (2011) 012002
[20] A. S. Carroll et al., Phys. Lett. **B80** (1979) 319
[21] V. Blobel et al., Nucl. Phys. **B69** (1974) 454
V. Blobel et al., Nucl. Phys. **B135** (1978) 379
[22] E. E. Zabrodin et al., Phys. Rev. **D52** (1995) 1316
[23] M. Yu. Bogolyubsky et al., Sov. J. Nucl. Phys. **50** (1989) 424, Yad. Fiz. **50** (1989) 683
[24] V. V. Ammosov et al., N. Cim. **A40** (1977) 237
V. V. Ammosov et al., Nucl. Phys. **B115** (1976) 269
[25] V. V. Abramov et al., Nucl. Phys. **B173** (1980) 348
[26] M. Bourquin and J.-M. Gaillard, Nucl. Phys. **B114** (1976) 334
[27] A. Breakstone et al., Z. Phys. **C21** (1984) 321
[28] M. Aguilar-Benitez et al., Z. Phys. **C50** (1991) 405
[29] U. Idschok et al., Nucl. Phys. **B140** (1978) 365
[30] D. Denegri et al., Nucl. Phys. **B114** (1976) 413
[31] L. Baksay et al., Phys. Lett. **53B** (1975) 484
[32] C. Conta et al., Nucl. Phys. **B175** (1980) 97
[33] C. Amsler et al., Phys. Lett. **B667** (2008) 1
[34] A. Suzuki et al., Nucl. Phys. **B172** (1980) 327
[35] D. Drijard et al., Z. Phys. **C9** (1981) 293
[36] J. W. Lamsa et al., Phys. Rev. **D26** (1982) 1769
[37] M. Rozanska et al., Nucl. Phys. **B162** (1980) 505
[38] http://quark.phy.bnl.gov/~ynara/jam/
[39] T. Anticic et al., Phys. Rev. **C83** (2011) 014901
[40] A. M. Rossi et al., Nucl. Phys. **B84** (1975) 269
[41] G. I. Veres et al., Nucl. Phys. **A661** (1999) 383c
[42] A. Bolshakova et al., Eur. Phys. J. **C70** (2010) 573

[43] Y. D. Bayukov et al., Sov. J. Nucl. Phys. **18** (1974) 639
Y. D. Bayukov et al., Sov. J. Nucl. Phys. **19** (1974) 648
[44] S. Frankel et al., Phys. Rev. Lett. **36** (1976) 642
[45] W. Bell et al., Nucl. Phys. **B254** (1985) 475
[46] http://cern.ch/spshadrons